Universidad de Alcalá
COMISIÓN DE ESTUDIOS OFICIALES
DE POSGRADO Y DOCTORADO

ACTA DE EVALUACIÓN DE LA TESIS DOCTORAL

(FOR EVALUATION OF THE ACT DOCTORAL THESIS)

Año académico (*academic year):* 2016/17

DOCTORANDO *(candidate PHD)*: **DOMÍNGUEZ LÓPEZ, ALEJANDRO**
D.N.I./PASAPORTE (*Id.Passport*): ******5936D**
PROGRAMA DE DOCTORADO *(Academic Committee of the Programme)*: **D441 ELECTRÓNICA: SISTEMAS ELECTRÓNICOS AVANZADOS. SISTEMAS INTELIGENTES**
DPTO. COORDINADOR DEL PROGRAMA *(Department)*: **ELECTRÓNICA**
TITULACIÓN DE DOCTOR EN *(Phd title)*: **DOCTOR/A POR LA UNIVERSIDAD DE ALCALÁ**

En el día de hoy 04/07/17, reunido el tribunal de evaluación, constituido por los miembros que suscriben el presente Acta, el aspirante defendió su Tesis Doctoral **con Mención Internacional** (*In today assessment met the court, consisting of the members who signed this Act, the candidate defended his doctoral thesis with mention as International Doctorate*), elaborada bajo la dirección de (*prepared under the direction of*) MIGUEL GONZÁLEZ HERRÁEZ // SONIA MARTÍN LÓPEZ.

Sobre el siguiente tema *(Title of the doctoral thesis)*: *OPTIMIZED LONG-RANGE AND HIGH-RESOLUTION BRILLOUIN OPTICAL TIME DOMAIN ANALYZERS*

Finalizada la defensa y discusión de la tesis, el tribunal acordó otorgar la CALIFICACIÓN GLOBAL[1] de (**no apto, aprobado, notable** y **sobresaliente**) *(After the defense and defense of the thesis, the court agreed to grant the GLOBAL RATING (fail, pass, good and excellent)*: SOBRESALIENTE

Alcalá de Henares, a 4 de JULIO de 2017

Fdo. *(Signed)*: SALVADOR SALOT Fdo. *(Signed)*: FERNANDO NARANJO Fdo. *(Signed)*: Marcelo Soto

FIRMA DEL ALUMNO (candidate's signature),

Fdo. *(Signed)*: ALEJANDRO DOMÍNGUEZ LÓPEZ

Con fecha 24 de julio de 2017 la Comisión Delegada de la Comisión de Estudios Oficiales de Posgrado, a la vista de los votos emitidos de manera anónima por el tribunal que ha juzgado la tesis, resuelve:

☒ Conceder la Mención de "Cum Laude"
☐ No conceder la Mención de "Cum Laude"

La Secretaria de la Comisión Delegada

[1] La calificación podrá ser **"no apto" "aprobado" "notable"** y **"sobresaliente"**. El tribunal podrá otorgar la mención de "cum laude" si la calificación global es de sobresaliente y se emite en tal sentido el voto secreto positivo por unanimidad. (*The grade may be* ***"fail" "pass" "good"*** *or* ***"excellent"****. The panel may confer the distinction of "cum laude" if the overall grade is "Excellent" and has been awarded unanimously as such after secret voting.).*

Universidad de Alcalá
COMISIÓN DE ESTUDIOS OFICIALES
DE POSGRADO Y DOCTORADO

En aplicación del art. 14.7 del RD. 99/2011 y el art. 14 del Reglamento de Elaboración, Autorización y Defensa de la Tesis Doctoral, la Comisión Delegada de la Comisión de Estudios Oficiales de Posgrado y Doctorado, en sesión pública de fecha 24 de julio, procedió al escrutinio de los votos emitidos por los miembros del tribunal de la tesis defendida por *DOMÍNGUEZ LÓPEZ, ALEJANDRO*, el día 4 de julio de 2017, titulada *OPTIMIZED LONG-RANGE AND HIGH-RESOLUTION BRILLOUIN OPTICAL TIME DOMAIN ANALYZERS*, para determinar, si a la misma, se le concede la mención "cum laude", arrojando como resultado el voto favorable de todos los miembros del tribunal.

Por lo tanto, la Comisión de Estudios Oficiales de Posgrado **resuelve otorgar** a dicha tesis la

MENCIÓN "CUM LAUDE"

Alcalá de Henares, 27 julio de 2017
EL PRESIDENTE DE LA COMISIÓN DE ESTUDIOS
OFICIALES DE POSGRADO Y DOCTORADO

Firmado digitalmente por VELASCO PEREZ JUAN RAMON - DNI 03087239H
Fecha: 2017.07.28 11:14:22 -06'00'

Juan Ramón Velasco Pérez

Copia por e-mail a:
Doctorando: DOMÍNGUEZ LÓPEZ, ALEJANDRO
Secretario del Tribunal: FERNANDO B. NARANJO VEGA.
Directores de Tesis: SONIA MARTÍN LOPEZ // MIGUEL GONZÁLEZ HERRÁEZ

Universidad de Alcalá

ESCUELA DE DOCTORADO
Servicio de Estudios Oficiales de Posgrado

DILIGENCIA DE DEPÓSITO DE TESIS.

Comprobado que el expediente académico de D./Dª ALEJANDRO DOMÍNGUEZ LÓPEZ reúne los requisitos exigidos para la presentación de la Tesis, de acuerdo a la normativa vigente, y habiendo presentado la misma en formato: ☒ soporte electrónico ☐ impreso en papel, para el depósito de la misma, en el Servicio de Estudios Oficiales de Posgrado, con el nº de páginas: 160 se procede, con fecha de hoy a registrar el depósito de la tesis.

Alcalá de Henares a 5 de junio de 2017

UNIVERSIDAD DE ALCALÁ SERVICIO DE ESTUDIOS OFICIALES DE POSGRADO

Emilia Rivero Antúnez

Fdo. El Funcionario

Universidad de Alcalá

Escuela Politécnica Superior

Departamento de Electrónica

“Optimized Long-Range and High-Resolution Brillouin Optical Time Domain Analyzers”

Autor:

Alejandro Domínguez López

Directores:

Dra. Sonia Martín López

Dr. Miguel González Herráez

2017

TESIS DOCTORAL

DEPARTAMENTO DE ELECTRÓNICA

Edificio Politécnico

Campus Universitario s/n

28805 Alcalá de Henares (Madrid)

Teléfono: 91 885 65 40

Fax: 91 885 65 91

eldep@depeca.uah.es

rector@uah.es

Universidad de Alcalá

Dra. Sonia Martín López

Dr. Miguel González Herráez

INFORMAN: Que la Tesis Doctoral titulada **"Optimized long-range and high-resolution Brillouin Optical Time Domain Analyzers"** presentada por D. Alejandro Domínguez López, y realizada bajo la dirección de los doctores Dª. Sonia Martín López y D. Miguel González Herráez, dentro del campo de los Sensores de Fibra Óptica, reúne los méritos de calidad y originalidad para optar al Grado de Doctor.

Alcalá de Henares, 19 de mayo de 2017

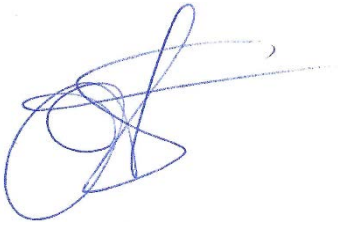

Fdo. Dra. Sonia Martín López

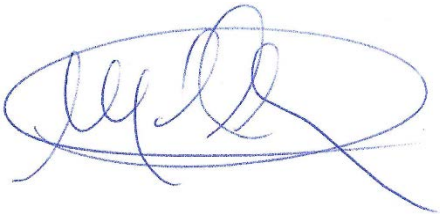

Fdo. Dr. Miguel González Herráez

DEPARTAMENTO DE ELECTRÓNICA

Edificio Politécnico

Campus Universitario s/n

28805 Alcalá de Henares (Madrid)

Teléfono: 91 885 65 40

Fax: 91 885 65 91

eldep@depeca.uah.es

rector@uah.es

Dr. D. Manuel Mazo Quintas, coordinador del Programa de Doctorado "ELECTRÓNICA: Sistemas Electrónicos Avanzados. Sistemas Inteligentes".

INFORMA: Que la Tesis Doctoral titulada **"Optimized long-range and high-resolution Brillouin Optical Time Domain Analyzers"** presentada por D. Alejandro Domínguez López, y dirigida por los doctores Dª. Sonia Martín López y D. Miguel González Herráez, cumple con todos los requisitos científicos y metodológicos para ser defendida ante un Tribunal para optar al Grado de Doctor, según lo indicado por la Comisión Académica del Programa de Doctorado.

Alcalá de Henares, 31 de mayo de 2017

Fdo. D. Manuel Mazo Quintas

Walk a single path, becoming neither arrogant with victory nor broken with defeat, without forgetting caution when all is quiet or becoming frightened when danger threatens.

- Jigoro Kano -

Agradecimientos

En primer lugar, quisiera agradecer de todo corazón, a mis directores de tesis, la Dra. Sonia Martín López y el Dr. Miguel González Herráez, el haber confiado en mí para llevar a cabo este bonito proyecto. A ellos les debo el trabajo de esta tesis, el haber descubierto y aprendido tanto sobre sensores de fibra óptica y haber conseguido transmitir mis ideas de la mejor manera posible. He de decir que os admiro mucho, sois un auténtico equipo y estoy muy orgulloso de haber compartido este tiempo con vosotros.

A la Dra. Ana Carrasco, por haberme convencido para dar el salto y embarcarme en esta aventura. Tenías razón, no me equivoqué.

Es necesario un reconocimiento al proyecto U-FINE (ERC Starting Grant 307441), que me ha permitido disfrutar de la financiación necesaria para poder desarrollar esta tesis satisfactoriamente en la Universidad de Alcalá (UAH).

Quiero agradecer profundamente el apoyo y el compañerismo recibido de todos los miembros del Grupo de Ingeniería Fotónica (GRIFO) de la UAH. A los doctores Fernando Naranjo y Óscar Esteban, así como a mis compañeros, principalmente a Alexia, con la que he trabajado codo con codo en numerosos experimentos, pero también a Andrés, Arantxa, Hugo, Juan, Javier, Luis, Marco, Paco, Piedad, Regina, Rodrigo, Rosario y Sirona. A Javier Tejedor, por todos esos buenos momentos, en los que incluyo las polémicas culinarias y disquisiciones varias. Quiero acordarme particularmente de Massimo Filograno, por haberme recibido tan abiertamente cuando llegué, por haber resuelto todas las dudas que le planteé y por ofrecerme su amistad y consejo desinteresadamente en cualquier momento. Y quiero agradecer especialmente a Xabi, que ha sido un gran compañero de trabajo, un auténtico referente del que he aprendido mucho y un verdadero amigo.

No puedo dejar de acordarme de otros de mis compañeros de fatigas en Alcalá: Ana, Jorge, Inés, Marco, Miguel y Susel, con los cuales he compartido innumerables buenos momentos.

Quiero agradecer especialmente a Laura el haberme acogido amable y desinteresadamente en su casa, regalándome su amistad sincera y contagiándome de su alegría y buena disposición para afrontar cualquier situación que la vida te plantee. Este agradecimiento se extiende, por supuesto, a Tomás, con el que también he compartido momentos inolvidables.

Quisiera acordarme particularmente de los miembros de INESC-Porto, Joao Ferreira, Prof. José Luis Santos, Prof. José Manuel Baptista y también, como no, Duarte Viveiros, por habernos acogido tan cariñosa y cálidamente durante nuestras dos visitas a Oporto.

No puedo olvidarme de los miembros del Grupo de Fibras Ópticas (GFO) del EPFL, en Lausana (Suiza), por el caluroso recibimiento que obtuve en mis dos estancias en su institución: Andrey, Desmond, Flavian, Kenny, Mehdi, Xin y Zhisheng. Particularmente he de agradecer al Prof. Luc Thévenaz por aceptarme e integrarme como uno más en su grupo y por sus numerosos y siempre valiosos consejos y apuntes científicos. A Svetlana por su paciencia y ayuda durante mi estancia. Y por supuesto, al Dr. Marcelo Soto, no sólo por hacerme disfrutar de brillantes conversaciones científicas con una pizarra y un rotulador, sino por haber compartido otros muchos momentos de gran valor fuera del laboratorio.

A todos los investigadores del CSIC con los que he tenido la suerte de coincidir y compartir momentos, no sólo de índole académica: los doctores Pedro Corredera, Juan Diego Ania Castañón, Concepción Pulido y Aitor Villafranca.

No me puedo olvidar del grupo de los “navarros”, dirigido por los profesores Manuel López Amo y Alayn Loayssa, con los que he compartido grandísimos momentos tanto en congresos nacionales e internacionales, como en diversas escuelas de verano: Aitor, Daniel, Haritz, Javier, Jon, Juanjo, Mikel, Rosana y Sergio.

Extiendo este agradecimiento a todas las personas con las que he disfrutado y crecido en los años de desarrollo de esta tesis, así como a todos los expertos que han contribuido en el desarrollo de este trabajo. En particular, quisiera agradecer a los expertos evaluadores de esta tesis y a los miembros del tribunal.

Por supuesto, a mi familia, ya que sin su apoyo incondicional y constante, y a pesar de la distancia, no estaría aquí. A mis padres, por haberos “deslomado” y seguir haciéndolo por

darnos la mejor vida posible, aunque eso implique que estemos lejos. Por haberme transmitido vuestra pasión por lo que hacéis, vuestro amor y vuestro sacrificio. A mi hermana y mi hermano, porque me habéis dado vuestro apoyo y cariño aun estando a demasiados kilómetros de distancia. Por supuesto, a mis tíos, mi abuela, mis primos, y como no, a mis amigos. Sois mi sustento, y tengo mucha suerte de teneros.

Por último, a Itsaso, mi compañera de aventuras, y también a su familia. Te has convertido en un gran apoyo para mí, fundamental en este último periodo de escritura y, por supuesto, esta tesis es también, en parte, tuya. ¡Gracias!

Abstract

In order to properly satisfy the societal needs of today in terms of energy, communications, transport or housing, a great number of civil infrastructures is required. Dykes, bridges, highways or railroads should all guarantee a correct and continuous working, and hence, solutions to preserve and control the integrity of these installations are strongly needed. Distributed optical fiber sensors are particularly suitable for these kind of applications, for they can provide measurements of strain, temperature and/or vibrations (or any other magnitude related to these) along thousands of sensing points over tens of kilometers of fiber.

Fiber sensing schemes based on Brillouin scattering, particularly sensors based on Brillouin Optical Time Domain Analysis (BOTDA) have become one of the most-established solutions to monitor large structures. A standard BOTDA sensor is typically able to inspect distances of 30-50 km with a spatial resolution of 1-2 m. However, some specific applications, such as oil & gas pipelines deployed in remote and not power-supplied areas may require measuring over longer distances (e.g. circa 100 km), whereas other may require increasing the number of sensing points by augmenting the system spatial resolution. Therefore, finding methods to increase the performance of the sensors (i.e. the system signal-to-noise ratio) turns critical.

This thesis aims to provide a deep understanding of the current limitations of the BOTDA technique. For this purpose, classical limiting factors are studied, such as modulation instability, pump depletion or noise-related limits in detection. Fundamental resolution boundaries are also analyzed, where the lower feasible resolution is said to be ~1 m for standard schemes. Additionally, a thorough investigation of the non-local effects arising in dual-probe-sideband BOTDA (DSB-BOTDA) setups is provided, where strong distortions of both the pump pulse and the retrieved Brillouin gain and loss curves are reported, preventing the system from working at conventional probe powers (already present at -5 dBm per sideband).

The first experimental results here demonstrated verify the virtues of applying a new detection scheme to BOTDA sensors: the balanced detection. Its successful application has

rendered a doubling in the amplitude of the BOTDA traces, while improving the SNR in a factor $\sqrt{2}$. In addition, it has been proven to be an effective solution to cancel out common-mode noise, and hence, by combining balanced detection with Raman amplification it has verified a strong elimination of the RIN transfer delivered by the Raman lasers.

In pursuance of avoiding the non-local effects induced by the probe in DSB-BOTDA, a novel technique that effectively overcomes such restrictions has been presented, allowing a significant increase of the used probe power, and consequently, considerably augmenting the system SNR. Such interesting feature has led to two major state-of-the-art records: first, a BOTDA sensor that reaches 100 km with a 2 m spatial resolution has been achieved without using any kind of amplification and in a conventional acquisition time; secondly, a sensor that resolves, for the first time to our knowledge, 1,000,000 sensing points in a time-domain Brillouin sensor, featuring 1 cm of spatial resolution over 10 km of fiber and keeping the acquisition time in a few minutes.

In summary, the work presented in this thesis represents a thorough study of the limitations of the BOTDA technique, where advanced improvement approaches are proposed, significantly increasing the system performance, both in terms of resolution and sensing range. This way, the worldwide growing infrastructural needs can be addressed in a more efficient and reliable way.

Resumen

A fin de dar cabida a todas las necesidades de la sociedad de hoy en día, tanto energéticas, como de comunicaciones, transporte o habitacionales, surgen gran número de infraestructuras. Presas, puentes, carreteras o vías férreas deben garantizar un continuo y correcto funcionamiento, y por tanto, urge preservar y controlar la integridad de dichas instalaciones. Los sensores distribuidos de fibra óptica son particularmente adecuados para este tipo de aplicaciones, ya que permiten obtener medidas de deformación, temperatura y/o vibraciones (o cualquier magnitud física relacionada con las mismas) de miles de puntos sensores a lo largo de decenas de kilómetros de fibra óptica.

Los sensores de fibra óptica basados en scattering Brillouin, en particular los fundamentados en el Análisis en el Dominio del Tiempo del efecto Brillouin (BOTDA, por sus siglas en inglés) se han convertido en una de las soluciones por excelencia para monitorizar grandes infraestructuras. Un sensor BOTDA convencional es capaz de medir, típicamente, sobre distancias de 30-50 km con una resolución espacial de 1-2 m. Sin embargo, ciertas aplicaciones, tales como gasoductos/oleoductos instalados en áreas de difícil acceso y sin posibilidad de alimentación eléctrica podrían requerir medir distancias más largas (del orden de los 100 km), mientras que otras, por el contrario, podrían necesitar aumentar el número de puntos sensibles en la fibra, es decir, incrementar la resolución espacial del sensor. Por tanto, urge encontrar métodos que permitan aumentar las capacidades actuales de dichos sensores, en otras palabras, aumentar la relación señal-ruido (SNR, por sus siglas en inglés) de los mismos.

El presente trabajo de tesis aporta un profundo estudio de las limitaciones actuales de la técnica BOTDA. Se han analizado, por tanto, los límites clásicos, tales como la inestabilidad de modulación, el agotamiento de bombeo o efectos relacionados con el ruido en detección. Asimismo, se define el límite técnico inferior en cuanto a resolución espacial, el cual está en torno a 1 m en esquemas convencionales. A su vez, se ha realizado un estudio detallado de los efectos no-locales que surgen en montajes con sonda de doble banda lateral (DSB, por sus

siglas en inglés), donde se han identificado distorsiones significativas tanto en la señal de bombeo como en las curvas de ganancia y atenuación Brillouin obtenidas, limitando el correcto funcionamiento de los sensores BOTDA para valores convencionales de potencia de la señal de sonda (ya presentes para una potencia de -5 dBm por banda).

El primer resultado experimental que se presenta es la aplicación de la detección diferencial a sistemas BOTDA. La aplicación de la misma conlleva un aumento de la amplitud de las trazas BOTDA en un factor 2, mientras que mejora la SNR en un factor $\sqrt{2}$. Asimismo, se ha mostrado particularmente eficaz a la hora de eliminar ruidos en modo-común presentes en el sistema, y por tanto, combinando este nuevo esquema de detección con la amplificación Raman se ha verificado una reducción considerable del ruido relativo en intensidad (RIN, por sus siglas en inglés) transferido a las señales BOTDA por los láseres Raman.

Por último, a fin de evitar los ya mencionados efectos no-locales provocados por la señal de sonda en BOTDA, se ha propuesto una novedosa y efectiva técnica de barrido, la cual permite aumentar la potencia de sonda, y por tanto, mejorar la SNR del sistema. Tal característica ha permitido alcanzar dos importantes records en el estado actual de la tecnología: en primer lugar, se ha conseguido un sensor BOTDA capaz de medir sobre 100 km de fibra con una resolución de 2 m, sin haber necesitado combinarlo con ningún otro tipo de técnica de amplificación y en un tiempo de adquisición convencional; en segundo lugar, se ha demostrado un sensor capaz de resolver, por primera vez, 1.000.000 de puntos sensibles en un sensor Brillouin basado en el dominio del tiempo, es decir, una resolución espacial de 1 cm a lo largo de 10 km de fibra estándar y en un tiempo de adquisición de pocos minutos.

En resumen, esta tesis presenta un estudio profundo de las limitaciones de la técnica BOTDA, proponiendo técnicas avanzadas que se traducen en una mejora considerable de las prestaciones actuales de los sensores, tanto en términos de resolución, como en alcance de medida. De este modo, se pretende dar una mejor y más eficaz respuesta a las necesidades de monitorización de las infraestructuras presentes hoy en día.

Contents

Chapter 1:
Introduction

1.1. Motivation

Nowadays, a significant number of infrastructures are required in order to properly fulfill the needs of the world population. From bridges, dams or railroads, to offshore wind-farms, sport facilities or highways, all of the infrastructures should guarantee a proper functioning in order to correctly provide the respective services they are designed for, and most importantly, for security reasons. Hence, there is an urgent need of monitoring such civil infrastructures.

Traditionally, electronic sensors have covered this necessity. However, these may not be suitable for some applications, such as railways or energy transportation, where there might be a strong presence of electromagnetic fields disturbing the readings of the sensors. In the past few decades, optical fiber sensors have become an appealing approach in monitoring large infrastructures due to their numerous advantages:

- The optical fiber itself acts as a sensor, i.e. already-deployed dark fibers can turn into distributed sensors.

- Fibers are lightweight, flexible and can be embedded in materials during fabrication process. This is of particular interest for Structure Health Monitoring (SHM) of aerospace and avionic structures, among other applications.
- Standard telecom fibers present low signal attenuation ($0.2\ dB/km$ for $\lambda = 1550\ nm$), which means the signals of interest can travel along several tens of kilometers of fiber, making them highly suitable for monitoring large distances.
- Optical fibers are immune to electromagnetic noise, making them adequate for certain applications, such as smart grid monitoring.
- Standard telecom fibers are made of silica, and thus, they can resist extreme temperature, which makes them very appropriate for sensing in harsh environments.
- Optical fibers are dielectric, which makes them extremely appealing for sensing in areas where electrical sensors should be avoided (i.e. with high risk of explosion).

All of these features have caused an important growth in the number of sensing applications covered by optical fiber systems. Among the optical fiber sensing schemes, distributed optical fiber sensors have attracted a great amount of interest from both the industry and the academia, for they allow measuring several thousand sensing points along tens of kilometers of a single optical fiber, by means of a unique interrogation unit.

Systems based on Brillouin scattering are a well-established option to monitor large civil infrastructures. In particular, the Brillouin Optical Time Domain Analysis (BOTDA) approach has become one of the most popular distributed sensing techniques. The BOTDA technique was first proposed in 1989, and since then, a vast and growing number of research groups and institutions, as well as several industrial firms, have put their effort in improving the sensing performance. Nowadays, a standard BOTDA sensor is able to continuously monitor distances of typically 30-50 km with 1-2 m of spatial resolution.

Of course, there is a huge interest in increasing the sensing range of the system, as well as its spatial resolution, in order to cover larger distances of fiber while resolving more sensing

points. In this thesis, a great effort is put on thoroughly studying the current limitations of the technique and providing a detailed understanding of the state-of-the-art. This allows to address such limits, and hence, be able to increase the performance of the sensors. The achieved advancements have reported, among others, two major results: first, a BOTDA sensor that reaches 100 km with a 2 m spatial resolution has been achieved without using any kind of amplification and in a conventional acquisition time; and ultimately, a sensor that resolves, for the first time to our knowledge, 1,000,000 sensing points in a time-domain Brillouin sensor, featuring 1 cm of spatial resolution over 10 km of standard fiber.

1.2. Objectives

The main goal of this thesis is to improve the current state-of-the-art of BOTDA sensors by identifying, studying and tackling the limitations of the technique. Therefore several main topics arise:

- In first place, perform a thorough study, both theoretical and experimental, of the current limitations of the conventional BOTDA sensing scheme, where the contribution of the different key parameters in BOTDA is to be considered (pump and probe power, interaction length, fiber distance, etc.).
- To study and apply a different detection scheme on BOTDA sensors: the balanced detection. A balanced detection scheme between the gain and loss bands of a Brillouin sensor is to be analyzed and implemented, verifying the expected improvement in sensing performance.
- Identify and tackle the draw-backs of a widely spread solution to distributed optical fiber sensors, the Raman assistance. Applying balanced detection to a Raman assisted BOTDA would certainly improve its performance by effectively mitigating the RIN transfer.

- Perform an exhaustive study of the effects of mid- to high-probe powers in dual-probe sideband BOTDA schemes for the conventional pump-probe frequency offset scanning method.
- Propose and validate an effective solution to avoid non-local effects arising in dual-probe-sideband BOTDA schemes. By solving such limitation, the signal-to-noise ratio of the system can be significantly improved, and hence, the overall performance. Particularly, studying the applicability of such solution in high-resolution schemes, where guaranteeing avoiding any detrimental effect on the pump pulse turns critical.

1.3. Thesis Outline

According to the objectives previously depicted, the work in this thesis has been structured in the following chapters:

- Chapter 2: “Inelastic Scattering Phenomena in Optical Fibers” covers the basic theoretical fundamentals of the physical processes that take place within the fiber when implementing a BOTDA sensor. It focuses on the principal non-linear effects used throughout this thesis, particularly Stimulated Brillouin Scattering. A theoretical introduction to Raman scattering is also provided.
- Chapter 3: “Brillouin Optical Time Domain Analysis” focuses on the working principle enabling the sensing technique, its main limitations and the current state-of-the-art, providing an insight on some of the most-used approaches to enhance the performance.
- Chapter 4: “Balanced Detection in BOTDA” describes the fundamentals of the application of a balanced detection scheme among the Brillouin gain and loss bands, highlighting the general benefits it renders, as well as the major enhancement provided when combined with Raman amplification.

- Chapter 5: “Non-local Effects in a Dual-Probe-Sideband BOTDA” studies, both theoretically and experimentally the detrimental non-local effects arising in dual-probe-sideband BOTDA, for two different probe power regimes. The severe consequences of such non-local effects in BOTDA sensors are thoroughly studied here.
- Chapter 6: “Novel Scanning Method for Distortion-free BOTDA Measurements” proposes a solution to avoid the detrimental non-local effects presented in the previous chapter. Applying this solution to a BOTDA allows substantially increasing the probe power (roughly one order of magnitude), rendering a significant signal-to-noise ratio enhancement. Such enhancement allows achieving remarkable performances, both as a long-range sensor (100 km of sensing range with 2 m of spatial resolution), and ultimately, when combining it with the Differential Pulse-width Pair (DPP) technique, as an extremely high-resolution system over mid-sensing ranges (e.g. 10 cm of spatial resolution over 10 km of fiber), which implies resolving an extremely large number of independent sensing points (~1,000,000).
- Lastly, the conclusions and open lines of this work are briefly provided in Chapter 7.

Chapter 2:
Inelastic Scattering Phenomena in Optical Fibers

2.1. Introduction

When an incident light travels through any medium it suffers a deviation from its original trajectory due to the non-uniformities in the molecular structure of the material. This physical process is known as scattering of light. If light is considered as an electromagnetic wave travelling along a dielectric medium, such as the optical fiber, the scattering can be considered linear (spontaneous) whenever the incident light power is below a certain threshold, for which the properties of the medium are not modified by the incident light. When a sufficiently intense incident light is applied, it induces changes in the refractive index of the medium, hence, causing non-linear (stimulated) scattering phenomena. The scattering process will remove some photons of the incident light when encountering a non-homogeneous medium, generating at the same time scattered photons that may be shifted in direction, phase and/or frequency.

Depending on the energy transfer between the medium and the scattered photons, the following distinction can be made:

- **Elastic Scattering**: The scattered photons maintain their energy, thus, keeping the same frequency as the incident beam.
- **Inelastic Scattering**: In this case, the scattered photons do suffer a frequency shift compared to the original incident light photons, since there is an energy transfer between the light and the material (photons may give or receive energy). If the scattered photons are downshifted in frequency, it is usually defined as the Stokes component. It is called "Stokes wave" after Irish physicist George Stokes, who found the frequency downshift in the process of luminescence in the 19th century. Conversely, if they are frequency upshifted, they are labelled as the anti-Stokes component.

According to the previous classification, made in terms of energy transfer between the medium and the incident light, the following scattering phenomena are depicted:

- **Rayleigh Scattering**: It is an elastic process, where the scattered photons do not suffer any frequency shift. The scattering process is due to the interaction between light and the non-homogeneities of the molecular structure of the medium.
- **Raman Scattering**: It is a strong inelastic scattering process due to the interaction between photons and optical phonons. It is generated by the interaction between the incident light and molecular vibrational modes of the material.
- **Brillouin Scattering**: This inelastic scattering arises from the interaction between light and moving pressure waves, due to acoustic phonons, which frequency shift is determined by the acoustic velocity in the medium.

Although the work developed in this thesis is not based on spontaneous scattering phenomena but on the stimulated processes, they are introduced to further support the detailed explanation of the stimulated processes. A comprehensive representation of the spontaneous phenomena have been presented in Figure 2.1, which helps having a full picture of the scattering phenomena in optical fibers. In it, it can be easily observed how weak Brillouin and Raman scattering are, compared to Rayleigh scattering, as well as the frequency spacing among them.

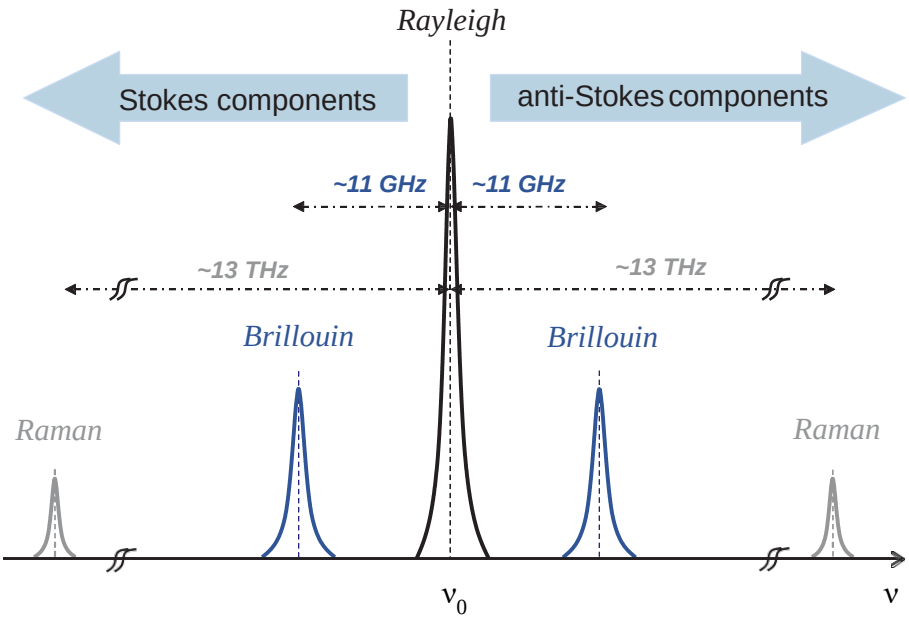

Figure 2.1: Scattering phenomena occurring in optical fibers when a coherent light beam at frequency ν_0 is injected [1].

The work developed in this thesis is focused in two inelastic and non-linear scattering effects: the stimulated Brillouin and Raman scattering (SBS and SRS respectively). For sufficiently intense incident fields, the scattering phenomena becomes non-linear, which means, the scattered photons not only come from the incident beam, but also from the medium. In this case, the scattering effect is reinforced and becomes intensity-dependent [2].

However, not only the power of the incident light drives the intensity of the scattering effect. The cross-sectional area of the optical fiber (A_{eff}), along with the distance in which the incident light is interacting with the medium (L_{eff}) should also be taken into consideration when studying the non-linear effects. The following section further analyzes these two parameters.

2.2. Non-linear Effective Area and Length

As previously said, the appearance of non-linear effects depends not only on the intensity of the incident light, but also on the total transmission length and the cross-sectional area. The longer the fiber length, the more the light interaction and the more severe the non-linear effects. As the light propagates along the fiber, its power decreases because of the intrinsic fiber attenuation. Hence, the impact of non-linear effects is higher at the beginning of the fiber link, and diminishes as the signal propagates. The effective length (L_{eff}) is said to be the length up to which power is assumed to be constant [3].The optical power at a distance z along the fiber is given by:

$$P(z) = P_{in} \exp(-\alpha z) \tag{2.1}$$

where P_{in} is the input power (power at $z = 0$) and α is the attenuation coefficient of the fiber. For a fiber link of length L, the effective length is defined as:

$$P_{in} L_{eff} = \int_0^L P(z) dz \tag{2.2}$$

Using equations (2.1) and (2.2), the effective length is obtained as:

$$L_{eff} = \frac{1 - \exp(-\alpha L)}{\alpha} \tag{2.3}$$

For short fiber lengths it is usually considered $L_{eff} \simeq L$. However, for long fiber ranges, where $L \gg 1/\alpha$, it turns out that $L_{eff} \simeq 1/\alpha$. If the typical fiber attenuation $\alpha = 0.22\ dB/km$ ($\lambda \approx 1550\ nm$) is considered, it yields $L_{eff} \approx 20$ km for long fiber ranges.

Additionally, since the appearance of non-linear effects increases with the incident light intensity, where such intensity is inversely proportional to the area of the fiber core, it is worth analyzing the role the fiber cross-sectional area plays in the appearance of such nonlinearities. Considering the power is not uniformly distributed within the cross-section of the fiber, it is reasonable to define the effective cross-sectional area (A_{eff}). The A_{eff} is related to the actual area (A) and the cross-sectional distribution of intensity $I(r,\theta)$ in the following way [3], [4]:

$$A_{eff} = \left[\frac{\int_r \int_\theta r dr d\theta I(r,\theta)}{\int_r \int_\theta r dr d\theta I^2(r,\theta)} \right] \tag{2.4}$$

where r and θ denote the polar coordinates.

Particularly, the concept of non-linear effective length will play a key role in the theoretical and experimental analysis depicted in the forthcoming Chapter 5 and Chapter 6 (since all the fibers used along this thesis are geometrically equivalent, i.e. having the same cross-sectional area).

2.3. Raman Scattering

The interaction of an incident light with the molecular vibrational modes of the medium generates the so-called Raman scattering. The incident light is inelastically scattered ($\sim 10^{-6}$ of the incident photons are scattered) when interacting with the medium, which means that a fraction of the incident light suffers a frequency shift to higher and/or lower frequencies. The Raman scattering is a well-known and undesired effect in optical communication systems, since it can generate and amplify noise in the communication channels. However, it also provides interesting features, such as the ability to determine the energy of the vibrational modes in the medium by inspecting the Raman gain spectrum, allowing precise characterization of chemicals and materials. In optical fibers it can also be used as a distributed temperature sensor and as a signal amplifier, compensating the intrinsic fiber losses and permitting increasing the performance of distributed optical fiber sensors, as it will be studied in the forthcoming sections.

2.3.1 Spontaneous Raman Scattering (SpRS)

The spontaneous Raman scattering was first described by C. V. Raman in 1928 as *"A new radiation"* [5] observed in a liquid medium, but it arises in every medium. It occurs due to the interaction of the light with the molecular vibrational modes of the material.

Raman scattering is commonly explained in terms of quantum energy levels. In Stokes Raman scattering, a molecule located in a ground level vibrational state [state '1' in Figure 2.1(a)] is excited by an incident photon (pump) with a frequency ω_p and transits to a higher virtual state. Then, the molecule transits to an intermediate state of energy [state '2' in Figure 2.1(a)], higher than the original ground state, emitting a new photon at a frequency ω_S (lower than the one of the pump photon). The energy and momentum differences between the pump (ω_p) and the emitted photon (ω_S) are compensated by the molecule, which absorbs a phonon of frequency Ω_R. Therefore, $\omega_S = \omega_p - \Omega_R$, where Ω_R is the frequency associated to the vibrational modes of the material. On the other hand, for the anti-Stokes Raman process [Figure 2.1(b)], if a molecule already has a given vibrational energy [state '2' in Figure 2.1(b)], then, the incident photon is able to absorb an amount of energy from the medium, which turns into emitting a photon at an upshifted frequency, which also complies with the energy and momentum preservation ($\omega_{AS} = \omega_p + \Omega_R$). The frequency shift associated to the vibrational modes of the material (Ω_R) is commonly known as Raman Frequency Shift (RFS), which for silica is typically $\simeq$ 13 THz.

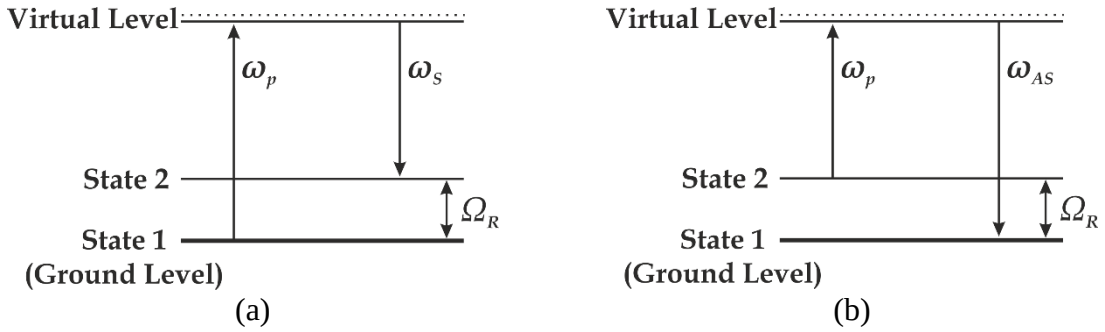

Figure 2.2: Illustration of the spontaneous Raman scattering process: (a) Stokes scattering; (b) anti-Stokes scattering [6].

The transition rates at which the Stokes (W_S) and anti-Stokes (W_{AS}) scatterings occur in thermal equilibrium are proportional to the population of the energy states [7], following that:

$$W_S \propto N_0(1+N_\Omega) \tag{2.5}$$

$$W_{AS} \propto N_0 N_\Omega \tag{2.6}$$

where N_0 is the incident photon number, proportional to the light intensity (i.e. $N_0 \propto |E_0|^2$) and N_Ω is the Bose-Einstein thermal population factor:

$$N_\Omega = \frac{1}{\exp(h\Omega_R / k_B T_{abs}) - 1} \tag{2.7}$$

where h is the Planck constant, k_B is the Boltzmann factor, Ω_R is the vibrational frequency and T_{abs} is the absolute temperature. The ratio of the unbalance between the Stokes and anti-Stokes intensities is $\exp(-h\Omega_R / k_B T_{abs})$, which demonstrates that the anti-Stokes components tend to equal the Stokes component at high temperatures and that disappears when T_{abs} tends to 0.

This property has been used to develop distributed temperature sensors, where the Raman anti-Stokes intensity is used to identify the temperature distribution and the Stokes component, which is practically temperature independent [8], and can be employed as reference for local loss variations.

2.3.2 Stimulated Raman Scattering (SRS)

If an intense pump light (ω_p) is present in the medium, it generates two side processes through Raman scattering, the Stokes (ω_S) and anti-Stokes (ω_{AS}) component, as depicted in the previous section. These two processes manifest shifted a certain frequency (Ω_R) from the incident pump radiation frequency (ω_p). If another field is introduced in the medium at a frequency $\omega_S = \omega_p - \Omega_R$ (see Figure 2.3), i.e. matching the Raman Stokes frequency, it will interact with the pump through Raman scattering, modulating at the same time the total intensity of the molecular vibration.

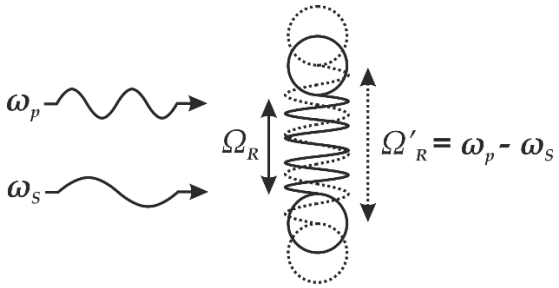

Figure 2.3: Illustration of the stimulated Raman scattering (SRS) with a pre-existent component at the Stokes frequency (ω_S) [6].

The modulated intensity coherently excites the molecular oscillation at $\Omega'_R = \omega_p - \omega_S$, that at the same time amplifies the Stokes wave, turning into a self-sustained feedback process that generates a stronger molecular vibration and an amplified Stokes field. The wave at the Stokes frequency can be introduced in the fiber either co- or counter-propagating with the pump wave.

This enhanced effect is called Stimulated Raman Scattering (SRS) and it was first accidentally discovered by Woodbury and Ng [9] in 1962, and then described in detail by Eckhardt *et al.* [10] later that year. SRS is commonly exploited as a distributed signal amplifier, where a sufficiently powerful pump wave, at a frequency ω_p, will amplify a signal at a frequency ω_S (Stokes wave). Along this thesis, Raman amplification has been used to boost the performance of the developed sensors.

2.3.2.1 Raman Gain Spectrum

In a simple approach valid under the Continuous-Wave (CW) or quasi-CW conditions, the Stokes wave is described by [11]:

$$\frac{dI_S}{dz} = g_R(\Omega) I_p I_S \tag{2.8}$$

where I_S is the Stokes intensity, I_p is the pump intensity and g_R is the Raman gain coefficient. The Raman Gain Spectrum (RGS) $g_R(\Omega)$, where Ω represents the frequency difference between the pump and Stokes waves, is the most important parameter when describing SRS.

It depends on the composition of the material, which makes it vary depending on the present dopant [12]. In crystals, the material vibrational modes have well defined energies and are associated with specific Raman frequency shifts. In this case, the Raman gain spectrum is typically a set of narrowband peaks at well-defined frequencies. In amorphous materials, however, the energy of the vibrational modes can be wide enough so that different bands can overlap, generating a continuum. This is the case of amorphous fused silica (the main material of silica fibers), whose RGS is a continuum that extends up to ~ 40 THz [12], with a maximum peak at ~ 13 THz and a Full Width at Half Maximum (FWHM) of ~ 7 THz, as it can be seen in Figure 2.4.

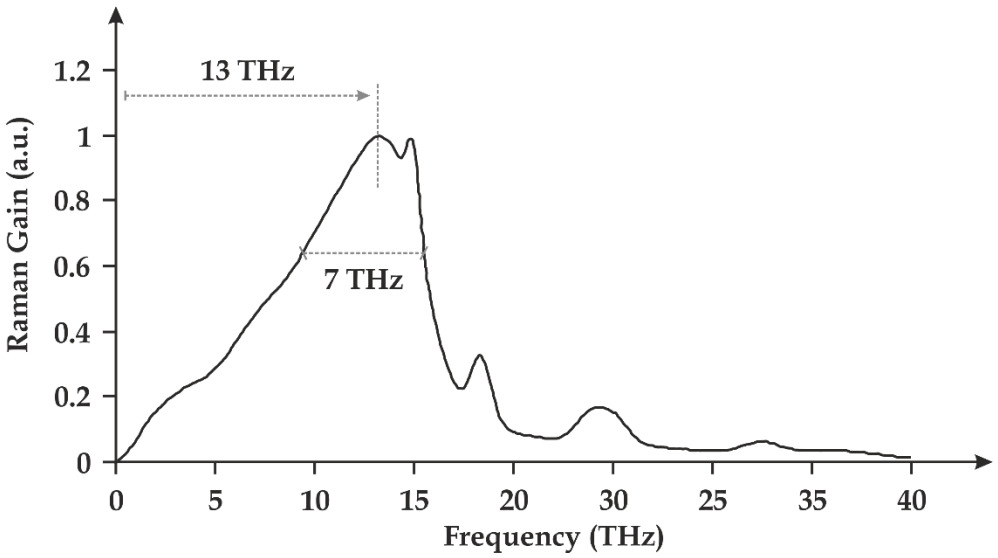

Figure 2.4: Illustration of the Raman gain spectrum in silica fibers [6], [12].

If a powerful enough Raman pump is employed and a signal is placed within the RGS, the signal of interest would experience a distributed amplification along the entire fiber. This interesting feature will be further exploited in this thesis as to increase the sensing performance of Brillouin-based distributed sensors, as it will be explained in Subsection 3.4.2.

2.3.2.2 Coupled Intensity Equations for SRS

When a Raman pump (ω_p) is used to amplify a signal at the Stokes frequency (ω_S) along an optical fiber by means of SRS, the evolution of the intensities of the two waves, in the CW case, are described by the two following coupled equations [12] :

$$\frac{dI_S}{dz} = g_R(\Omega) I_p I_S - \alpha_S I_S \tag{2.9}$$

$$\frac{dI_p}{dz} = -\frac{\omega_p}{\omega_S} g_R(\Omega) I_p I_S - \alpha_p I_p \tag{2.10}$$

where α_p and α_S are the fiber losses at the pump and Stokes frequencies respectively.

In the absence of losses ($\alpha_p = \alpha_S = 0$), and considering the processes through which photons appear and disappear from each beam, it can be merely concluded that the total number of photons in the pump and Stokes beams remains constant during SRS [12]. That is represented by the factor ω_p / ω_S in Eq. (2.10).

2.3.2.3 Raman Threshold

Although pump depletion must be included for a complete description of SRS, it can be neglected for the purpose of estimating the Raman threshold [12][13]. Equation (2.10) can be easily solved if we neglect the first term on its right-hand side, which is responsible for pump depletion, i.e., the power lost due to attenuation is already higher than the depletion. If we substitute the solution in equation (2.9) and solve it, we obtain:

$$I_S(L) = I_S(0) \exp(g_R(\Omega) I_0 L_{eff} - \alpha_S L) \tag{2.11}$$

where I_0 is the incident pump intensity at $z = 0$ and L_{eff} is the effective length as expressed in Eq. (2.3).

Equation (2.11) requires an input intensity $I_S(0)$ at $z = 0$. In practice, SRS builds up from spontaneous Raman scattering occurring throughout the fiber length. It has been shown that

this process is equivalent to injecting one fictitious photon per mode at the input end of the fiber [13][12]. The power needed to make the scattered field comparable to the pump field is what is known as Raman threshold (P_{th}^{SRS}), and its value is given by:

$$P_{th}^{SRS} = 16\frac{A_{eff}}{g_R L_{eff}} \tag{2.12}$$

For standard telecommunication optical fibers working at 1550 nm ($A_{eff} = 80\mu m^2$, $L_{eff} \approx$ 20 km and $g_R = 6.6\times10^{-14}$ m/W) the Raman threshold will be ~970 mW for forward SRS. In the case of backward SRS, the numerical factor 16 is replaced with 20 [12], therefore, P_{th-bw}^{SRS} will equal approximately ~1.2 W.

2.4. Brillouin Scattering

As deeply analyzed in previous sections, the interaction of light with optical phonons generates the so-called Raman scattering. In this case, the interaction of an incident light with acoustic phonons (instead of optical ones) is known as Brillouin scattering. It was named after French physicist Léon Brillouin, who theoretically predicted light scattering from thermally excited acoustic waves in 1922 [14]. The scattered photons are up and downshifted in frequency (anti-Stokes and Stokes components respectively), compared to the frequency of the incident photons. Compared to Raman scattering, Brillouin Frequency Shift (BFS) manifests three orders of magnitude below the RFS, in this case, ~ 11 GHz (instead of the ~ 13 THz of RFS). Such difference comes from the fact that the optical phonons of the Raman scattering have much higher energy than the acoustic phonons involved in Brillouin scattering. Brillouin scattering, as well as Raman, was first identified as a major deleterious effect in optical communication systems when utilizing sufficiently powerful signals. However, it can also be useful for making fiber-based Brillouin lasers and amplifiers [12]. Particularly in this thesis, we will exploit another interesting feature, which is, its capability of sensing temperature and strain along tens of kilometers of fiber in a distributed manner.

2.4.1 Spontaneous Brillouin Scattering (SpBS)

Spontaneous Brillouin scattering arises from the presence of thermally excited acoustic waves in the material, which yields in density fluctuations in the medium. From a quantum-mechanical point of view, a photon from an incident light wave is transformed into a scattered photon and an acoustic phonon. Thus, in order to properly understand this scattering phenomenon, it is convenient to analyze the acoustic wave behavior in optical fibers.

From the acoustic point of view, a silica-based optical fiber can be considered an homogeneous, isotropic, viscous and compressible fluid [15]. First of all, let us consider the following acoustic wave (pressure wave, Δp) equation:

$$\frac{\partial^2 \Delta p}{\partial t^2} - \Gamma \nabla^2 \frac{\partial \Delta p}{\partial t} - V_A^2 \nabla^2 \Delta p = 0 \tag{2.13}$$

where Γ is the damping parameter of the material and V_A is the acoustic velocity in the medium. The intensity of the acoustic wave evolves along the fiber following:

$$\left|\Delta p(z)\right|^2 = \left|\Delta p(0)\right|^2 \exp(-\alpha_a z) \tag{2.14}$$

in which α_a is the acoustic absorption coefficient, defined as:

$$\alpha_a = \frac{\left|\mathbf{q}\right|^2 \Gamma}{\nu_a} = \frac{\Gamma_B}{\nu_a} \tag{2.15}$$

where $\Gamma_B = \left|\mathbf{q}\right|^2 \Gamma$ is the acoustic damping coefficient, which is inversely proportional to the acoustic damping time (τ_p), also commonly known as the average lifetime of the acoustic phonon in the medium:

$$\tau_p = \frac{1}{\Gamma_B} \tag{2.16}$$

The average phonon lifetime ($\tau_p \approx 6$ ns) will play a key role in the development of Brillouin distributed sensors, limiting the spatial resolution of the system, as it will be explained in the forthcoming Chapter 3.

In addition, the interaction of an incident light with acoustic waves in the medium is given by [11]:

$$\nabla^2\mathbf{E}-\frac{n^2}{c^2}\frac{\partial^2\mathbf{E}}{\partial t^2}=\mu_0\frac{\partial^2\mathbf{P}}{\partial t^2} \tag{2.17}$$

where n is the refractive index of the medium, c is the speed of light in vacuum and μ_0 is the magnetic permittivity in vacuum. The right-hand side term of the equation is the non-linear polarization component. The polarization itself ($\mathbf{P}$) is defined by:

$$\mathbf{P}(\mathbf{r},t)=\epsilon_0\left(\frac{\partial\epsilon}{\partial\rho}\right)\left(\frac{\partial\rho}{\partial p}\right)_S\Delta\boldsymbol{p}(\mathbf{r},t)\mathbf{E}_0(z,t)=\epsilon_0\gamma_e C_S\Delta\boldsymbol{p}(\mathbf{r},t)\mathbf{E}_0(z,t) \tag{2.18}$$

where ϵ_0 is the dielectric permittivity of free space, γ_e is the electrostrictive constant of the medium and C_s is the adiabatic compressibility. The polarization depends on the density variation (Δp) of the thermally excited pressure disturbance:

$$\Delta p=\Delta p_0\exp[i(-\mathbf{q}\cdot\mathbf{r}-\Omega_a t)]+c.c. \tag{2.19}$$

where $\Omega_a=V_A|\mathbf{q}|$ is the frequency of the acoustic wave and $\mathbf{q}$ the scattered wavevector.

By combining Eq. (2.17), (2.18), and (2.19), it can be found that the scattered field must obey the following wave equation:

$$\begin{aligned}\nabla^2\mathbf{E}-\frac{n^2}{c^2}\frac{\partial^2\mathbf{E}}{\partial t^2}=-\frac{\gamma_e C_s}{c^2}\{&(\omega-\Omega_a)^2E_0\Delta p^*\exp[i(\mathbf{k}-\mathbf{q})\cdot\mathbf{r}-i(\omega-\Omega_a)t]+\\&+(\omega+\Omega_a)^2E_0\Delta p\exp[i(\mathbf{k}+\mathbf{q})\cdot\mathbf{r}-i(\omega+\Omega_a)t]+c.c.\}\end{aligned} \tag{2.20}$$

where E_0, ω and $\mathbf{k}$ are the amplitude, frequency and wavevector of the incident light respectively.

On the right-hand side term of Eq. (2.20) it can be observed that the first expression corresponds to Brillouin Stokes scattering, where:

$$\mathbf{k}'=\mathbf{k}-\mathbf{q} \tag{2.21}$$

$$\omega'=\omega-\Omega_a \tag{2.22}$$

The second part of the right-hand side term of Eq. (2.20) describes the Brillouin anti-Stokes process, where:

$$\mathbf{k}' = \mathbf{k} + \mathbf{q} \tag{2.23}$$

$$\omega' = \omega + \Omega_a \tag{2.24}$$

where the wavevector and the frequency of the scattered and the incident waves are related by:

$$\omega = |\mathbf{k}| \frac{c}{n} \tag{2.25}$$

$$\omega' = |\mathbf{k}'| \frac{c}{n} \tag{2.26}$$

The energy of the incident photons is $E_0 = h\omega$, while the energy of the acoustic phonons is $E_0 = h\Omega_a$, where h is the Plank's constant. Since the frequency of the phonon is negligible compared to the frequency of the photon (10 GHz *vs.* 200 THz), the energy of the phonon is also negligible compared to the one of the photon. Hence, the interaction between the photon and the phonon renders an almost unchanged energy and frequency of the scattered photon. Thus, the absolute value of the wavevector of the photon remains constant ($|\mathbf{k}'| \approx |\mathbf{k}|$) for both Stokes and anti-Stokes components. Its direction, though, might change significantly.

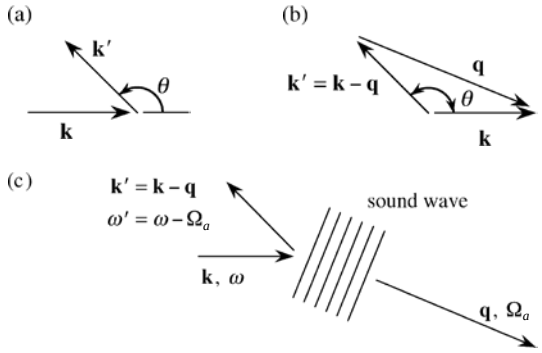

Figure 2.5: Illustration of the Brillouin Stokes scattering [11].

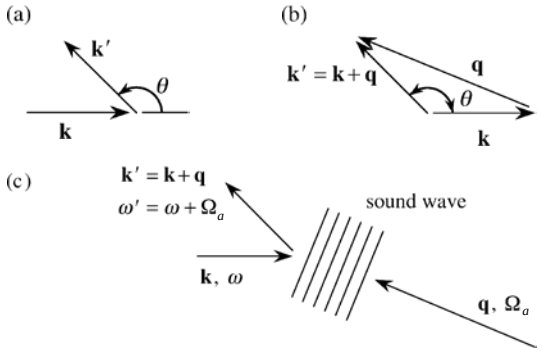

Figure 2.6: Illustration of the Brillouin anti-Stokes scattering [11].

The interaction between the incident light and the acoustic wave is fully depicted in Figure 2.5 and Figure 2.6 (Stokes and anti-Stokes scattering respectively). Figure 2.5(a) and Figure 2.6(a) show the relation of the wavevectors of the incident and scattered fields, where θ is the angle between them. Figure 2.5(b) and Figure 2.6(b) represent the relation between the wavevectors of the acoustic, incident and scattered waves. According to the latter, the scattered

photons are shifted a certain frequency (Ω_a), with a certain direction, and counter- or co-propagating to the incident light [Figure 2.5(c) and Figure 2.6(c)] [11].

The concrete direction of the scattered photons is given by the angle θ between the incident light and the acoustic wave. Its relation is given by:

$$\left|\mathbf{k}'-\mathbf{k}\right| = 2k\ sin\left(\frac{\theta}{2}\right) \tag{2.27}$$

where θ varies from 0 to π.

As a result of the scattering process, the energy of the photon is changed according to:

$$\Delta E = qV_A = 2kV_A\ sin\left(\frac{\theta}{2}\right) \tag{2.28}$$

which yields in a change in frequency proportional to:

$$\Omega_a = \frac{4\pi n V_A}{\lambda_p} sin\left(\frac{\theta}{2}\right) \tag{2.29}$$

Since the optical fiber geometry only allows for light propagation in two directions (forward and backwards), only the light scattered at angles 0 and θ propagates. From Eq. (2.29), it can be inferred that the light scattered forward ($\theta = 0$) experiences no frequency shift [16]. Actually, if $\theta = 0$, Eq. (2.28) renders a frequency and wavevector of the acoustic phonon equal to zero. In the case of backward scattering ($\theta = \pi$), the wavevector of the phonon is equal to $2k$, giving the following change in the frequency of the scattered photon, which maximum peak is noted by Ω_B:

$$\Omega_B = \frac{4\pi n V_A}{\lambda_p} \tag{2.30}$$

which can be reformulated in order to obtain the classical expression for the so-called Brillouin frequency shift (BFS):

$$\nu_B = \Omega_B \big/ 2\pi = \frac{2nV_A}{\lambda_p} \tag{2.31}$$

Due to the finite duration of the phonon lifetime ($\tau_p \approx 6$ ns) [17], it should be noted that, in the frequency domain, the Brillouin components are not strictly monochromatic (see Figure 2.7) and suit a Lorentzian spectral profile [12], given by:

$$g_B(\nu) = g_0 \frac{(\Delta\nu_B / 2)^2}{(\nu - \nu_B)^2 + (\Delta\nu_B / 2)^2} \tag{2.32}$$

where $\Delta\nu_B = \Gamma_B / 2\pi$ is the FWHM or Brillouin spectral linewidth.

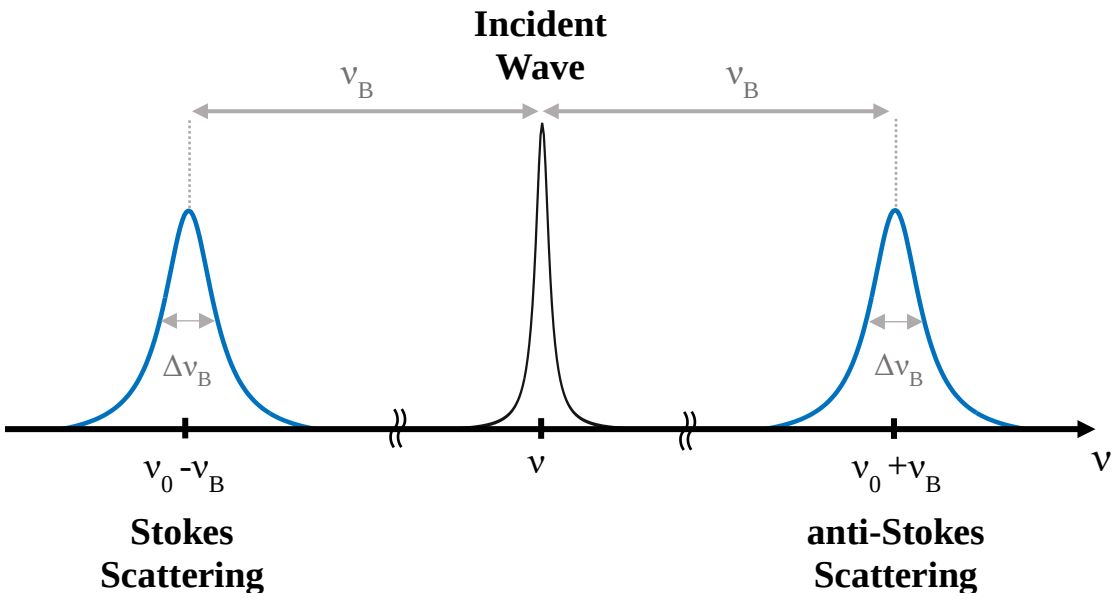

Figure 2.7: Illustration of the Brillouin Stokes and anti-Stokes scattering.

The Brillouin Gain Spectrum (BGS) peaks at the Brillouin frequency shift (ν_B), and the peak value is given by the Brillouin gain coefficient g_0:

$$g_B(\nu_B) = g_0 = \frac{2\pi n^7 p_{12}^2}{c\lambda_p^2 \rho_0 V_A \Delta\nu_B} \tag{2.33}$$

where p_{12} is the longitudinal elasto-optic coefficient and ρ_0 is the material density [18].

In a standard single-mode optical fiber (SMF) with a given refractive index $n = 1.44$ and acoustic velocity $V_A = 5.9$ kms^{-1}, the typical value of the BFS (ν_B) is ~ 10.8 GHz, for an incident wavelength λ_p centered at ~1550 nm. The Brillouin linewidth ($\Delta\nu_B = \Gamma_B / 2\pi$) for these operating parameters is typically ~ 30 MHz.

2.4.1.1 Temperature and Strain Dependence of the Brillouin Scattering

As previously stated, the Brillouin Stokes and anti-Stokes spectra manifest shifted a certain frequency (ν_B) from the incident wave. The Brillouin frequency shift is dependent on the incident pump wavelength (λ_p), but also on the refractive index (n) and the acoustic velocity (V_A), as expressed in Eq. (2.31). If Eq. (2.31) is derived with respect to strain and temperature, it renders the following equations:

$$\frac{\partial \nu_B}{\partial T} = \frac{2}{\lambda_p}\left(V_A \frac{\partial n}{\partial T} + n\frac{\partial V_A}{\partial T}\right) = \nu_B C_T \tag{2.34}$$

$$\frac{\partial \nu_B}{\partial \varepsilon} = \frac{2}{\lambda_p}\left(V_A \frac{\partial n}{\partial \varepsilon} + n\frac{\partial V_A}{\partial \varepsilon}\right) = \nu_B C_\varepsilon \tag{2.35}$$

Where C_T and C_ε are the temperature and strain coefficients, respectively. These coefficients depend on the material itself, and may vary from one fiber to another, but typical values are around $\sim 505.5\ MHz/\%$ (or $\sim 0.05\ MHz/\mu\varepsilon$) for strain, and $\sim 1\ MHz/^{\circ}C$ for temperature for standard SMF fibers and pump waves at $\lambda_p = 1550$ nm [19].

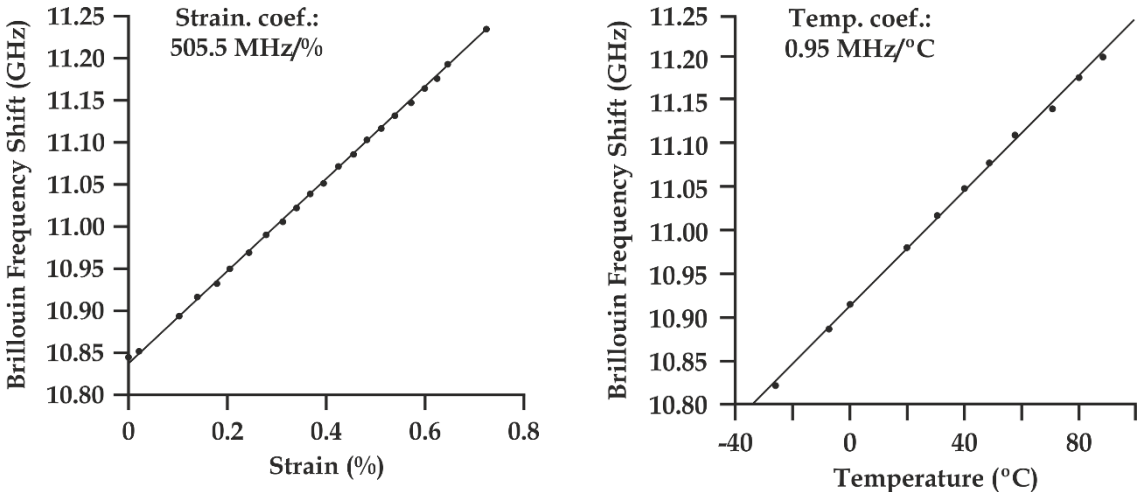

Figure 2.8: Brillouin frequency shift dependence on (a) strain, and (b) temperature for an incident pump wave at $\lambda_p = 1550$ *nm* [19].

The temperature and strain dependence of the BFS allows developing distributed sensors based on Brillouin scattering. However, it is not possible to isolate temperature or strain contributions to changes in the BFS. The most common solution to measure both magnitudes is to use two spatially close fibers: one of them is loose inside the cable as to isolate it from changes in the strain; the other one is fabricated in tight contact with the cable, so any deformation on it would be directly transferred to the fiber. This way, the tight fiber will be sensitive to both strain and temperature, meanwhile the loose fiber would be only sensitive to temperature. This latter fiber could be then used to compensate the temperature drifts on the strain measurements.

2.4.2 Stimulated Brillouin Scattering (SBS)

Although spontaneous Brillouin scattering was predicted in 1922, the stimulated process, which needs a powerful and coherent light source, was not observed until the 1960s, after the invention of the laser. In 1964, Chiao *et al.* [20] observed that if the incident light is powerful enough, the acoustic wave is reinforced by the pump light beam itself, so the scattering phenomenon can be considerably enhanced. Stimulated Brillouin Scattering (SBS) is quite similar to SRS inasmuch as it manifests through the generation of a Stokes and an anti-Stokes wave whose frequency is down or upshifted respectively from that of the incident light by an amount set by the medium. However, there are several differences between the two phenomena. In SBS, the scattered photons propagates only in the backward direction, meanwhile in SRS they can spread in both forward and backward directions. The Brillouin Frequency Shift (BFS) manifests typically at ~ 11 GHz (for λ_p at 1550 nm), which is three orders of magnitude smaller than the RFS (~13 THz). All of these differences are due to the nature of the light-matter interaction in each case (acoustic or optical phonons).

There are two mechanisms where SBS arises: either by utilizing a pump power higher than the so-called Brillouin threshold (see forthcoming Section 2.4.2.4); or by introducing a counter-propagating wave with a frequency equivalent to the Brillouin Stokes or anti-Stokes frequency (see Section 2.4.1 for further details), as to stimulate the scattering process. This

latter procedure is the one exploited in this thesis, and the counter-propagating wave will be called, from now on, the probe wave.

2.4.2.1 Electrostriction

The electrostriction is the predisposition of some materials, such as silica, to compress under the presence of an electric field. At the same time, the electrostriction is related to the phenomenon where molecules are liable to move or re-orientate under the presence of an electric field in order to maximize their potential energy [6]. If we consider the force acting over molecules ($\mathbf{F}$) is acting solely over a unique molecule (macroscopic point of view), under the presence of an electric field ($\mathbf{E}$) the molecule develops a dipole moment that increases its potential energy (Δu)[11], therefore:

$$\Delta u = \frac{1}{2}\Delta\varepsilon_{\text{var}}\left|\mathbf{E}\right|^2 \tag{2.36}$$

where $\Delta\varepsilon_{\text{var}}$ is the variation of the dielectric permittivity and $\left|\mathbf{E}\right|^2$ is proportional to the intensity of the electric field. Therefore, the force acting over the dipole is given by:

$$\mathbf{F} = -\nabla u = \frac{1}{2}\varepsilon_0\alpha_P\nabla(\mathbf{E}^2) \tag{2.37}$$

where ε_0 is the permittivity in free space and α_p is the molecular polarizability.

The $\mathbf{F}$ force produces an internal pressure known as electrostrictive pressure (p_{el}). When the media is compressible, the electrostrictive force produces a densification (Δp) with respect to the average medium density, as well as a molecular displacement [11]. Hence, the dielectric constant varies in the following way:

$$\Delta\varepsilon_{\text{var}} = \frac{\partial\varepsilon}{\partial p}\Delta p \tag{2.38}$$

where the work per unit developed by the force compressing the material is proportional to the electrostrictive pressure (p_{el}) as a function of the intensity of the electric field:

$$p_{el} = -\frac{1}{2}\rho_0 \frac{\partial \varepsilon}{\partial p}\left|\mathbf{E}\right|^2 = -\frac{1}{2}\varepsilon_0 \gamma_e \mathbf{E}^2 \tag{2.39}$$

being γ_e the electrostrictive constant that equals $\rho_0\left(\partial\varepsilon/\partial\rho\right)$.

By inserting the electrostrictive pressure (p_{el}) from Eq. (2.39) in Eq. (2.20), it provides coupled-wave field equations for the three waves present on the SBS interaction: pump, probe and acoustic wave, which lead to the coupled intensity equations represented in the forthcoming subsection 2.4.2.3.

2.4.2.2 Stimulated Brillouin Scattering through Electrostriction

The electrostriction becomes a key mechanism when aiming to generate SBS in optical fibers due to the great amount of acoustic phonons it can generate. The produced stimulation is enhanced with the beating between the pump wave and the corresponding counter-propagating signal. If the counter-propagating probe wave is properly tuned to ν_S (Brillouin Stokes frequency, in this case), so that the frequency difference with the pump wave (ν_p) matches the Brillouin frequency shift ($\nu_B = \nu_p - \nu_S$), it will enhance the SBS process. The pump and the probe will interfere with each other, creating an electrical intensity wave. Such electrical intensity wave is transformed into an equivalent pressure (acoustic) wave moving along the medium at the acoustic velocity (V_A), due to electrostriction. The moving pressure wave induces a periodic variation in the density of the material. This periodic density variation leads to a change in the refractive index, which can be seen as a creation of a Bragg grating moving along the fiber, whose resonant frequency is the one of the pump wave. When the pump encounters the moving diffraction grating along the fiber, light will be backscattered. The frequency of the backscattered light is downshifted with respect to the pump frequency, proportional to the Brillouin frequency shift of the material. Such downshifting occurs due to Doppler effect, since the moving grating co-propagates with the pump, propagating at the acoustic velocity V_A. The scattered photons feed the Stokes wave (probe), which means, the probe wave is amplified whenever it encounters the pump, enhancing the acoustic wave along

the fiber. This process is repeated cyclically since the Stokes wave and the acoustic wave reinforce mutually, becoming a self-sustained loop, as illustrated in Figure 2.9.

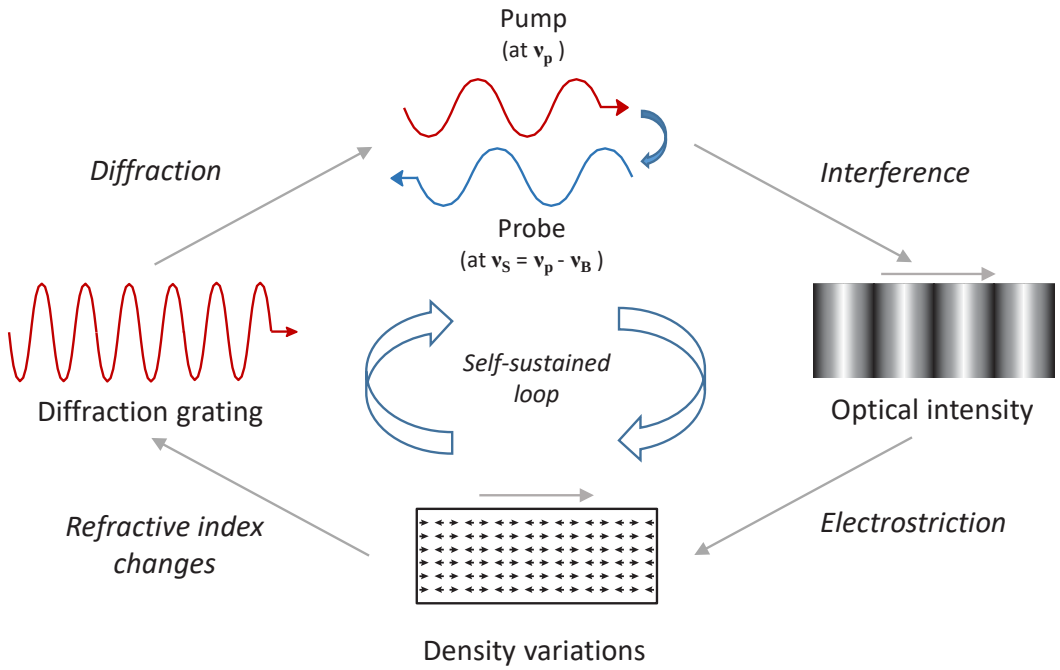

Figure 2.9: Illustration of the stimulated Brillouin scattering (SBS) process for a Stokes wave.

The spectral amplification suffered by the probe Stokes wave is commonly known as the Brillouin gain spectrum (BGS), as depicted in Section 2.4.1. It follows the typical Lorentzian shape introduced in Section 2.4.1:

$$g_B(\nu) = g_0 \frac{(\Delta\nu_B/2)^2}{(\nu-\nu_B)^2 + (\Delta\nu_B/2)^2} \tag{2.40}$$

where g_0 is the Brillouin gain coefficient defined in Eq. (2.33).

Analogously, if the probe wave is tuned to match the Brillouin anti-Stokes frequency ($\nu_{AS} = \nu_p + \nu_B$), a similar process would occur. The pump and the counter-propagating probe wave will interfere creating an optically-induced density fluctuation in the medium due to electrostriction. The density variation modulates the refractive index of the material, creating a moving diffraction grating, which period is proportional to the Brillouin shift of the medium.

Such diffraction grating, in this case, co-propagates with the anti-Stokes probe wave, moving at the given acoustic velocity (V_A). Thus, every time the probe wave meets the moving Bragg grating it will backscatter photons, which due to Doppler effect, will be downshifted in frequency. These photons feed, in this case, the pump wave, reinforcing once again the generation of the acoustic wave, and continuing the process. Hence, the anti-Stokes component is depleted, in this case, in order to amplify the pump wave. The SBS interaction between the pump and the Stokes or anti-Stokes probe waves respectively are depicted in Figure 2.10.

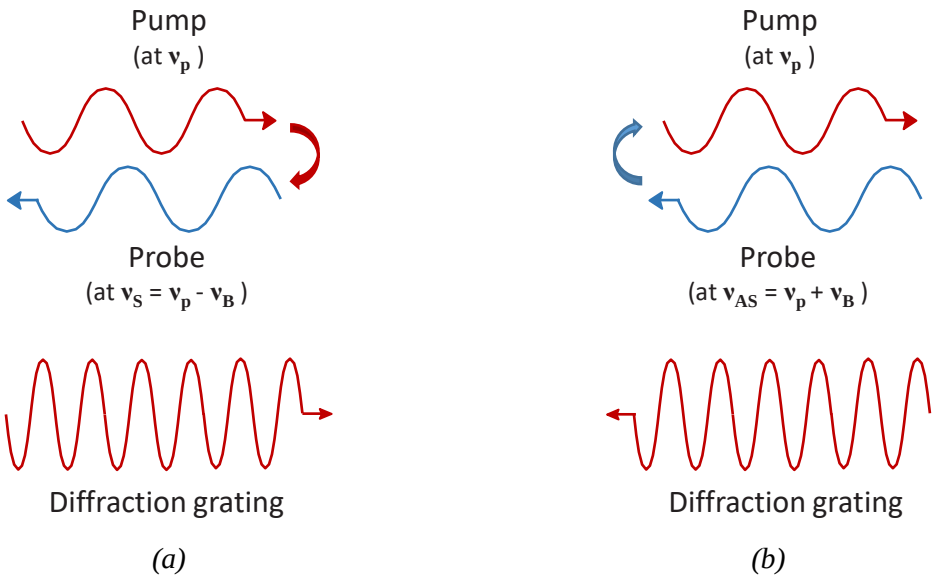

Figure 2.10: Illustration of the SBS interaction between the pump and (a) Stokes probe wave or (b) anti-Stokes probe wave; generation of the moving grating and energy transfer between signals.

The depletion of the anti-Stokes component, which feeds the pump wave, renders the so-called Brillouin Loss Spectrum (BLS). The BLS, analogously to the BGS also fits a Lorentzian profile, although with a negative sign:

$$g_B(\nu) = -g_0 \frac{(\Delta\nu_B / 2)^2}{(\nu + \nu_B)^2 + (\Delta\nu_B / 2)^2} \tag{2.41}$$

Several options can be considered in order to generate the probe wave as to fully exploit SBS, and a review of the best approach, according to the literature, is given in Chapter 3.

2.4.2.3 Coupled Intensity Equations for SBS

In the same way that has been done for the SRS (see Section 2.3.2.1), the condition of a CW or quasi-CW is assumed, in order to give a proper explanation to SBS [12]. In addition, despite the previous description of the SBS phenomenon (given for either a Stokes or anti-Stokes probe wave), to clarify explanations only the Stokes case is considered in the following derivations. First, it is necessary to consider the counter-propagating nature of the Stokes wave with respect to the pump (as explained in Section 2.4.1). Second, since relatively small Brillouin shifts are assumed ($\omega \equiv \omega_p \approx \omega_S$), as well as equal fiber losses for both pump and Stokes waves ($\alpha \equiv \alpha_p \approx \alpha_S$), the following expressions can be obtained [12]:

$$\frac{dI_p}{dz} = -g_B(\nu) I_p I_S - \alpha I_p \tag{2.42}$$

$$\frac{dI_S}{dz} = -g_B(\nu) I_p I_S + \alpha I_S \tag{2.43}$$

The produced interference will depend on the relative polarization alignment among the interacting waves, I_p and I_S. On one hand, if no alignment is present, no interference will be produced and, on the other hand, with total alignment, maximum interference will arise. Therefore, with polarization diversity schemes, as will be described in forthcoming sections, the Brillouin gain ($g_{B(\nu)}$) will be reduced by a factor of 1.5 compared to the case where perfect alignment along the entire fiber is guaranteed [21].

2.4.2.4 Brillouin Threshold

In this case, again, as it was done in Section 2.3.2.3, to estimate the Brillouin threshold, pump depletion can be neglected, which derives into an exponential decay of the pump wave, given by:

$$I_p(z) = I_p(0)\exp(-\alpha z) \tag{2.44}$$

In this case, if Eq. (2.44) is substituted in Eq. (2.42) and integrating the latter over the fiber length (L), it provides the Stokes intensity, which grows exponentially in the backward direction, as follows:

$$I_S(0) = I_S(L)\exp(g_B(\nu)I_p(0)L_{eff} - \alpha L) \tag{2.45}$$

where L_{eff} is the effective length (see Section 2.2 for further details). It is important to mention that when a pulsed signal is used as a pump wave, L_{eff} is dependent on the pulse width:

$$L_{eff} = \frac{v_g T_0}{2} \tag{2.46}$$

where v_g is the group velocity and T_0 the pulse width.

Thus, as Eq. (2.45) depicts, the Brillouin Stokes wave grows exponentially when travelling through the fiber counter-propagating to the pump wave, due to Brillouin amplification occurring as a result of SBS. Since the spontaneous Brillouin bandwidth is very narrow ($\Delta\nu_B < 100$ MHz), the Brillouin threshold, also known as SBS threshold (P_{th}^{SBS}), strongly depends on the pump light linewidth ($\Delta\nu_p$). The SBS threshold, i.e., the power at which the backscattered signal power at the input of the fiber equals the pump power at the output of it, is given by the following expression [13], [22], which accounts for CW light with $\Delta\nu_p > \Delta\nu_B$:

$$P_{th}^{SBS} \approx 21\frac{A_{eff}}{g_B L_{eff}}\frac{\Delta\nu_p \otimes \Delta\nu_B}{\Delta\nu_B} \tag{2.47}$$

where the $\otimes$ denotes the convolution between the pump linewidth and the Brillouin bandwidth. For Lorentzian profiles, it turns out that $\Delta\nu_p \otimes \Delta\nu_B = \Delta\nu_p + \Delta\nu_B$. Thus, if a coherent pump light source is used, so that $\Delta\nu_p \ll \Delta\nu_B$, Eq. (2.47) can be simplified as follows:

$$P_{th}^{SBS} \approx 21\frac{A_{eff}}{g_B L_{eff}} \tag{2.48}$$

If typical optical communication parameters are used for SMF fibers operating at $\lambda_p = 1550$ nm ($A_{eff} = 80\mu\,\mathrm{m}^2$, $L_{eff} \approx$ 20 km and $g_B = 1.5\times10^{-11}$ m/W) [12], the Brillouin threshold will be ~ 5.6 mW. Thus, SBS turns out to be dominant over SRS, which manifests at ~ 970 mW.

Chapter 3:
Brillouin Optical Time Domain Analysis

3.1. Introduction

Brillouin scattering has been traditionally identified as a major limitation in optical communication systems, especially when augmenting the intensity of the signals in the fiber. Since the early 1990s, though, it has also played an important role in the development of optical fiber sensors. Particularly, Brillouin Optical Time Domain Analysis, commonly known by its acronym, BOTDA, is a sensing technique that provides position-resolved information of the SBS interaction along the fiber length using time-domain analysis. It was first described by Horiguchi *et al.* in 1989, as a fiber inspection procedure alternative to the widely known OTDR (Optical Time Domain Reflectometry), based on Rayleigh scattering. It has become, since then, one of the trendiest approaches when monitoring large infrastructures, such as oil & gas pipelines, railways, wind farms, etc.

Throughout this thesis, the limitations of the BOTDA technique are extensively analyzed, implementing feasible solutions to overcome several of such limitations, as well as improving the overall performance of the sensors.

3.2. BOTDA Working Principle

BOTDA allows performing distributed measurements of strain and/or temperature along several tens of kilometers of fiber. Its working principle is based on the interaction of two counter-propagating light beams: a pulsed pump light, and a continuous wave (probe). The probe signal is amplified/depleted by the pump due to SBS whenever their frequency difference matches the Brillouin shift (ν_B) of the fiber (see Section 2.4.2). Figure 3.1 shows a simple scheme representing the original BOTDA proposed by Horiguchi *et al.* [23]. On it, the pump pulse goes through the fiber in the $+z$ direction, and the probe (CW) advances inside the fiber in the $-z$ direction (counter-propagating to the pump pulse).

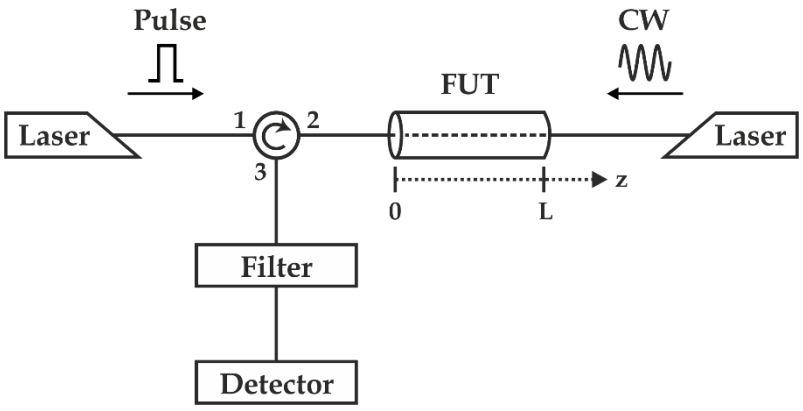

Figure 3.1: Original BOTDA scheme proposed by Horiguchi et al. [23]. *FUT: Fiber Under Test; CW: Continuous Wave* [6].

As previously explained in Section 2.4.2, Brillouin scattering manifests as a Lorentzian profile several megahertz wide ($\Delta\nu_B$) [12][11], whose peak (ν_B) may shift along the fiber length due to fabrication non-homogeneities or local fiber conditions. Hence, to perform proper BOTDA measurements, i.e., obtaining full Brillouin profiles of the fiber, it turns necessary to sweep the pump-probe frequency offset. The original BOTDA proposal, as Figure 3.1 illustrates, featured two separate laser sources. Thus, as the Brillouin shift depends on the pump wavelength [see Eq. (2.30)], any drift in one of the laser sources also entails an equivalent error on the BFS determination. One of the greatest advances of the BOTDA techniques was made

by Niklès *et al.* [24], where they proposed the use of a single laser source to shape both the pump and probe signals, avoiding any relative error due to laser drifts.

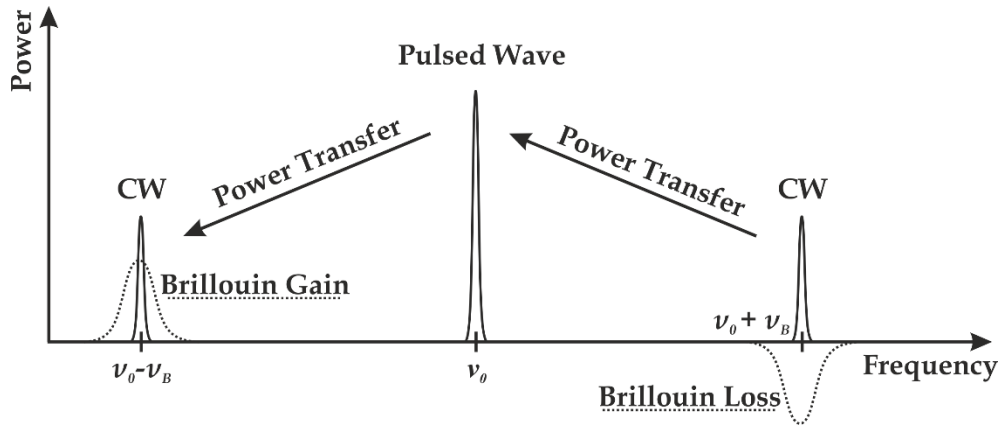

Figure 3.2: BOTDA working principle where a dual-tone probe (DSB modulated CW) is located around the Brillouin Gain/Loss frequencies for a pump pulse at ν_0*. The higher frequency probe component, located at* $\nu_0 + \nu_B$ *(Brillouin loss), transfers energy to the pump, meanwhile the pump (*ν_0*) transfers an equivalent amount of energy to the lower frequency component, located at* $\nu_0 - \nu_B$ *(Brillouin gain)* [6].

Since there is a gain process (Brillouin Gain) occurring at lower frequencies than the pump frequency ($\nu_0 - \nu_B$), and an equivalent attenuation (Brillouin Loss) happening at higher frequencies ($\nu_0 + \nu_B$), the probe wave can be chosen to match either Brillouin Gain or Loss frequencies. In the original work presented by Horiguchi *et al.* [23], both cases are illustrated. Such approach, where a single probe tone is used, became widely spread because of its simplicity, but yields a less robust system, where some undesired phenomena start arising when utilizing strong powers [25], as we will see later in this chapter. A common and well-established solution is to use a dual-tone probe, where the probe is tuned to match at the same time Brillouin Loss and Brillouin Gain [26]. The usual working principle is based on the use of a single laser source (Niklès *et al.* [24]), where the probe wave is intensity-modulated using a Dual Side-Band (DSB) modulation. This way, as shown in Figure 3.2, there is a balanced energy transfer between pump and probe, i.e., the amount of energy withdrawn from the pump by the lower-frequency probe component is at the same time provided to the pump by the higher-frequency probe sideband. This is the approach used throughout this thesis.

Another fundamental parameter of the sensors is the spatial resolution of the system. It is defined as the smallest fiber section over which any sensible variation can be detected [6]. In BOTDA, it is directly proportional to the width of the pump pulses, as expressed in the following equation:

$$\Delta z = \frac{1}{2}\frac{c}{n}T_0 \simeq T_0 \cdot 10^8 \tag{3.1}$$

where T_0 is the pulse width in seconds, $c = 3 \cdot 10^8$ m/s is the speed of light in vacuum and the refractive index of a standard Single Mode Fiber (SMF) is considered $n \simeq 1.45$. Therefore, the spatial resolution of the system follows the relationship of ~ 1 meter per every 10 ns.

Now that all the necessary elements of BOTDA have been introduced, it is time to analyze how a BOTDA system operates. Figure 3.3 illustrates the basic BOTDA working principle, where a pump pulse is introduced into the fiber at $z = 0$, and where the probe (CW) is inserted into the opposite side, at $z = L$, i.e. counter-propagating to the pump pulse. The probe wave is modulated to match Brillouin gain or loss (SSB modulation) or both of them (DSB modulation). Figure 3.3 depicts the functioning of a BOTDA operating in gain configuration (SSB-modulated probe wave, matching the Brillouin gain region). Whenever the probe wave (located at a certain frequency ν_{probe}) encounters the counter-propagating pump pulse, it gets amplified only if their frequency difference matches the local Brillouin frequency shift of the fiber (ν_B), as shown in Figure 3.3(a). The local amplification the pump wave renders on the probe signal due to SBS is given by the following expression:

$$\Delta P_S(z) = \frac{g_B}{A_{eff}} P_P(z) P_S(z) \Delta z \tag{3.2}$$

where ΔP_S is the local power transfer to the probe Stokes wave, g_B is the Brillouin gain coefficient, A_{eff} is the nonlinear effective area, P_P and P_S are the pump and probe (Stokes band) powers respectively, and Δz is the spatial resolution [see Eq. (3.1)].

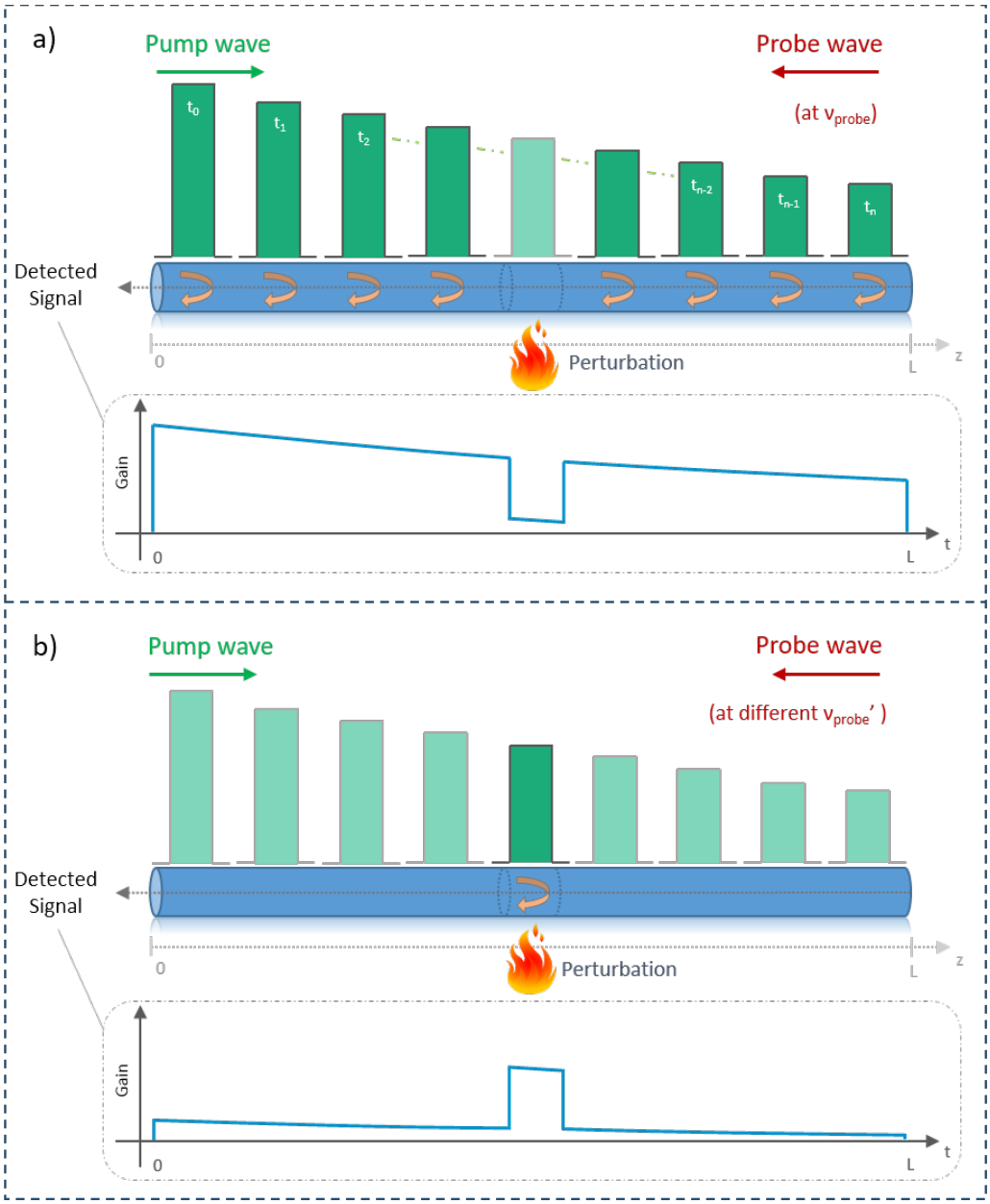

Figure 3.3: BOTDA working principle: SBS interaction between the pulsed pump wave and a) a probe wave tuned to match the overall BFS of the fiber, where a certain region experiences a local perturbation (change in temperature or strain); b) a probe wave tuned to match the local BFS of the perturbed section. Both cases are illustrated with their time-domain retrieved signal.

Since, obviously, the pump pulse loses power due to the fiber attenuation, the amplification experienced by the probe wave increases towards $z = 0$. If any anomaly (i.e. any local variation in the fiber temperature or strain) occurs in the fiber, the local BFS of the fiber will vary, and since the pump-probe frequency offset does not match the current probe

modulation frequency, the probe will not be amplified in such local region. Conversely, as depicted in Figure 3.3(b), if the probe wave is tuned to match the local BFS of the non-homogeneous section (ν_{probe}'), it will be amplified only in that local section of the fiber, experiencing no amplification in the rest of the link.

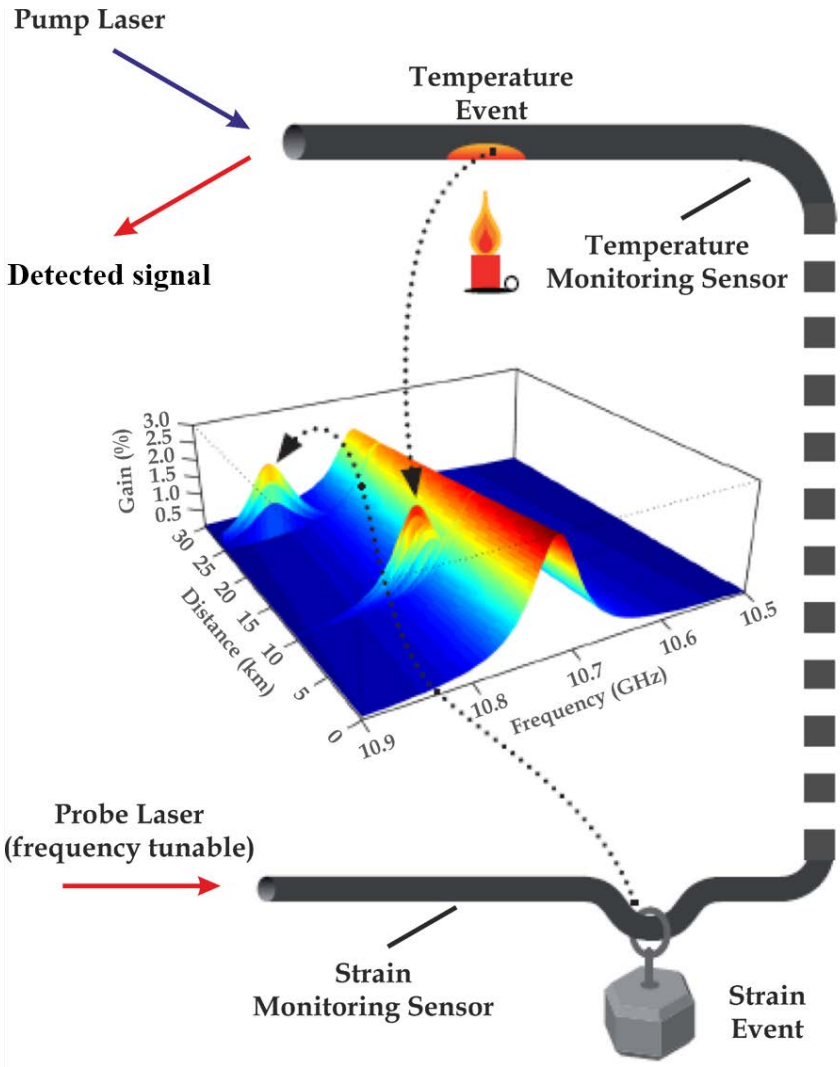

Figure 3.4: Brillouin profile of a 30 km SMF, retrieved by a BOTDA system in the presence of two perturbations in the fiber: a temperature increase and a positive strain [6].

By analyzing the time-of-flight of the pump pulses, the time-to-distance conversion is straightforward, which enables a precise determination of the events occurring in the fiber, in a distance-wise manner. Finally, after experiencing SBS along the fiber, such time-domain

signal arriving at the detector is mostly a background DC level, where the signal of interest (amplified probe due to SBS) represents a tiny variation on top of it (typically < 5 %).

By retrieving consecutive time traces for different pump-probe frequency offsets (ν_{probe}), a full 3D profile of the fiber can be developed, such as the one illustrated in Figure 3.4. Any event occurring to the fiber, i.e. any deformation or temperature change, will be directly imprinted on the BFS profile (see Figure 3.4). Such BFS variations, as previously stated, cannot be univocally distinguished if affecting the same fiber region at unison, since both the temperature and strain events contribute to the BFS.

3.2.1 Theoretical Model

The coupled-wave equations derived in subsection 2.4.2.3 can be applied to a BOTDA in order to describe the power evolution of the pulsed and CW signals (I_p and I_{CW} respectively)[12], [27]:

$$\frac{dI_p}{dz} = -g_B(\nu) I_p I_{CW} - \alpha I_p \tag{3.3}$$

$$\frac{dI_{CW}}{dz} = -g_B(\nu) I_p I_{CW} + \alpha I_{CW} \tag{3.4}$$

where $g_B(\nu)$ is the BGS [see Eq. (2.32)] and α is the fiber attenuation. In the case of the BGS at a specific fiber position, it is worth mentioning that it will depend on the polarization states of the light beams traveling within the fiber [21], [27], [28]:

$$g_B(z,\nu) = \gamma_f g_0 \frac{(\Delta\nu_B/2)^2}{(\nu-\nu_B)^2 + (\Delta\nu_B/2)^2} \tag{3.5}$$

where γ_f is the polarization factor [29].

Although Equations (3.3) and (3.4) are applicable for steady-state conditions, they can be applied to the BOTDA model despite one of the signals is pulsed, since it can be considered that the pulse width is generally much longer than two times the phonon lifetime ($\sim$ 6 ns) [6], [30]. In any other case, the full dynamic model of SBS should be taken into account.

As stated previously, a BOTDA can work either in Gain or Loss configuration. The first case arises when the pulsed signal transfers its power to the CW, setting a positive value for $g_B(\nu)$. On the other case, the power is transferred from the CW to the pulsed beam, where $g_B(\nu)$ will have a negative sign. If we consider the Brillouin Gain case ($g_B(\nu) > 0$), which is a widely employed approach in long range BOTDA systems, a perturbation method can be employed to solve the system of Eq. (3.3) and Eq. (3.4) so the Brillouin gain received from a particular spatial location can be retrieved considering that only the fiber attenuation (α) affects the CW probe [29]:

$$I_{CW}(z) = I_{CW}(L)\exp[-\alpha(L-z)] \tag{3.6}$$

where $I_{CW}(L)$ is the input power of the CW probe and L is the sensing length. If Eq. (3.6) is substituted in Eq. (3.3) the pulsed wave has the following analytic solution:

$$I_p(z) = I_p(0)\exp(-\alpha z)G(z,\nu) \tag{3.7}$$

where $I_p(0)$ is the input peak power of the pulsed laser and $G(z,\nu)$ represents the depletion experienced by the pulsed beam due to Brillouin interaction, and comes represented by [28]:

$$G(z,\nu) = \exp\left(-\int_0^z g_B(z',\nu)I_{CW}(L)\exp[-\alpha(L-z')]dz'\right) \tag{3.8}$$

If Eq. (3.7) is substituted in Eq. (3.4), it can be integrated over Δz_i distance, interval in which the pulsed beam interacts with the CW [6], [28], [29]:

$$\int_{I_{CW}(z)}^{I_{CW}(z+\Delta z_i)} \frac{dI_{CW}(z,\nu)}{I_{CW}(z,\nu)} = \int_z^{z+\Delta z_i} \left[-g_B(z',\nu)I_P(z',\nu)+\alpha\right]dz' \tag{3.9}$$

To recover the information of the BGS along the fiber, it is necessary to compare the CW light intensity with and without Brillouin interaction. This intensity change can be expressed as a function of time (t) and frequency offset (ν) considering that the gain factor (G) nearly equals 1 so the changes in the pulse intensity are mainly due to fiber attenuation (α) [31]:

$$\Delta I_{CW}(t,\nu) \propto \int_{tv_g/2}^{tv_g/2+\Delta z_i} g_B(z',\nu)Ip(z',\nu)dz' \tag{3.10}$$

where $0 < t < 2(L - \Delta z_i)/v_g$. This expression allows to directly reconstruct the BGS from measurements of the CW intensity, which presents the same Lorentzian shape as the Brillouin gain coefficient ($g_B(\nu)$). Therefore, a full BGS/BLS profile as a function of distance can be retrieved by measuring the intensity contrast of the CW for different frequency offsets (ν), as it has been presented in Eq. (3.2).

Once we have gained a comprehensive insight of the BOTDA working principle, it becomes necessary to evaluate the performance of the sensors. The quality of such BOTDA measurements is driven by several parameters: the frequency step taken to sweep the pump-probe frequency offset, the number of averages in each time trace, the Brillouin bandwidth ($\Delta\nu_B$), the link length or the pulse width. All these parameters have an impact on the signal-to-noise ratio of the measurements, and ultimately the frequency uncertainty in the determination of the BFS. The contribution of these parameters in the frequency uncertainty of the sensor has been thoroughly studied by Soto *et al.* in [32]. In this paper, the particular contribution of each factor is analyzed, and a unitless figure-of-merit (FoM) is established, which aims to serve as an impartial method to evaluate the performance of BOTDA sensors. Such FoM is expressed as follows:

$$FoM = \frac{(\alpha L_{eff})^2 exp[(2+f_1)\alpha L]}{\Delta z\sqrt{N_{Tr}N_{AV}}}\frac{\sqrt{\delta\Delta\nu_B}}{\sigma_\nu} \tag{3.11}$$

where L is the sensing fiber length, Δz is the spatial resolution, δ is the frequency step of the sweep and σ_ν is the frequency uncertainty in the determination of the BFS. N_{AV} corresponds to the required number of averages in the temporal traces and N_{Tr} accounts for the number of acquired traces (equals 1 in conventional BOTDA and 2 in differential-pulse schemes). f_1 is a parameter that takes into account the fiber configuration: f_1 = 0 for the standard fiber configuration (i.e. when the total fiber length is equal to L) and f_1 = 1 for the fiber loop configuration [12,30], in which half of the total fiber length is employed for sensing (i.e. when the total fiber length is equal to 2 L). In this thesis, the implemented schemes sense along the entire fiber span, thus, being f_1 equal to zero for the presented results.

The FoM turns out to be 1 for a typical commercial BOTDA sensor of distance range L = 30 km, spatial resolution of Δz = 1 m and error on the Brillouin frequency of σ_ν = 1 MHz,

obtained with a standard BOTDA method (i.e. f_1 = 1 and N_{Tr} = 1), N_{AV} = 1024 temporal trace averaging and with frequency sampling step δ = 1 MHz, in a standard fiber with $\Delta\nu_B = 27$ MHz and 0.2 dB/km of attenuation [32]. The limitations of the parameters that drive the performance of BOTDA sensors (SNR) as well as the current state-of-the-art is studied in the forthcoming subsections.

3.3. Limitations of the Technique

Since the first implementations of the BOTDA sensing technique in the early 90s, the performance of the sensors has improved considerably, extending the sensing range, the spatial resolution of the system and reducing the uncertainty of the measurements. As previously mentioned, in BOTDA, the signal of interest, which carries the meaningful information about the fiber, represents a small percentage compared to the total background signal (typically not higher than 5 %). Hence, the most limiting factor is the signal-to-noise ratio of the system, where all the sensor parameters are directly linked to it. A probably straightforward strategy to improve the system characteristics could be to increase the intensity of the signals present in the fiber as to enhance the SBS interaction among them, and thus, boost the sensing performance. However, as we will study in this section, there are several trade-offs worth considering when pushing the system performance, where some very specific limits have been pointed out in the literature.

3.3.1 Power Limitations

The use of the BOTDA technique as an approach to sense temperature/strain variations along the optical fiber in a distributed manner was first described by Kurashima *et al.* [33] in 1990. In this first implementation, the authors measured 1.2 km of fiber, featuring 100 m of spatial resolution and achieving a temperature accuracy of 3°C. Since then, the technique has become a great field of research for in both the academia and the industry, experiencing a tremendous evolution. One of the greatest advances was suggested by Niklès *et al.*

in 1996 [24], in which they overcome the problematic of suffering laser drifts (originating from the use of two different laser sources) by shaping both the pump and the probe from a unique and common master laser. Using such approach, the authors successfully achieved a total range of 1.4 km of SMF, though reducing the spatial resolution down to 35 m. Ever since, the sensing range of BOTDA systems has considerably increased, while increasing the number of resolved points in the fiber. Nowadays, a standard BOTDA sensor typically performs over a range of 30-50 km with a spatial resolution of ~2-5 m, featuring ~1 MHz of frequency uncertainty for an acquisition time of a few minutes. Boosting the power of the signals present in the fiber might improve the overall performance (i.e. SNR) in BOTDA systems (increase in sensing range and number of resolved points, reducing uncertainty and acquisition time) up to a certain limit, where some spurious effects start arising. As a matter of fact, one of the first implementation constraints on the probe wave is the onset of Amplified Spontaneous Brillouin Scattering (ASpBS), which is ~5 mW (~7 dBm), as derived in subsection 2.4.2.4. In the literature, this threshold comes denominated as SBS or ASpBS threshold. In this thesis, the latter option will be the preferred choice to identify the limit at which the measured traces start showing distortions. Other power-limiting phenomena, constraining the pump power are also studied hereafter.

3.3.1.1 Modulation Instability

The phenomenon known as Modulation Instability (MI) manifests as the appearance of two side lobes in the spectrum of a continuous pump wave. In the time domain it can be seen as the breakup of CW pump radiation into a train of ultrashort pulses. It is directly related to the used pump power and the dispersion of the optical fiber the signal is going through [34]. MI has proven to be a limiting effect in the performance of distributed fiber sensors based on stimulated Brillouin scattering and/or coherent Rayleigh reflectometry, due to the long distances of the fiber spans commonly used. The detrimental effect of MI in distributed fiber sensors has been analyzed by Foaleng [35] and Alasia [36] in their respective thesis dissertations, though in the latter case, the effect was reproduced by seeding two sidebands on the pump spectrum and observing their evolution with the input power. In our particular case,

as the pump and probe signals travel always in opposite directions, as explained in Figure 3.1, the generated sidebands due to MI are only seeded from noise. This process induces a recurrent signal depletion.

For high power levels, the pump signal gets depleted in favor of the generated noise sidebands. When either the range or the pump power are increased, the power transfer is reversed after a certain distance, which is translated as a power return from the sidebands to the central pump wave. This reversible behavior of the MI is known as the Fermi-Pasta-Ulan (FPU) recurrence [37]. After some more distance, the phenomenon again transfers power from the pump to the sidebands, resulting into an oscillatory power pattern in the pump pulse. Figure 3.5 shows a simulation of such particular behavior of MI for a 10 km SMF, processed by Martins [2] in his thesis dissertation, which has been obtained from the integration of the Non-Linear Schrödinger Equation (NLSE) using noise as seed.

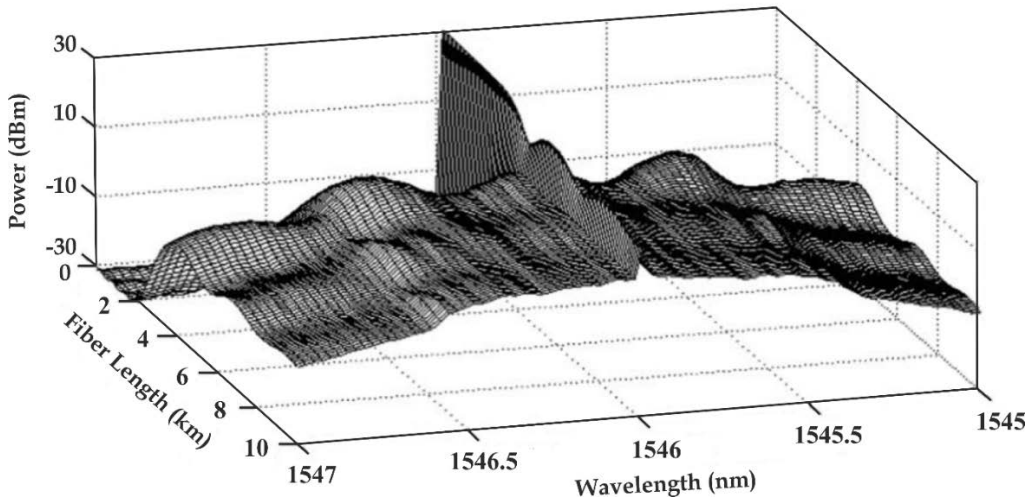

Figure 3.5: Spectral simulation of the effect of MI on a pump pulse over 10 km of SMF [2].

The critical power limit to avoid MI in BOTDA, as well as a detailed model of MI in fiber optics, has been thoroughly studied by Alem *et al.* [38]. Figure 3.6 shows an analysis of the evolution of the pump power in a 25 km-long SMF for several input pump powers, where a clear safe scenario is ensured if the input power does not exceed 100 mW.

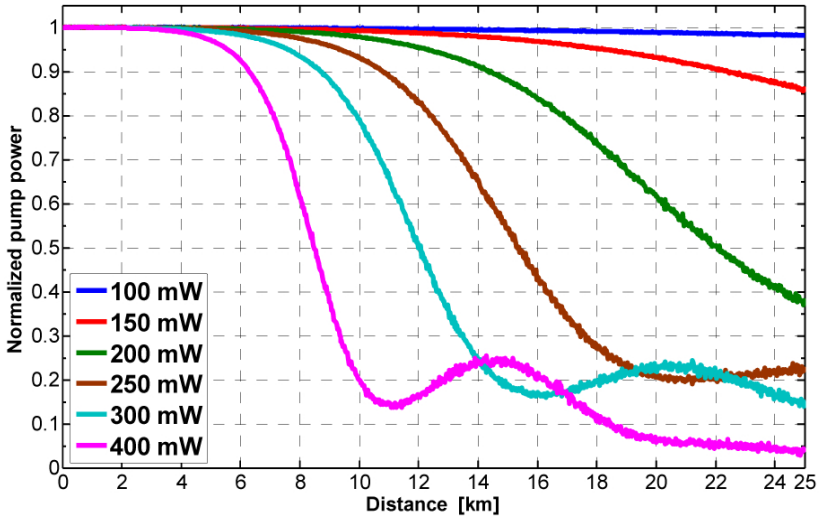

Figure 3.6: Pump power evolution along a 25 km SMF for different input pump powers [38].

Particularly in BOTDA, such detrimental effect on the pump power evolution directly induces a fading of the BOTDA trace, as shown in Figure 3.7. In this figure, it is proven that after a certain safe-limit, the gain of the BOTDA traces is increasingly reduced towards the end of the fiber meanwhile the pump power is raised.

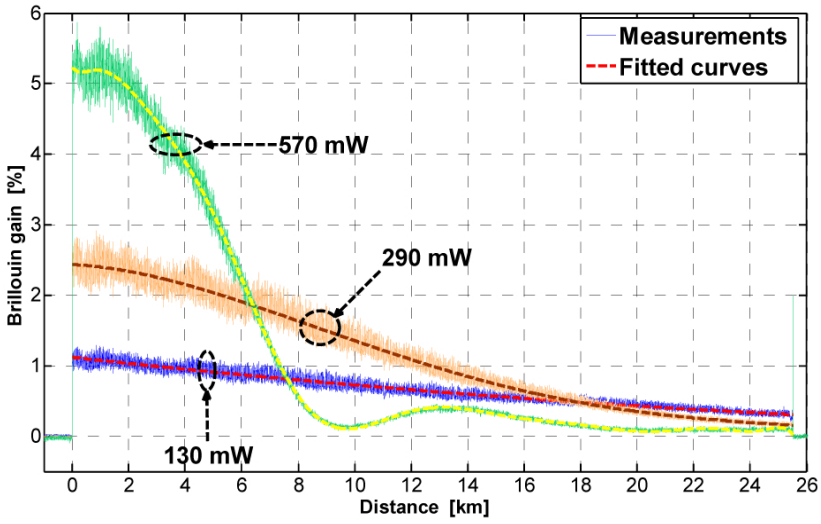

Figure 3.7: Experimental (continuous lines) and simulated (dashed lines) BOTDA traces for several input pump powers: 130 mW, 290 mW, and 570 mW [38].

3.3.1.2 Pump Depletion

Pump depletion refers to the frequency-dependent loss the pump suffers due to the pump-probe energy transfer (see Figure 3.2) [6]. This detrimental effect has been widely studied in the literature [2][39], where some smart approaches have successfully been used to avoid it [26][40]. However, it is the work of Thévenaz *et al.* [25] the one that provides a more detailed study of such phenomenon.

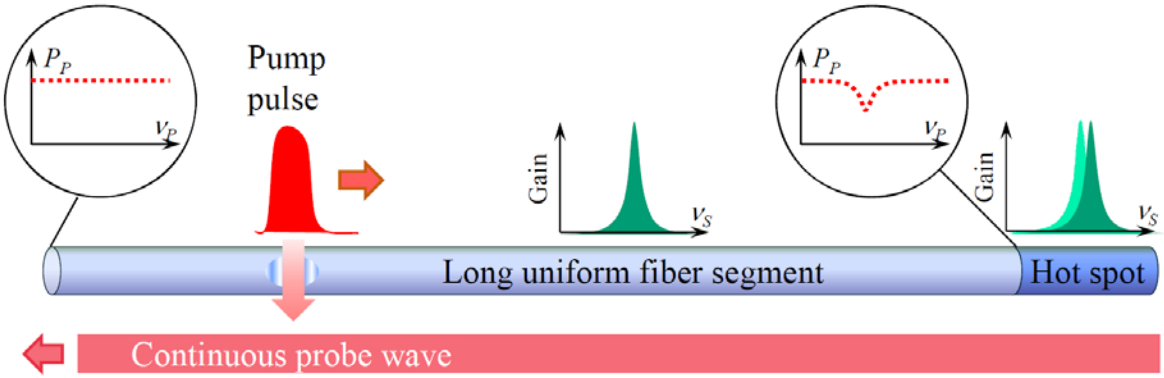

Figure 3.8: Worst case scenario for pump depletion: the pump pulse gradually transfers a fraction of its power to the CW through SBS. Since the BFS is uniform along most of the fiber, starting at the near end of it, the energy is constantly drained from the same spectral region of the pump wave. Hence, if any inhomogeneity takes place at the far end of the fiber, i.e. changing the local BFS, the CW will interact through SBS with an spectrally non-uniform pump pulse, thus, distorting the BGS (or BLS) retrieved at that region [25].

Depletion can be understood as a gradual power transfer from the higher frequency wave to the lower frequency one along the distance, leading to a frequency-dependent power variation in the pump pulses. If a BOTDA system in gain configuration is considered, as illustrated in Figure 3.8 (the pump is the pulsed wave and the CW is the amplified probe), the amplitude of the pump pulse will depend on the pump-probe frequency difference in presence of a cumulated energy transfer between the interacting waves [25]. As the pump pulse interacts continuously with the CW signal, this effect will be higher on the pump than on the CW since the latter only interacts with the pump during the pulse duration [6]. Furthermore, the severity of this effect on the pump wave will increase towards the end of the fiber (for the energy

transfer is cumulative along the distance), where additionally the probe power is at its highest (the stronger the probe wave, the more rapid is the power drained from the pump wave).

In practice, the described dynamic is translated as an uncontrolled amplitude change of the pump pulse, which at the same time does not certify a constant pulse power when the pump-probe frequency difference is scanned. In conclusion, the measured BGS/BLS will be distorted, especially if the central Brillouin gain/loss frequency is shifted with respect to the gain/loss spectrum in the preceding fiber section, e.g. due to a temperature difference or fiber elongation.

Following the notation of Thévenaz *et al.* [25], the quantity of the suffered depletion (d) for a BOTDA in gain configuration can be expressed as follows:

$$d = \frac{P_{p_0} - P_p}{P_{p_0}} \tag{3.12}$$

where P_{p_0} is the pump power when no Brillouin interaction arises and P_p is the pump power under maximum Brillouin interaction. In the case of the Brillouin loss BOTDA, d will just require a negative sign.

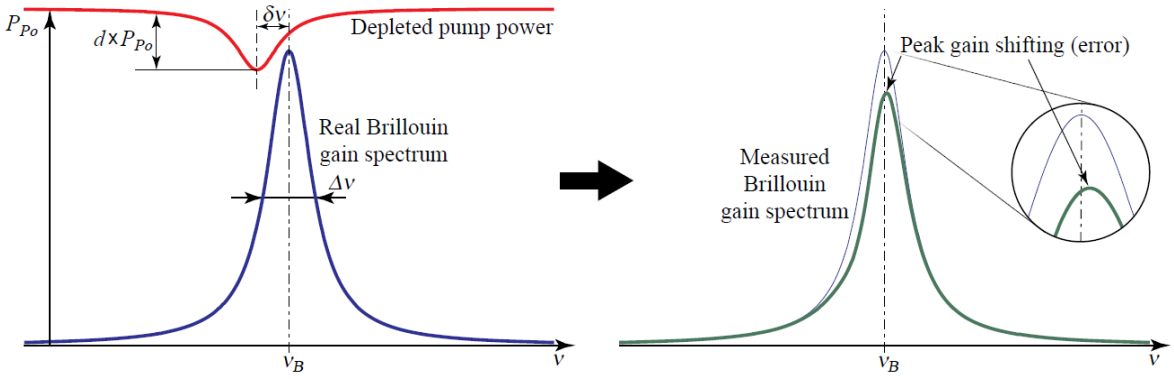

Figure 3.9: Effect of a spectrally non-uniform pump (highly depleted pump) interacting with the CW probe wave at a non-homogeneous fiber section, where the measured BGS is shifted [25].

As it can be seen in Figure 3.9, when a depleted pump wave is employed to scan the frequency difference ($\delta\nu$) of an inhomogeneous section of fiber, the measured gain frequency difference will have an error (ν_e) with respect to the actual BGS. In particular, it will be shifted

upwards or downwards depending on the relative position of the strain/temperature event with respect to the dominant fiber BFS.

The acceptable depletion coefficient ($d_{\max}$) for a given tolerable systematic error (ν_e) of the measured Brillouin gain frequency can be formulated through the following expression provided that $\nu_e \ll \Delta\nu_B$ [25]:

$$d_{max} = \frac{(1+4\xi^2)[16\xi e^2 - (1+4\xi^2)e]}{12\xi e^2 - 2(1+2\xi^2)e + \xi} \tag{3.13}$$

where $\xi = \delta\nu / \Delta\nu_B$ and $e = \nu_e / \Delta\nu_B$.

Considering the case of having two probe wave sidebands simultaneously within the fiber (DSB modulated probe), the depletion factor d will be defined as follows [25]:

$$1 - d = \exp\left(\frac{g_B}{A_{eff}} (P_{iS} - P_{iAS}) L_{eff} \right) \tag{3.14}$$

where P_{iS} and P_{iAS} are the two probe waves at the gain and loss frequencies at $z = L$ position, g_B is the Brillouin gain and A_{eff} and L_{eff} are the effective area and length respectively.

By reversing Eq. (3.13), the following expression is derived:

$$P_{iS} - P_{iAS} < -\ln(1-d)\frac{A_{eff}}{g_B L_{eff}} \overset{L\to 1}{=} -\ln(1-d)\frac{A_{eff}}{g_B}\alpha \tag{3.15}$$

where α is the fiber attenuation.

From Eq. (3.15) it can be inferred that, as Minardo *et al.* [26] and Cui *et al.* [40] suggested, in a DSB-Brillouin sensor, if the two probe sidebands present equal amplitude ($P_{iS} - P_{iAS} = 0$) the system becomes completely robust to pump depletion. In other words, when using such DSB modulation on Brillouin sensors, the depletion does not depend on the probe wave power, and the ultimate probe power limit is given by the onset of ASpBS. If a long-range system is considered, i.e. fiber distances longer than the non-linear effective length ($1/\alpha \approx 21$ km), the probe power limit is ~ 5 mW (~7 dBm) per sideband [25]. When making use of a SSB-probe scheme, though, the limit for a tolerable pump depletion framework is lower, ~ 40μW

(-14 dBm) per sideband [25]. However, even in a dual-probe BOTDA scenario, as it will be later described and demonstrated in this thesis, there are indeed a sort of depletion-like non-local effects arising for probe wave powers way below the ASpBS threshold, which dramatically harm the Brillouin measurements.

3.3.2 Spatial Resolution & Number of Resolved Points

The spatial resolution of a BOTDA sensor, as already stated, is directly linked to the pump pulse width, following Eq. (3.1). Reducing its duration improves the system resolution, although at the expense of lowering the SBS gain, due to the shorter interaction length and, consequently the available SNR. In addition, since the pump pulse amplifies the probe through SBS only after their interaction has excited the acoustic field, and since it takes time (~30 ns) for the acoustic field to fully build up, pulses shorter than ~30 ns significantly broaden the BGS/BLS. Such broadening reduces the peak of the Lorentzian profile, thus, reducing the SNR of the measurements and increasing the uncertainty. The ultimate pulse width lower limit is given by twice the phonon lifetime (~10 ns) (see Section 2.4.1), which sets the system minimum feasible resolution to be ~1 m. Below that, the acoustic wave does not get properly excited as to generate SBS, and therefore the BOTDA sensors cannot operate under such conditions.

Several approaches have been proposed in the literature to overcome such limitation, based on frequency, correlation [41]–[44] or time domain approaches [30], [45]. All of these techniques also pursue increasing the number of resolved sensing points in the fiber. Frequency- and correlation-domain approaches allow very sharp spatial resolutions (in the order of mm or a few cm), however the measurement range is typically limited to a few km. Using correlation-based schemes, a significant increase in the number of resolved points has been demonstrated along fibers of several km-long [41]–[44]; however, the total measurement time still remains extremely long, e.g. a few hours for 1 million points [42]. A most recent improvement has ultimately led to a remarkable state-of-the-art record, doubling the number of resolved points up to 2.1 million, in spite of an 8-fold increase in the acquisition time [44].

Conversely, time-domain approaches, which are typically much faster, are all based in the pre-excitation of the acoustic wave: the dark pulse technique [46], the Brillouin dynamic gratings [47], the differential pre-excitation technique [48], the Brillouin echoes [35] and the differential pulse-width pair (DPP) technique [45]. In this thesis, we will focus in the latter one, the DPP, as the preferred choice to achieve centimetric spatial resolution.

3.3.3 Sources of Noise in BOTDA

The signals retrieved by a BOTDA sensor usually suffer the effect of several sources of noise, which also limit the performance of the system. The most common noises are the thermal and shot noises at the receiver stage and the polarization-induced fluctuations in the traces. Thermal and shot noises are responsible for current fluctuations of the detected optical signal in the receiver. Thermal noise is caused by random thermal motion of electrons in a resistor, which manifests even in the absence of optical signal. In the case of a transimpedance-amplified photoreceiver, like the ones typically used, it is defined as [49], [50]:

$$\left\langle i_{ther}^2 \right\rangle = 4kT\frac{B_{eq}}{R_f} + 3.7kT\pi^2\frac{C_t^2 B_{eq}^{\ 3}}{g_m} \tag{3.16}$$

where k is the Boltzman constant ($1.38\times10^{-23}\,J/K$), T is the temperature ($296\,K$), B_{eq} is the equivalent noise bandwidth that is related to the electrical bandwidth of the photodetector ($B_e = 100MHz$) as $B_{eq} = \pi/2\,B_e$, R_f is the transimpedance gain resistance ($40\,k\Omega$), C_t is the total input capacitance of the detector (typ. $8\times10^{-12}\,F$), and g_m, which is the FET transconductance (typ. $5\times10^{-3}\,S$).

On the other hand, shot noise arises because of the discrete nature of the photodetection process. It is a manifestation of the fact that an electric current consists of a stream of electrons that are generated at random times of photon arrival, and it is expressed as [49], [50]:

$$\left\langle i_{shot}^2 \right\rangle = 2e\left(\frac{\eta e(\Delta P_{CW} + P_{CW})}{h\nu} + I_d\right)B_{eq} \tag{3.17}$$

where e is the electronic charge ($1.6\times10^{-19}\ C$), η is the quantum efficiency of the detector (typ. 0.63 for InGaAs detectors of this kind), ΔP_{CW} and P_{CW} are the amplified signal amplitude and the CW respectively, h is the Planck constant ($6.63\times10^{-34}\ Js$), ν is the operating frequency ($193.55\ THz$) and I_d is the dark current of the detector (typ. $0.15\times10^{-9}\ A$). As it will be studied later on in this chapter (Subsection 3.4.1), a particular attention should be paid to these and other extra sources of noise when optimizing BOTDA sensors, mainly if amplification means of the probe wave are utilized.

Another significant source of noise in BOTDA schemes is the polarization noise, which manifests as a variable gain/loss along the fiber length, leading to signal fading in certain positions. As we know, the Brillouin interaction is highly dependent on the degree of parallelism of the States of Polarization (SOPs) of the pump and probe signals [as referred in Eq. (3.5)], a degree which is not maintained in single-mode optical fibers [29]. These fibers are weakly birefringent, causing the pump/probe SOPs to hover around each other. Such changing degree of parallelism results in highly non-uniform Brillouin gain/loss along the fiber length, leading to an apparent noise in the trace [see Figure 3.10(a)] [51]. This polarization noise, in addition, varies in time, thus making an unpredictable contribution to the trace.

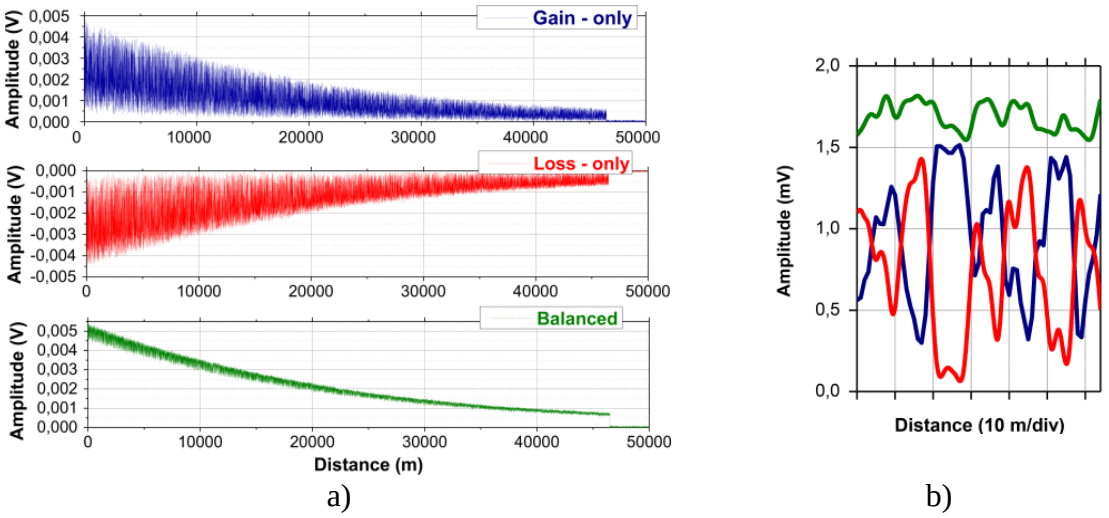

Figure 3.10: Working principle of the elimination of the polarization fading using orthogonal probe sidebands technique. (a) Trace obtained using the single-detector cases (two on top) and balanced detection (one on bottom) for a pump-probe frequency shift of 10.883 GHz. (b) A detail of 64 m of the three traces of Fig (a) around 25 km [52].

A widely spread solution to tackle this problem is to scramble the SOP of one of the interacting waves and average the sensor readings over multiple pump pulses, until a sufficiently high SNR is reached along the entire fiber length. However, doing such procedure significantly slows down the acquisition speed. An alternative solution, which only doubles the acquisition speed, involves the use of a fast polarization switch, where two orthogonal SOPs are sequentially launched into the fiber, and the resulting readings are added, effectively eliminating the polarization fading. Recently, another smart approach to solve this issue has been proposed and demonstrated by Lopez-Gil *et al.* [52], which is related to the principle of operation developed in the forthcoming chapter of this thesis (see Chapter 4). In it, a DSB-BOTDA is implemented, where the Stokes and anti-Stokes components of the probe wave travel along the fiber at orthogonal polarization states. By using a balanced detection scheme among the two sidebands the method effectively achieves a polarization-fading-free trace, as seen in Figure 3.10.

Ultimately, an additional source of noise (although not intrinsic from standard BOTDA schemes) is the Relative Intensity Noise (RIN) introduced by Raman Fiber Lasers (RFLs) when using distributed Raman amplification to boost the BOTDA signals. Its particular description will be thoroughly studied in the forthcoming subsection 3.4.2.

3.4. Addressing the Limits

In this section, a description of the available techniques to overcome the aforementioned limitations of the BOTDA performance will be covered, of course, focusing in describing the approaches more related to the work presented in this thesis.

3.4.1 Pre-Amplification

As previously mentioned, in a BOTDA sensor, the detected signal of interest is a small intensity variation on top of a considerable background level. A typical and simple way of

improving the SNR of the retrieved signal is based on using a pre-amplifier system just before detection. Usually, this stage is formed by introducing an Erbium Doped Fiber Amplifier (EDFA), which may provide up to 30 dB of gain. When dealing with elements that provide gain (G), it is important that all possible noise sources are taken into account. At the photodetector level, it is important to consider the thermal and shot noises, which are depicted in Eq. (3.16) and Eq. (3.17) respectively. However, in this case, the shot noise is also affected by the additional gain delivered by the EDFA, and thus, its expression is now [49], [50]:

$$\left\langle i_{shot}^2 \right\rangle = 2e\left(\frac{\eta e G(\Delta P_{CW} + P_{CW})}{h\nu} + I_d \right) B_{eq} \tag{3.18}$$

As it was shown, thermal noise scales with the temperature and the electrical gain in the photodetector $\left\langle i_{ther}^2 \right\rangle \propto kT/R$, hence it is independent on the amplifier gain. Shot noise, however, turns out to be proportional to the light power, hence $\left\langle i_{shot}^2 \right\rangle \propto G$. Besides photodetector noises, EDFA amplifiers also introduce a large amount of noise. EDFAs produce broadband noise all over the amplification bandwidth known as Amplified Spontaneous Emission (ASE) noise [53]. This is caused by the de-excitation process of the previously excited erbium electrons that produce the amplification. When this de-excitation phenomenon arises spontaneously, a photon is generated that has no coherence with the incoming optical signal. This harmful noise source produces a beating in the photodetector with the amplified signal and with itself, while introducing some additional shot noise (usually small) [50]:

$$\left\langle i_{sig-ASE}^2 \right\rangle = \frac{2(\eta e)^2}{h\nu} F G^2 (\Delta P_{CW} + P_{CW}) B_{eq} \tag{3.19}$$

$$\left\langle i_{ASE-ASE}^2 \right\rangle = (\eta e)^2 F^2 G^2 B_o B_{eq} \tag{3.20}$$

$$\left\langle i_{ASE-shot}^2 \right\rangle = 2e^2 \eta G F B_o B_{eq} \tag{3.21}$$

where F is the optical noise figure of the EDFA [49], and where B_o is the optical bandwidth ($50\ GHz$).

The sig-ASE and ASE-ASE terms are proportional to the square of the gain, hence: $\left\langle i_{sig-ASE}^2 \right\rangle \propto G^2$ and $\left\langle i_{ASE-ASE}^2 \right\rangle \propto G^2$. Also, the ASE-ASE and the ASE-shot terms depend on

the optical bandwidth of the signal entering the detector. The optical SNR can be evaluated in terms of the currents of the detected signal and can be expressed as [50]:

$$SNR_o\left[dB\right] = 10log\left[\frac{GP_s\frac{\eta e}{h\nu}\sqrt{N}}{\sqrt{\sum i^2_{noise}}}\right] \tag{3.22}$$

where N is the number of averages performed on the retrieved signal and $\left\langle i^2_{noise}\right\rangle$ is the current of the different noise sources.

Based on the proportionalities of each noise source, it can be easily seen that the amplification process is essentially interesting to overcome the thermal noise contribution in the detector. Beyond this limit, the other noise terms grow at a rate proportional to the square root of the gain ($\sqrt{G}$) or the gain (G), therefore the SNR is in all cases kept, or even reduced. A thorough study of the contribution of noise sources in pre-amplified BOTDA schemes, among other studies, is presented by Angulo-Vinuesa *et al.* in [49].

3.4.2 Raman amplification

The use of the stimulated Raman effect (see Chapter 2.3.2) as a distributed amplifier has become an important research line in the past decade. It allows extending the sensing range of the systems by compensating the intrinsic fiber attenuation [11]. Raman assistance can be applied as its first-order, where the Raman gain spectrum (RGS) generated by a lower wavelength seed acts as a wide amplification band along the whole fiber span, enhancing the signals of interest. This is known as first-order Raman amplification, and it was first used in BOTDA in 2010 by Rodriguez-Barrios *et al.* [54], achieving a sensing range of 75 km with 2 m of spatial resolution. An alternative scheme can be used, in which an even lower wavelength pump is used as seed to generate amplification over a second pump seed, which at the same time enhances the signals of interest. This is referred as second-order Raman amplification. It was first demonstrated and applied to BOTDA by Martin-Lopez *et al.* [55] in 2010. By combining second-order Raman amplification with pulse coding (see

subsection 3.4.3), Soto *et al.* [56] achieved a sensing range of 120 km in loop configuration (i.e. a total fiber length of 240 km), with a spatial resolution of 5 m, and averaging ~2000 times each frequency. In this thesis, however, first-order Raman amplification is the approach chosen to be implemented.

As it can be seen in Figure 3.11, in the presence of an intense CW Raman pump located at ~ 1455 nm (~ 206 THz), a significantly powerful RGS is generated at a longer wavelength, around ~ 1550 nm (~ 193 THz, i.e. ~ 13 THz difference). Such band is wide enough (~ 7 THz) to cover and amplify the BOTDA signals of interest throughout the fiber.

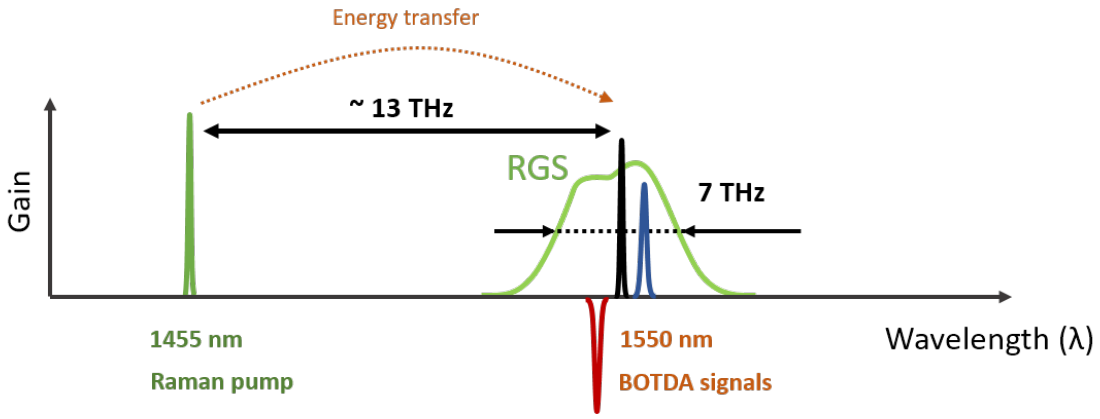

Figure 3.11: Schematic representation of the first-order Raman amplification working principle: a strong Raman pump placed at 1455 nm generates a RGS around 1550 nm, where the BOTDA signals of interest are placed.

The Raman amplification can be applied to BOTDA in different ways, depending on which end of the fiber is used to introduce the Raman pump. Three possible configurations to do so are depicted as follows, being illustrated in Figure 3.12:

- Co-Propagating Amplification (X on - Y off on Figure 3.12): When the Raman pump propagates in the same direction as the BOTDA pump pulse.
- Counter-Propagating Amplification (X off - Y on): In this case, the Raman pump is introduced in opposite direction to the BOTDA pump pulse.
- Bi-Directional Amplification (X on - Y on): The pump is introduced on both sides of the Fiber Under Test (FUT).

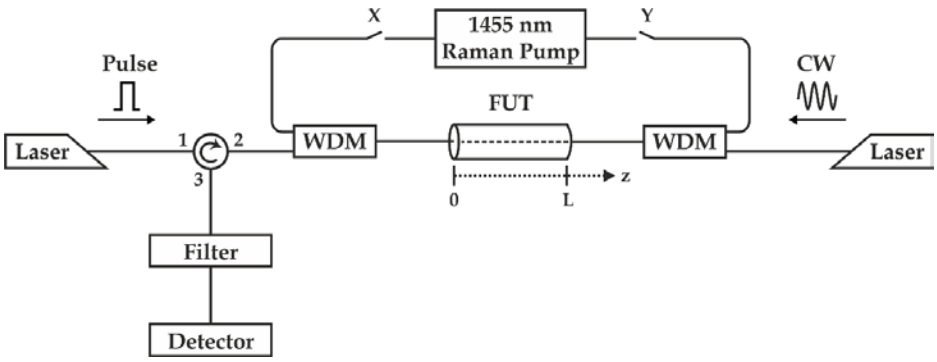

Figure 3.12: Schematic of the first-order Raman-assisted BOTDA. WDM: Wavelength Division Multiplexing; FUT: Fiber Under Test; CW: Continuous Wave [6].

The evolution of the power of all the signals taking part in the Raman-assisted BOTDA differ from one scheme to another. A thorough analysis of such characteristic has been carried out, first by Rodriguez-Barrios *et al.* [54], and then by Nuño [57] in his thesis dissertation. The latter one, as illustrated in Figure 3.13, provides a full modeling of the power evolution of the Raman signals in a large fiber span. In it, it can be observed that the bi-directional approach renders an equi-distributed power profile and, although the co-propagating scheme ("forward pump" in Figure 3.13) performs better over the first half of the link, the bi-directional approach is the preferred option in certain cases, since it ultimately yields a more uniform SNR profile along the fiber. Therefore, such homogeneous performance justifies the selection of the bi-directional Raman configuration as the preferred approach to apply Raman assistance to BOTDA throughout this thesis.

As previously said, in order to generate a significant Raman gain as to properly enhance the BOTDA signals of interest it turns necessary to employ considerably powerful Raman pumps (~ 1 W). Until now, the use of Raman fiber lasers (RFLs) has been the preferred choice when producing strong Raman pumps, since semiconductor lasers were not able to deliver intense-enough pumps. However, RFLs entail an important drawback: they transfer substantial amounts of Relative Intensity Noise (RIN) on the signal. The relative intensity noise describes the instability in the output power of a laser, i.e. its intensity fluctuations [58]. In RFL it originates from small gain variations due to the resonances in the concatenated internal laser cavities [59]. Several works have identified the RIN transfer as a major limitation in Raman

amplified fiber telecommunication systems [60][61]. Of course, such phenomenon has as well a detrimental impact on Raman-assisted BOTDA systems, especially when increasing the measuring range of the sensors.

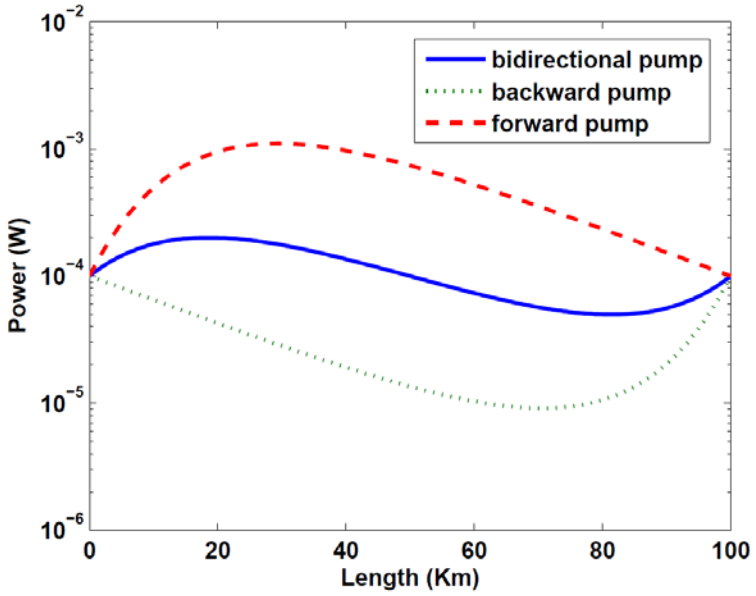

Figure 3.13: Theoretical signal evolution in a transmission fiber for different pumping configurations [57].

The main RIN transfer drawback in Raman-assisted BOTDA sensors relies in the fact that the intensity fluctuations in the Raman pumps induce time-dependent variations in the gain of the BOTDA signals. According to the model proposed by Fludger *et al.* in [60], Angulo-Vinuesa *et al.* [62] quantified the RIN transfer in a 100 km first-order Raman-assisted (bi-directional configuration) BOTDA, for several pump powers, as it can be observed in Figure 3.14. It is clear the RIN manifest in a low-pass-like manner, where the higher transfer is given for frequencies below ~ 100 MHz, i.e. overlapping with the BOTDA signals of interest.

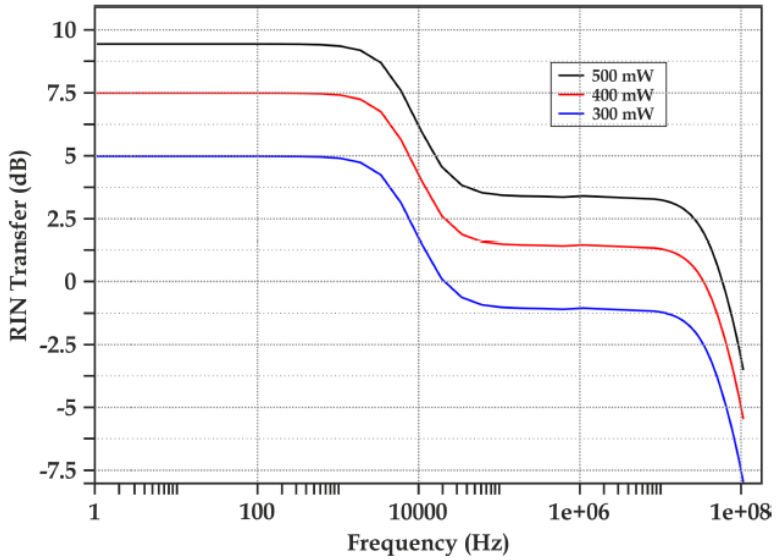

Figure 3.14: RIN transfer spectral representation as a function of the pump power in a first-order bi-directional Raman amplifier [62].

Considering a typical RIN value of Raman lasers of -110 dBc/Hz, the expected RMS noise in this case is expected to be in the order of 10^{-3}, which is in the same order of magnitude as the BOTDA gain to be measured. As the Raman pump increases, the overall RIN grows rapidly. In fact, the RIN growth is faster than the signal gain increase. Hence, the Raman amplification must be used just up to the point of avoiding thermal noise in detection. Several smart approaches have tried to overcome and optimize the RIN transfer issue in Raman amplifiers. The first one makes use of low-noise semiconductor Raman pumps [63], which, as previously said, until now do not deliver pump powers as strong as RFLs do. The second smart approach, suggested by Angulo-Vinuesa *et al.* [64], makes use of the Vector-BOTDA technique [65] , which shifts the BOTDA signals to higher frequencies, i.e. out of the effect of RIN transfer. The effective RIN transfer reduction achieved by this method is ~ 10 dB, at the expense of a more complex implementation. In the following chapters, a simple approach to effectively overcome the RIN transfer will be proposed.

3.4.3 Pulse Coding

Another widely spread technique used to enhance the SNR on BOTDA is the so called *pulse coding* technique. The use of optical coding as a SNR enhancer in time-domain measurement schemes was first presented by Moharir *et al.* [66] in the mid-1970s. The breakthrough, though, was achieved by Jones [67] when employing Simplex codes (S-codes) to enhance the sensitivity of Optical Time-Domain Reflectometers (OTDRs), since it considerably improved the signal dynamic range. The transition of this technique to different time domain sensing techniques has been widely developed and exploited by Soto in his thesis dissertation [31], who successfully applied it for the first time in a BOTDA sensor, reaching 50 km with 1 meter of spatial resolution [68].

This SNR enhancement technique bases its principle on coding the pump wave with a known pulse sequence. The simplest form of coding that has been widely demonstrated is the simplex coding. When introducing a coded sequence of pulses within the fiber, the amplified probe wave is recovered as a linear superposition of all the traces produced by each independent pulse. This phenomenon is schematically represented in Fig.4.

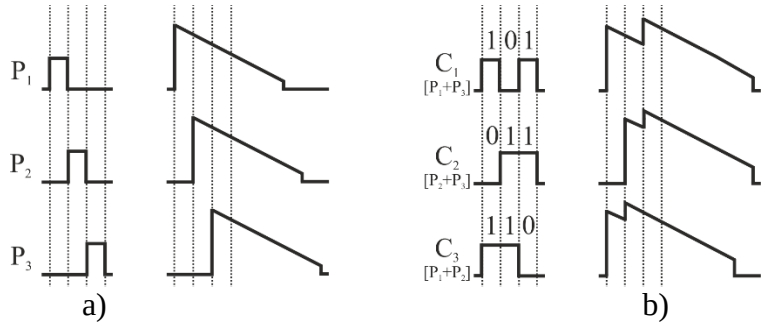

Figure 3.15: Illustration of the retrieved signal with a single pulse (a) and with a linear combination of pulses (b).

Obviously, the fact that superposed traces are present within the fiber increases the received energy level, thus increasing the SNR (when dominated by thermal noise only). After the signal retrieval, through simple algebraic operations, it is possible to isolate each of the

measured traces to obtain the equivalent of a single pulse trace. The gain in signal to noise ratio produced by the code can be expressed as:

$$g_{cod} = \frac{L_C + 1}{2\sqrt{L_C}} \tag{3.23}$$

where g_{cod} is the code gain (equivalent to the overall SNR improvement in the trace retrieval) and L_C is the code length.

The obtained expression scales with the square root of the code-length ($\sqrt{L_C}$), hence, for longer code lengths, more energy will be measured with the consequent SNR improvement. Such SNR enhancement is clearly highlighted in the results obtained by Soto *et al.* [68], which is illustrated in Figure 3.16. Employing a 511 bit simplex code the signal to noise ratio is increased in more than 10 dB.

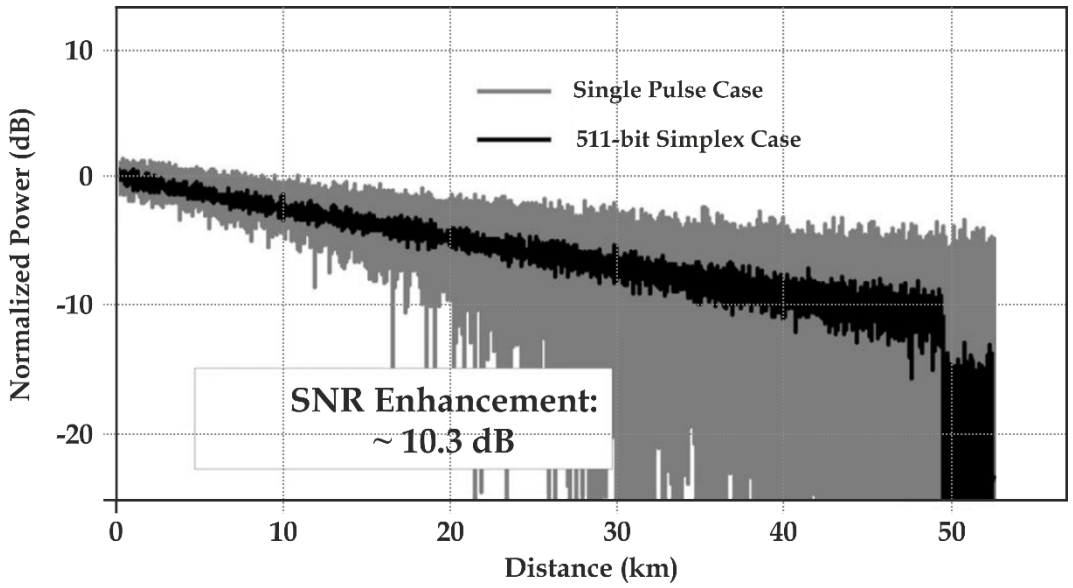

Figure 3.16: Experimental comparison of the results obtained with a simple pump pulse BOTDA and a simplex-coded system [68].

Recently, Iribas *et al.* [69] presented a different coding scheme (cyclic code), combined with probe dithering [70], which allowed them to measure over ~82 km of sensing fiber (164-km loop), featuring a 1 m spatial resolution and 2 MHz of frequency uncertainty.

3.4.4 Differential Pulse-width Pair (DPP)

The differential pulse-width pair (DPP) technique was proposed by Li *et al.* [45] in 2008 as an effective approach to overcome the ~1 m resolution limit in BOTDA sensors. It tackles the fact that for short pulse widths (< 10 ns) the acoustic field does not have enough time to be fully build up, and thus, there is no SBS interaction between pump and probe waves. Its working principle is illustrated in Figure 3.17, and it is based on the acquisition of two consecutive Brillouin gain/loss traces, corresponding to two long pulses of widths T and $T+\Delta T$, where $T >> \tau_A$ (e.g., ~30 ns) is long enough for the acoustic field to develop to its full strength. The differential pulse width ΔT , though, can be way shorter than the pulse width itself, being only limited by the fall-time of the original pulse, i.e., in practice ΔT can be as short as a few hundreds of picoseconds or even less.

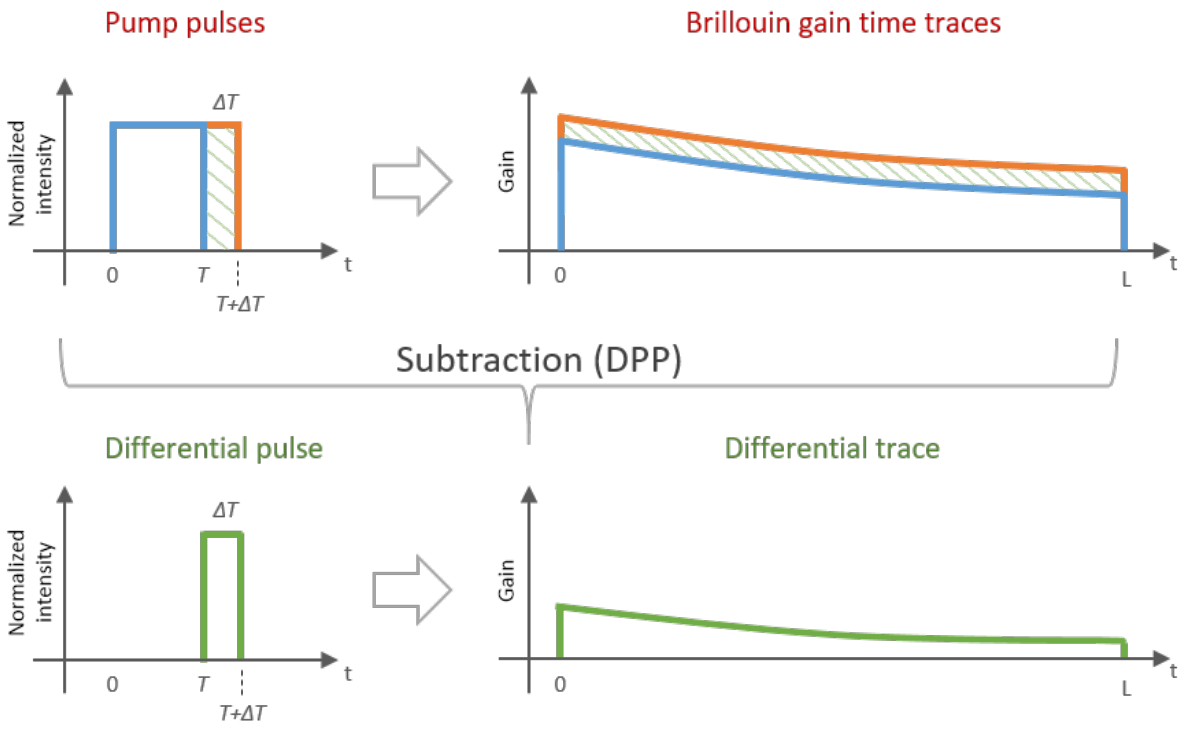

Figure 3.17: Differential pulse-width pair (DPP) working principle: Two Brillouin gain time traces are acquired for two pump pulses of different widths (T and $T+\Delta T$) (top); the subtraction of the two time traces renders a differential trace which is equivalent as a Brillouin trace generated by a pulse of width ΔT (bottom).

While both pump pulses give rise to the same amplification of the probe wave during the common time interval $[0, T]$, only the longer one generates amplification during $T + \Delta T$, since there is no SBS interaction beyond the end of the shorter pump pulse. Thus, subtracting the measured Brillouin amplified probe signal of the short pulse from that of the longer one yields information on the gain in the time slot ΔT, without compromising the shape or strength of $g_B(\nu)$. Note, however, that the shorter ΔT, the shorter the Brillouin interaction length and the lower the SNR [51]. Therefore, in order to apply DPP on BOTDA, it turns critical to ensure well-shaped and squared pulses, since, as previously said, the resulting differential resolution is highly dependent on the falling-edge of the pulse.

The DPP technique has been successfully applied to BOTDA, particularly for long-range sensing schemes. In 2012, Soto *et al.* presented a DPP-BOTDA scheme combined with optical pulse coding (which serves to amplify the gain rendered by the pump, avoiding MI and other undesired effects). In it, they achieve 25 cm of spatial resolution over a 60 km range, representing 250k independent sensing points resolved in the fiber [71].

3.5. Summary

In this chapter, a thorough study of the BOTDA technique has been presented, as well as a review of the more significant limiting factors of the technique, several approaches to overcome them and the current state-of-the-art.

It has been identified that, when trying to push the performance of the BOTDA sensors and increasing the power of the signals intervening, several limitations arise. For long-range schemes, the pump power will be limited by the onset of MI. To avoid MI on the pump wave, its power must be kept below ~100 mW. On the other hand, the probe power, when using DSB modulation to generate it, is said to be limited by the ASpBS threshold, i.e. ~5 mW (~7 dBm) per sideband (we will see later in this thesis that significant distortions arise in DSB-BOTDA schemes even for probe powers well below this value). Using an SSB-probe, though, the limit turns out to be lower, around ~ 40μW (~ -13 dBm) per sideband. In addition, if using a dual-tone probe, pump depletion is avoided whenever the power of the probe sidebands is balanced. Some effective solutions to avoid these power-related detrimental effects are the use of first-order Raman amplifiers or pulse coding techniques. These approaches have also been successfully combined to further exploit their benefits. In some extreme-sensing cases, particularly for long-range measurement distances, the signal power reaching the detector is very low, so pre-amplification schemes are highly suitable to improve the SNR upon detection.

The system spatial resolution is directly linked to the pump pulse width. The ultimate lower limit is set by twice the phonon lifetime, i.e. ~10 ns, which in practice sets the minimum resolution to ~1 m, thus, limiting the number of resolved points along the fiber. Techniques based on correlation domain have recently demonstrated resolving a considerable number of sensing points along the fiber, with resolutions way below 1 m, in spite of long acquisition times. In time-domain schemes, the differential pulse-width pair technique is the selected approach to overcome such limitation and achieve centimetric spatial resolution in BOTDA in a conventional acquisition time, where securing well-shaped square pulses has been identified as a key requirement to guarantee the correct operation of the technique.

In addition, a summarized state-of-the-art is provided, aiming to facilitate its access to the reader at a glance. Such compendium is presented in the following table, for the sake of simplicity:

Table 1: State-of-the-art

Technique	Range	Resolution	Uncertainty	Averages	FoM
Standard BOTDA [27]	51 km	5 m	1 MHz	1024	300
1st-order Raman assisted BOTDA [62]	100 km	2 m	1.2 MHz	65536	110
Pulse Coding + 1st-order Raman [72]	75 km	2.5 m	1 MHz	508	650
Pulse Coding + 2nd-order Raman [56]	120 km *	5 m	1.9 MHz	2040	300k
Pulse Coding + Probe Dithering [69]	82 km *	1 m	3 MHz	16000	7100
Pre-Amp + Pulse Coding [73]	120 km	3 m	3.1 MHz	2000	1800
DPP-BOTDA [74]	2 km	0.02 m	2 MHz	2000	0.1
Pulse Coding + DPP [71]	60 km	0.25 m	1.2 MHz	15330	39
Brillouin Echoes [75]	5 km	0.05 m	1.5 MHz	512	0.2
BOCDA [42]	17.5 km	0.014 m	1.5 MHz	2000	**
BOCDA [44]	17.5 km	0.008 m	1.8 MHz	8000	**

** Fiber loop configuration, i.e. the fiber length is twice the sensing range.*
*** The Figure of Merit is a parameter modelled for BOTDA sensors only, hence, a comparison with other techniques does not apply.*

Chapter 4:
Balanced Detection in BOTDA

4.1. Introduction

One of the main areas of research in BOTDA sensors focuses on the extension of the measuring range, since one of the main field of application is monitoring large civil infrastructures. To do so, it becomes necessary to increase the signal to noise ratio (SNR) of the sensor, in particular considering the reduced signal contrast at the far end of the fiber. One widespread solution to do so has been presented in the previous chapter: the Raman assistance. In this thesis, first-order pumping [54] is the implemented approach. Raman amplification renders a distributed gain along the fiber that allows to partially compensate the inherent fiber losses. This way, the typical exponentially decaying response of the system is avoided, and a sufficient SNR throughout the system is kept. Despite the several advantages Raman assistance provides, it also brings Relative Intensity Noise (RIN) to the detected probe signal, mostly if Raman Fiber Lasers (RFL) are utilized as pumps (see subsection 3.4.2).

As thoroughly explained in the previous chapters (see Chapter 2 and Chapter 3), Brillouin optical time domain analysis relies on the interaction among two counter-propagating waves: a pulsed pump wave and a modulated probe wave. The probe wave is commonly generated

using a DSB modulation as to increase the robustness to non-local effects [40][26], which features two sidebands located at $\pm\nu_B$ with respect to the pump frequency. Conventional systems retrieve the time-resolved gain/loss by detecting only the upper/lower wavelength sideband. In this chapter, we propose the use of a well-known detection technique to increase the SNR: the balanced detection. This detection procedure has resulted in remarkable improvements for several methods [76] in other areas of photonics, such as optical communications [77]–[79] or biomedical applications [80]. In BOTDA, a balanced detection among the Stokes and anti-Stokes probe sidebands doubles the amplitude of the detected signal while the noise only grows by a factor of $\sqrt{2}$, leading to a $\sqrt{2}$ SNR increase. Moreover, any common-mode noise in the probe signal path (e.g. master laser noise, modulator drifts, etc.) is eliminated, rendering the system more robust. Thus, this particular approach turns extremely suitable to cancel out the RIN transfer delivered when using Raman assistance as an extending-range technique. The principle is experimentally validated for both the conventional and Raman-assisted BOTDA schemes, highlighting the inexpensive improvement in terms of signal-to-noise ratio.

4.2. Principles

Stimulated Brillouin Scattering (SBS) features two side bands: the Stokes (gain) and Anti-Stokes (loss) bands (see Chapter 2 for further details). To take advantage of the SBS phenomenon, a single sideband (SSB) modulator can be used at the probe signal to work at Brillouin gain frequency (Stokes band) or at Brillouin loss frequency (anti-Stokes band). However, as thoroughly studied in Chapter 3, making use of a dual sideband (DSB) modulator to generate both Stokes and Anti-Stokes bands, the effect of pump depletion can be effectively mitigated [26], [40]. For this reason, DSB modulation turns out to be the preferred option in long-range setups. In conventional BOTDA, one of the two sidebands (Stokes or anti-Stokes) is filtered in detection and fed into a conventional photo-receiver for analysis.

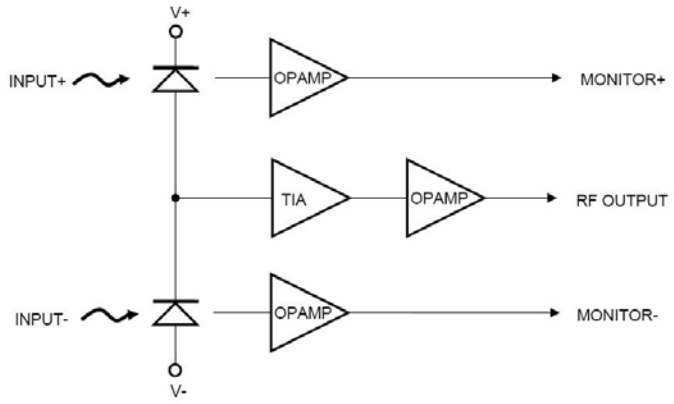

Figure 4.1: Functional block diagram of a balanced photodetector (Thorlabs PDB410C).

In balanced detection, the receiver features two well matched photodiodes. As illustrated in Figure 3.14, two light beams (Input+ and Input- in the figure) are fed into the corresponding photodiode and the obtained currents are subtracted. Ultimately, the remaining current difference is amplified through a trans-impedance amplifier. This technique allows for the detection of small signal variations over substantial DC levels. In this chapter, we show how advantageous a balanced detection among the Stokes and anti-Stokes bands can be in BOTDA, where the differential output will be the result of subtracting the negative input signal (Brillouin loss) to the positive input signal (Brillouin gain).

For a given position z along the fiber, as depicted in Eq. (3.2) the signal change recorded in the Stokes band will be proportional to:

$$\Delta P_S(z) \propto +g_B P_P(z) P_S(z) \Delta z \tag{4.1}$$

where g_B is the Brillouin gain coefficient, P_P is the pump pulse power, P_S is the Stokes wave power and Δz is the pulse length. Conversely, in the anti-Stokes band, the signal change will be proportional to:

$$\Delta P_S(z) \propto -g_B P_P(z) P_{AS}(z) \Delta z \tag{4.2}$$

where P_{AS} is the anti-Stokes power. After the balanced detection scheme, the overall signal change will be proportional to:

$$\Delta P_{S-AS}(z) \propto +g_B P_P(z)[P_S(z) + P_{AS}(z)]\Delta z \tag{4.3}$$

In typical conditions (when an external Mach-Zehnder electro-optic modulator is employed), P_S is equal to P_{AS}, and the detected signal will be naturally doubled in comparison with a single-detector scheme of equal responsivity.

It is interesting now to think what happens in terms of the noise. Considering equal noise characteristics for the two input photodiodes, the use of balanced detection will lead to an increase of the noise of only $\sqrt{2}$ (sum of two independent equally-distributed random variables). Thus, an overall improvement of $\sqrt{2}$ in SNR should be expected in this configuration over a conventional single-detector option.

In addition to the previous discussion, this detection technique has an additional number of advantages: in the first place, it makes the system strongly robust to common-mode noise sources (noise sources affecting equally both bands). Common noise sources may include: master laser intensity noise, modulator drifts, varying coupling losses in the fiber, etc. However, effective common-mode intensity noise cancellation will occur solely when optical path lengths for both sidebands are equal before reaching the detector. In addition, the use of DC-coupled balanced detection allows for the amplification of the signal to higher values compared to DC-coupled single sideband detection, due to the fact that the DC levels of both independent signals are subtracted previous to the amplifying stage at the receiver, which means that the receiver clamps at a higher value of signal amplitude.

4.3. Balanced Detection in Conventional BOTDA

To prove the above advantages in a conventional BOTDA, we developed the BOTDA scheme represented in Figure 4.2. It is a variation of a standard DSB-BOTDA system, though incorporating balanced detection.

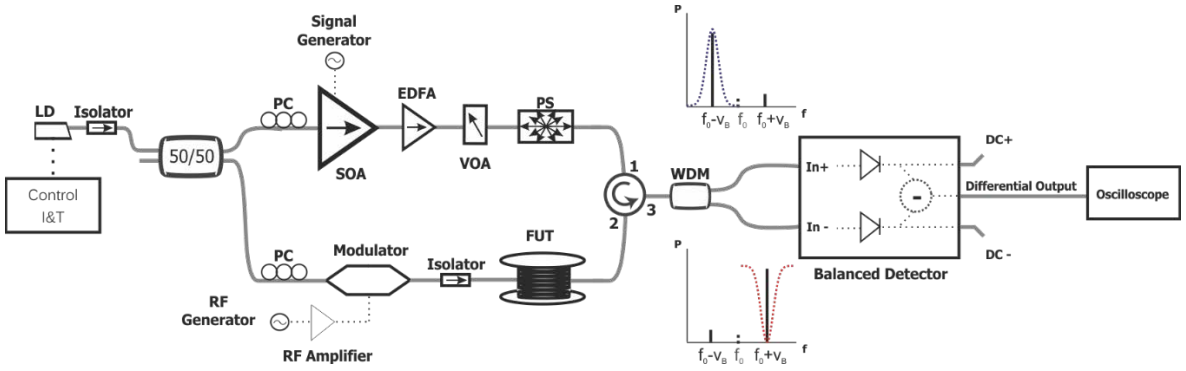

Figure 4.2: Experimental setup of the BOTDA with Balanced Detection. LD: Laser Diode; PC: Polarization controller; EDFA: Erbium Doped Fiber Amplifier; RF: Radio-frequency generator; VOA: Variable Optical Attenuator; PS: Polarization Scrambler; WDM: Wavelength Division Multiplexer [81].

As in most BOTDA setups, pump and probe waves are developed from a single Distributed Feed-Back (DFB) laser diode [24]. A Mach-Zehnder Electro-Optic Modulator (EOM) is used to make a Dual Side-Band with Suppressed Carrier (DSB-SC) modulation. The Extinction Ratio (ER) of the EOM is >40 dB, and thus, it is possible to nearly eliminate the carrier signal. The probe power fed into the fiber is ~60 μW on each sideband. The modulating frequency of the EOM is controlled through an RF generator whose frequency is chosen to sweep around the BFS of the fiber under test.

At the pump side, the signal is pulsed using a Semiconductor Optical Amplifier (SOA). The SOA allows to shape high extinction ratio (>30 dB) optical pulses. The pulse width used in the experiment is 40 ns (which implies that the sensor features 4 meters of spatial resolution), and the pulse peak power provided is ~100 mW. After pulsing, the optical signal is amplified by means of an Erbium Doped Fiber Amplifier (EDFA). The power of the pulses is controlled through a Variable Optical Attenuator (VOA) and their polarization is scrambled by a fast polarization scrambler. Although this scrambler is very fast (5 MHz of scrambling rate), the scrambling of the polarization state was imperfect, leading to some polarization noise in the trace as we will see in the results section.

After going through the fiber and experiencing SBS, the signal is split using a conventional 100 GHz Dense Wavelength Division Multiplexing (DWDM), which separates Brillouin gain (Stokes) and Brillouin loss (anti-Stokes). The filter used is sharp enough to

separate both sidebands correctly, attenuating the rejected band in >13 dB. These two different bands are then fed to the positive and negative ports of the balanced detection system. Ultimately, the employed balanced detection system (see Figure 3.14) will provide three different output signals: the differential output (carrying the signal of interest), and two monitoring outputs, where we will read the DC levels of each of the input signals.

In general, for BOTDA systems, the acquired signal is a slight amplitude variation upon a significant background DC level. To obtain meaningful gain values, it is necessary to normalize the obtained signal values by the background DC level of the signal, which is a measure of the background Stokes (P_S) or anti-Stokes power (P_{AS}).

In balanced detection, the obtained signal has usually a small (close to zero) DC level, as the DC levels of the two photocurrents also get subtracted in the process. Thus, the DC level of the differential output cannot be used for the normalization. To obtain a correct normalization, it is necessary to monitor the DC levels of the two input signals separately and sum them. This is a measure of $P_S + P_{AS}$. With this value, a correct normalization of the differential output signal can be performed. Conventional balanced detectors typically provide these outputs, so this process is rather straightforward to do with current off-the-shelf instrumentation.

4.3.1 Experimental Results

In this section we illustrate the results obtained with the BOTDA using the balanced detection configuration described previously. To obtain meaningful comparisons, the measurements have always been carried out with the same scheme, first using the gain band only (gain-only measurements), then the loss band only (loss-only measurements), and finally the balanced detection with both gain and loss bands (balanced measurements). The same amount of averages is used in all cases (1024).

The measurements are performed over ~50 km of single mode fiber (SMF) with an essentially homogeneous Brillouin frequency shift located at 10.883 GHz at the pump wavelength (~1550 nm).

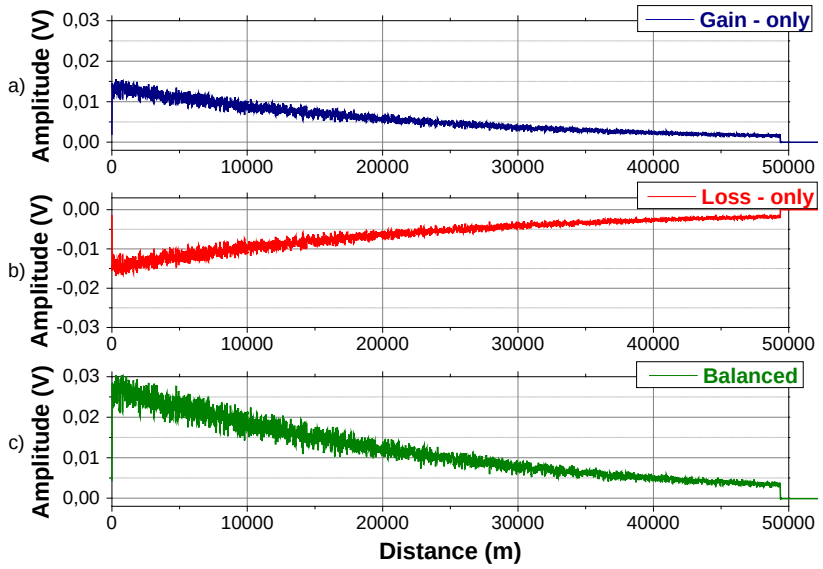

Figure 4.3: BOTDA amplitude time-traces for: single sideband detection cases (a), (b) and balanced detection (c) for a pump-probe frequency shift of 10.883 GHz [81].

The first remarkable result is that when acquiring in balanced mode, the trace amplitude of the differential output is twice the amplitude of any of the single sidebands, as illustrated in Figure 4.3. This is an expected result considering the reasoning given in subsection 4.2. Doubling the trace amplitude increases the signal contrast by 3 dB, which is potentially equivalent to 15 km of fiber. It also leads to a theoretical $\sqrt{2}$ SNR increase, as shown before. In addition, balanced detection increases the robustness of the system to common-mode noises, which may affect both sidebands.

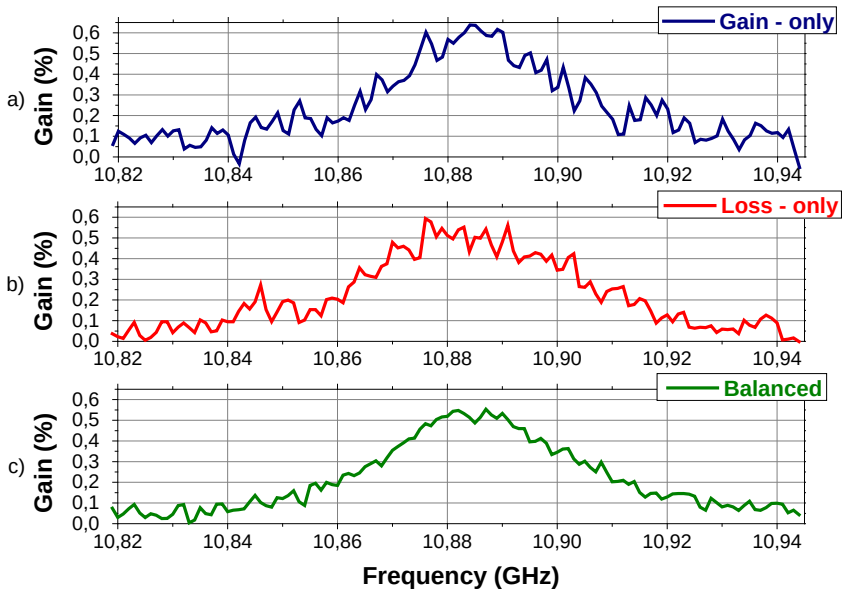

Figure 4.4: Gain profiles at 46.818 km for a frequency sweep between 10.82 GHz and 10.95 GHz: a) Brillouin gain spectrum (BGS) acquired profile (Stokes band); b) Brillouin loss spectrum (BLS) absolute value profile (anti-Stokes band); c) Differential output acquired profile.[81].

Figure 4.4 shows three gain profiles at a distance of 46.818 km, with a frequency sweep done from 10.82 GHz to 10.95 GHz. As it can be inferred, the noise of the differential output gain profile [Figure 4.4(c)] is visibly reduced compared to the gain profiles of the single Brillouin gain [Figure 4.4(a)] and Brillouin loss [Figure 4.4(b)] sidebands.

Once the frequency sweep is finished, the BFS is obtained by fitting a 2nd order polynomial curve to the raw gain profile, and then finding the position of the maximum of the curve. As shown in Figure 4.5, finding the BFS at any point of the fiber is more accurate when balanced detection is employed. The standard deviation of the obtained BFS between five consecutive traces at the very beginning of the fiber (first 5000 points window) is ~0.618 MHz for both single sidebands acquisitions and ~0.432 MHz for the balanced case. The standard deviation is improved by a factor of ~ $\sqrt{2}$, in consistency with the SNR improvement expected in the balanced case (see [32] for details on the relationship between SNR and frequency estimation error). At the end of the fiber under test (last 5000 points window), the standard deviation for the single sideband cases is ~1.232 MHz and, as expected, for the balanced detection case it is ~0.884 MHz, also resulting in an improvement ratio of ~ $\sqrt{2}$. In terms of the figure-of-merit

discussed by Soto *et al.* [32] (see Section 3.2.1), the FoM calculated at the end of the fiber is 25.28 for the single sideband detection cases, and raises up to 35.24 for the balanced detection case, confirming the ~ $\sqrt{2}$ improvement factor.

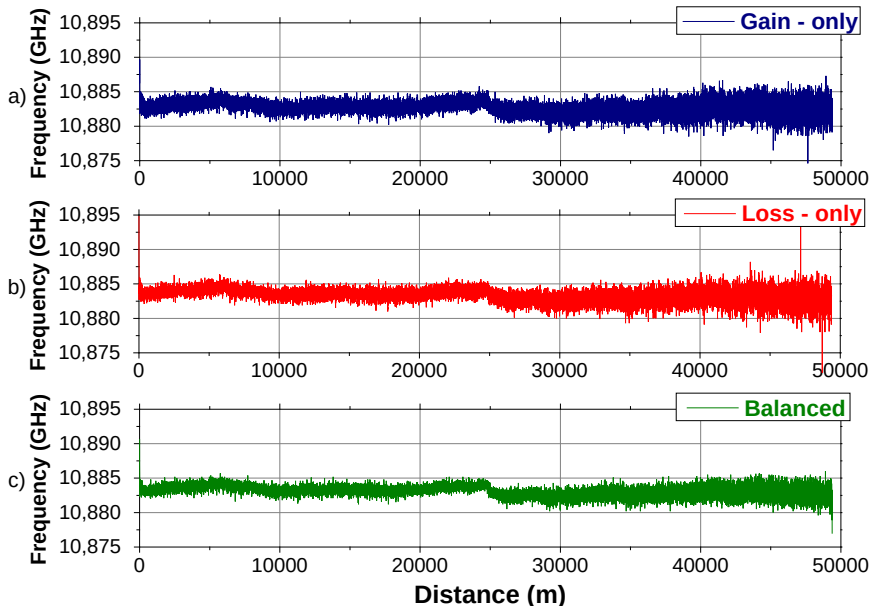

Figure 4.5: Brillouin frequency shift for the single sideband acquisition cases (a), (b) and the balanced detection acquisition (c) for ~50 km of SMF [81].

A final interesting feature of the balanced detection system is that the overall response of the system turns out to be more robust to some of the variables of the experiment. One of these important variables to control is the pulse ER. As stated previously, the SOA employed is electrically controlled by a signal generator. In normal conditions, it is intended to work at the highest ER the SOA could provide. Having a high extinction ratio pulse is crucial when aiming for a good SNR. However, employing an SOA is an advanced solution and it is not always available. In exchange we can easily find conventional EOMs pulsing the pump beam, which normally have lower extinction ratio. In our case, the extinction ratio is deteriorated on purpose by varying the logical high and low voltage levels of the electrical pulse controlling the SOA.

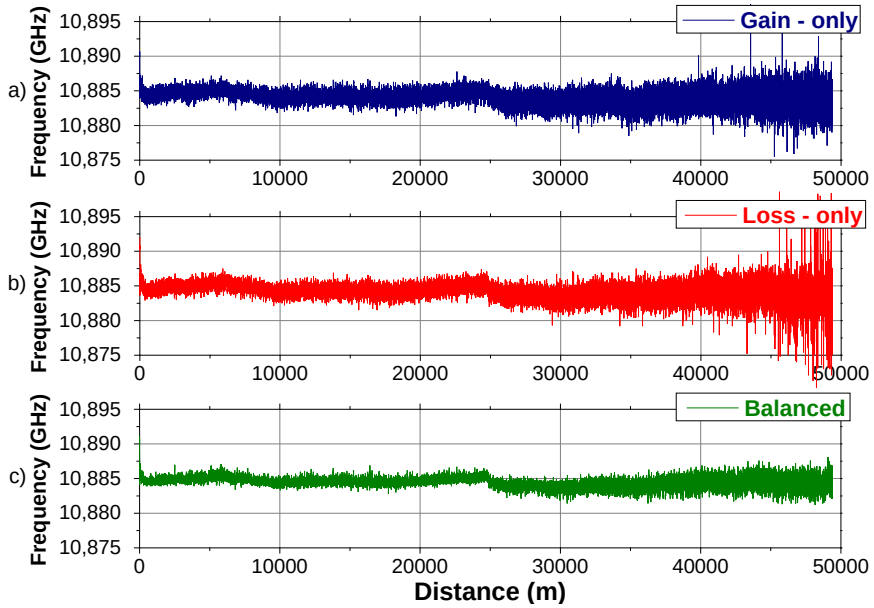

Figure 4.6: Brillouin frequency shift for the single sideband acquisition cases (a), (b) and the balanced detection acquisition (c) for ~50 km of SMF and deteriorating the Extinction Ratio of the SOA (27 dB ER).[81].

BOTDA using balanced detection becomes more robust to the deterioration of the pulse extinction ratio. Figure 4.6 shows the BFS profiles obtained for an ER of the SOA of 27 dB in comparison to the 34 dB ER case of Figure 4.5.

The standard deviation of the obtained BFS between five consecutive traces calculated for the worst ER scenario achieved (27 dB ER) remains roughly the same at the beginning of the fiber. For the single sideband cases it is ~0.625 MHz and once again, for the balanced acquisition it is ~0.438 MHz, resulting in an improvement factor of $\sim\sqrt{2}$. However, the standard deviation at the end of the fiber is ~1.759 MHz for the single sideband acquisitions and ~0.891 MHz for the balanced detection case, which means, the standard deviation of the obtained BFS for the single sideband cases is more than double the uncertainty of the balanced case.

For any of the single sideband acquisitions, the fitting and finding the maximum processes might lead to points with extreme error, which are often observed at the end of the fiber. This situation is caused by the appearance of extreme peaks in the gain profile at that position, which perturb the fitting process. As it can be seen, the misleading points in the fitting and finding

the maximum procedure are substantially avoided in the balanced case, even using raw gain profiles.

The remarkable feature of employing balanced detection is that the frequency uncertainty of the obtained BFS at the end of the fiber remains stable (~0.89 MHz) as the ER is worsened, showing an improved robustness to the deterioration of this experimental parameter.

4.4. Strong RIN Transfer Cancellation in a Raman-assisted BOTDA using Balanced Detection.

As previously demonstrated, when the BOTDA probe sidebands show no common-mode intensity noise, the summation of the two input noises coming from the two photodetectors renders an increase of $\sqrt{2}$ in noise. As the trace signal is doubled, the overall result is an SNR improvement of $\sqrt{2}$. However, the SNR increase is much larger when there is any perturbation affecting both bands equally (common-mode noise). Such perturbation will be effectively cancelled by applying balanced detection. This is the case of the Raman amplification, where the use of high power RFLs entails a great amount of RIN transferred to the probe wave, and where balanced detection, as it will be demonstrated in this section, will effectively eliminate such RIN transfer.

To explore the improvement given by balanced detection in Raman-assisted configurations, we have developed the scheme represented in Figure 4.7. It is an evolution of a previous first-order Raman assisted BOTDA setup prepared by Angulo-Vinuesa *et al.* [62], where the detection scheme has been modified to include balanced detection.

The implemented experimental setup is analogous to the one describe in Section 4.3 (see Figure 4.2), where pump and probe waves are developed from a single laser source. The probe wave is DSB-SC modulated by means of a high-ER EOM, and the power of each sideband is ~60 μW. The RF generator controls the frequency sweep performed by means of the EOM around the BFS of the fiber.

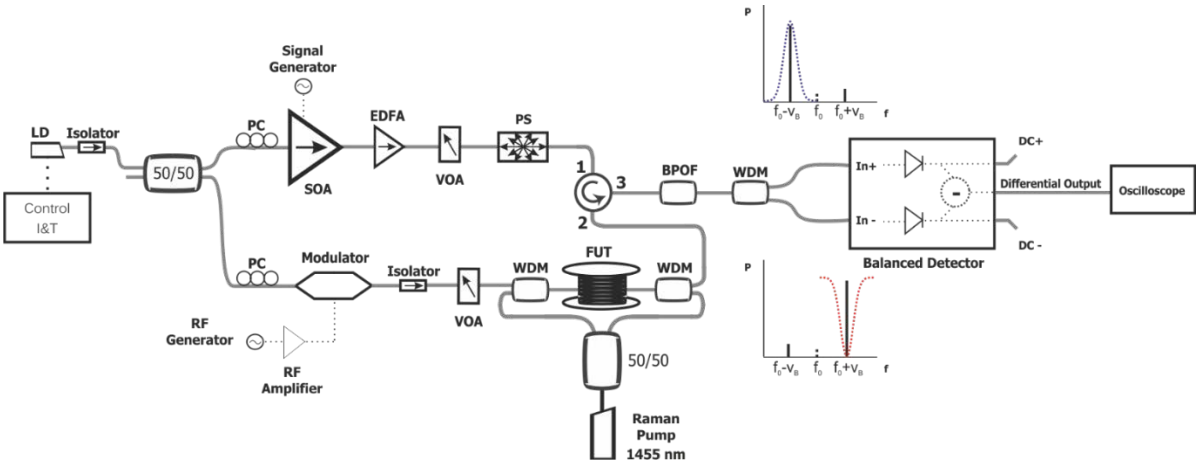

Figure 4.7: Experimental setup of the first-order Raman assisted BOTDA with balanced detection. LD: Laser Diode; PC: Polarization controller; EDFA: Erbium Doped Fiber Amplifier; VOA: Variable Optical Attenuator; PS: Polarization Scrambler; FUT: Fiber Under Test; WDM: Wavelength Division Multiplexer; BPOF: Band-Pass Optical Filter [82].

At the pump side, the signal is pulsed using a high-ER SOA. The pulse width used is 20 ns, which implies a system spatial resolution of 2 meters. The pulses are then amplified by means of an EDFA, and before getting into the fiber, their polarization is scrambled by a fast polarization scrambler. The peak power of the pulses fed into the fiber is ~10 mW in this case.

In this case, a RFL is employed to provide first-order bi-directional Raman amplification to the system, ensuring a sufficient signal level across the fiber (see Section 3.4.2 for more details). The Raman pump power introduced is ~240 mW on each propagation direction at a pump wavelength of ~1455 nm (480 mW total power). Two WDM couplers are used to combine the Raman pumps and the Brillouin signals.

After going through the fiber and experiencing SBS, a Band-Pass Optical Filter (BPOF) with a 10-dB bandwidth of 2 nm is used to eliminate most of the amplified spontaneous emission (ASE) noise introduced by Raman amplification, leaving just the two sidebands of interest. The probe sidebands are then separated using a DWDM filter. The edge of the filter used is sharp enough to separate both sidebands correctly, attenuating the rejected band in >13 dB. The Brillouin gain band (Stokes) is fed into the positive port of the balanced detector, and Brillouin loss band (Anti-Stokes) is fed into the negative port. It must be noted, as pointed out in the previous section, that effective common-mode noise cancellation will occur solely

when optical lengths for both sidebands are equal before reaching the detector. Thus, care is taken to ensure that the fiber lengths covered by each sideband after separation are the same.

Ultimately, the balanced detection system provides the differential output (signal of interest) and the necessary signals to perform the correct normalization explained before (see Section 4.3).

4.4.1 RIN Cancellation

A high amount of RIN transfer is expected in the present Raman-assisted BOTDA setup, and thus, it turns necessary to verify the balanced detection outcomes in terms of common-mode noise cancellation. To do so, measurements have been performed over ~100 km of single-mode fiber (SMF) with an essentially homogeneous Brillouin frequency shift located at 10.865 GHz at the pump wavelength (~1550 nm). The acquired traces have always been averaged 1024 times.

The first and most notable result is that, when acquiring in balanced mode, an effective cancellation of the RFL RIN transfer is accomplished. To evidence this, we performed electrical spectrum measurements of the intensity noise measured in detection, either using conventional (single-sideband) or balanced detection. Figure 4.8 shows the electrical spectra of the detected probe wave acquired in both detection setups, for a total Raman pump power of 360 mW (180 mW per each side). In single-sideband acquisition, the RIN transfer is well visible as a set of peaks with a periodic spacing of ~1.5 MHz. This frequency is given by the inverse of the cavity round-trip time of the primary Yb oscillator in the RFL. As it is visible, these RIN noise peaks are completely eliminated in the balanced detection case [82]. This is an expected result due to the fact that the RIN is common to both the Brillouin gain and loss bands.

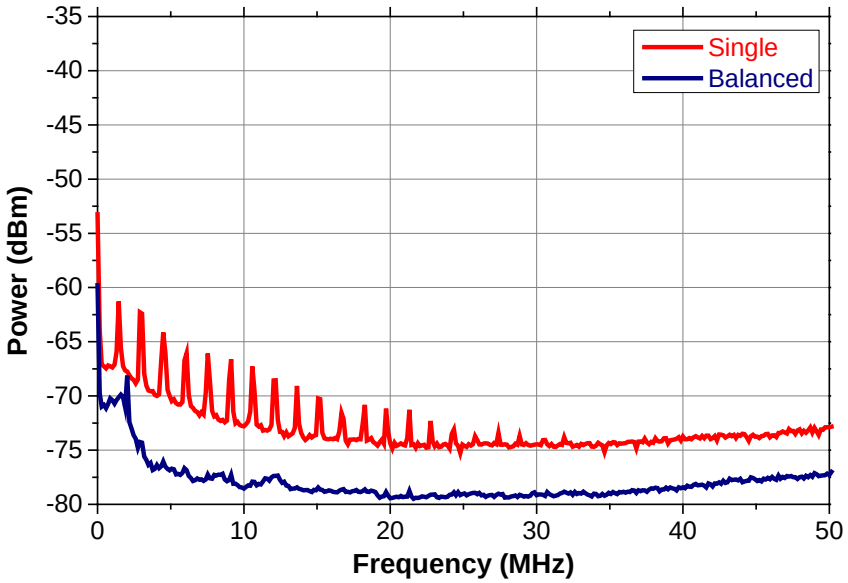

Figure 4.8: Electrical spectra of the detected probe wave recorded for a total Raman pump power of ~360 mW (30 kHz of resolution bandwidth) Filter [82].

To challenge the noise cancellation limits of the proposed detection procedure, we repeated the same measurement but raising the Raman pump power up to 480 mW (240 mW per each side). At this particular power, the RFL used brings a powerful noise peak at 44 MHz. The results are displayed in Figure 4.9. As it is visible, the cancellation of the RIN noise peaks is >15 dB for frequencies below 10 MHz. However, the strong peak at 44 MHz is just reduced in ~10 dB. Although this is a significant reduction of noise, complete and perfect noise cancellation has not been achieved in this particular case. This is due to several setup defects: First of all, the small differences in the optical path lengths (±1 cm in our setup) of the two single sidebands could lead to a small mismatch when arriving to the receiver, and thus, unbalance slightly the noise cancellation at high frequencies. In addition, the master laser source wavelength should be perfectly tuned in order to have exactly the same amount of probe wave detected on each port of the balanced detector. Any minimal error in the process of adjusting these parameters could lead in a non-symmetric separation of Brillouin gain and loss bands previous to detection, which would, once again, cause an imperfect noise cancellation. These non-idealities tend to impact the noise cancellation more severely at high frequencies. Nevertheless, high-frequency noise turns out to be more easily cancelled out in the

conventional averaging procedure that is usually done in BOTDA. Hence we can safely affirm that most of the RIN transfer issues can be effectively avoided by using this configuration.

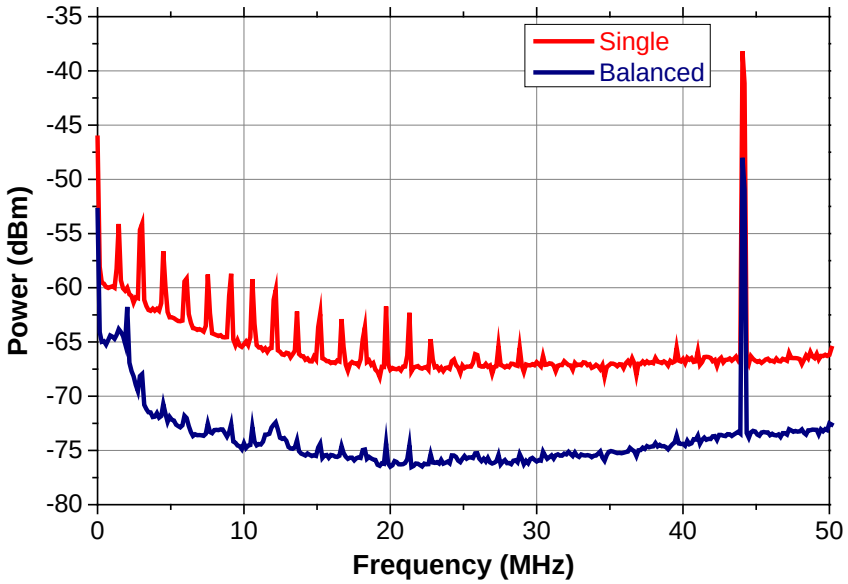

Figure 4.9: Electrical spectra of the detected probe wave recorded for a total Raman pump power of ~480 mW (30 kHz of resolution bandwidth) [82].

4.4.2 BOTDA Measurements

To have a close to perfect RIN cancellation, we set the total Raman pump power back to 360 mW. Using these settings, we performed BOTDA trace measurements over the complete length of 100 km with 2 meter spatial resolution (20 ns pump pulse duration).

To accomplish these BOTDA measurements, a frequency sweep is done from 10.75 GHz to 10.95 GHz. Once the frequency sweep is finished, the BFS profile is obtained by fitting a 2nd order polynomial curve to the raw gain profile, and then finding the position of the maximum of the curve. For each frequency step, only 1024 averages are carried out. Figure 4.10 shows a ~100 km amplitude trace using balanced detection for a pump-probe frequency shift of 10.865 GHz. The trace reveals the imperfect polarization scrambling that was carried out, showing a larger polarization noise in the first kilometers of the fiber under test. The actual

measured trace noise is comparable to the trace noise in other Raman-assisted BOTDA experiments over the same distance with 64 times more averaging [62].

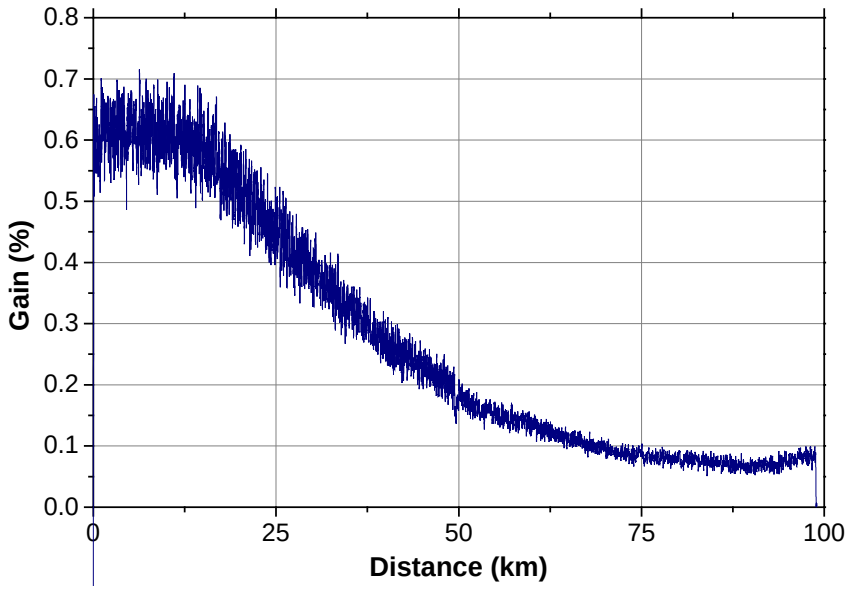

Figure 4.10: First-order bi-directional Raman assisted BOTDA gain trace using BD for a pump-probe frequency shift of 10.865 GHz and a total Raman pump power of ~360 mW [82].

To further verify the performance of the setup as a sensor, a hot-spot is placed in the position of worst contrast of the fiber (around 75 km). This is done by immersing ~2 meters of fiber in a hot water bath. Again, a full frequency sweep is performed to retrieve the Brillouin Frequency Shift change in the position of the hot-spot. The results of temperature change around the hot-spot are visible in Figure 4.11. The process of translating frequency to temperature difference is rather straightforward due to the fact that the relation temperature-frequency is linear (~ 1 ºC/MHz) (see Figure 2.8). A ~22 ºC elevation over room temperature was recorded in the hot-spot location. The system performs properly as a temperature sensor, as the temperature elevation is correctly verified with an external thermometer.

The sensing uncertainty (estimated as the standard deviation of the repeatability in 5 consecutive measurements) around the hot-spot (1000 m window) was ± 2 ºC. The hot spot is also correctly identified as being ~2-meter wide.

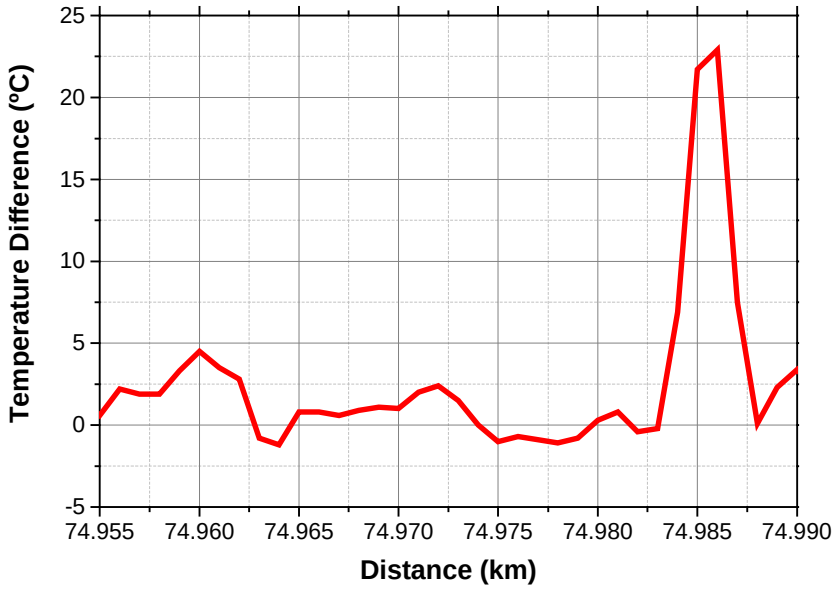

Figure 4.11: Brillouin frequency shift translated to temperature difference around a ~2-meter hot-spot (located around 75 km) [82].

It is interesting to compare now this setup, in terms of figure of merit (FoM) [32] (see Section 3.2.1), with the same setup not using balanced detection [62]. While in [62] the estimated FoM was 108, in the present setup, the FoM has been raised to 500, which implies a fivefold improvement. Therefore, on top of the expected improvement of $\sqrt{2}$ just by using balanced detection, there is an extra improvement factor of 3.5 given by the elimination of the RIN transfer. This highlights the importance of managing RIN in these Raman-assisted BOTDA systems. In terms of RIN removal, it should be noted that the FoM improvement achieved in this case is much better than when using a numerical denoising procedure [83].

4.5. Conclusions

In this chapter, it has been presented the application of a well-known detection technique, the balanced detection, to BOTDA systems. It has been shown, both theoretically and experimentally, that remarkable and easy-to-implement improvements in terms of SNR can be obtained. In typical conditions, the trace amplitude is doubled and the SNR is improved by a factor of $\sqrt{2}$. The system has demonstrated a strong robustness to the deterioration of the

pump pulse extinction ratio, which could ease the technical requirements of BOTDA implementations.

In addition, the technique has proven to be extremely effective in cancelling common-mode noise. Making use of the balanced detection when extending the BOTDA sensing performance by means of Raman-assistance, effectively eliminates the RIN transfer (as the Raman-induced RIN is equally transferred to both probe sidebands). The use of balanced detection in the same Raman-assisted setup implies a fivefold increase in FoM compared to the conventional single-detector option. Moreover, we now have a clear measure of the potential improvement in FoM given by Raman assistance in any BOTDA setup, regardless of RIN noise issues.

We envisage that, by using this methodology, an almost zero RIN transfer scenario is feasible in most Raman-assisted BOTDA configurations (including second-order). The possible non-idealities of the setup have also been discussed (unequal optical path lengths for both Brillouin gain and loss bands, optimal tuning of the laser with respect to the filters, etc.).

Chapter 5:
Non-local Effects in a Dual-Probe-Sideband BOTDA

5.1. Introduction

As deeply studied in the previous chapter, BOTDA schemes rely on mapping the Stimulated Brillouin Scattering (SBS) characteristics along the length of an optical fiber [18], [23], [84]. The basic assumption of the measurement technique is that the power lost or gained by the pump pulse through SBS is negligible in comparison to the total pulse power [25]. This is the only way to ensure that strictly local information is retrieved from the variations of the probe beam. Non-local effects in these systems appear when the integrated power transfer from pump to probe is non-negligible in comparison to the total pump power. These situations are of important concern, as they cause deformations of the observed Brillouin gain/loss curves, which lead to errors in the determination of the BFS as a function of the position. The exact error introduced depends on the whole BFS landscape of the fiber, and this is why these

impairments in the measurement are termed as “non-local effects”. Several strategies to avoid non-local effects have been put forward in the literature [26], [85].

According to recent models [25], [26], [40], [86], pump depletion and non-local effects in dual-probe-sideband BOTDA systems should be essentially negligible whenever the probe power is below the ASpBS threshold. However, in this chapter the appearance of non-local effects in this type of systems for powers way below such threshold is thoroughly demonstrated. To explain these effects it is necessary to take into account a full spectral description of the SBS process. The pump pulse experiences a frequency-dependent temporal and spectral deformation that originates from the conventional pump-probe frequency offset scanning. The pump pulse distortion affects the Brillouin gain and loss spectra and scales proportionally to the probe power. Two probe power regimes are here defined: First, a low-to-medium power regime (up to -3 dBm/sideband) where, although there appear significant distortions in the pump pulse (and therefore in the BGS and BLS), it permits a reasonable determination of the BFS, affecting the readout process differently in the gain and loss configurations. A simple analytical model of this phenomenon is provided, which is validated against compelling experimental data, showing good agreement. In the high-power regime (up to the ASpBS threshold), the massive pump pulse distortions give rise to huge deformations of the retrieved Brillouin gain and loss profiles, besides dramatically affecting the spatial resolution of the system. Such deformations can be intense enough to even conceal any BFS local change, thus, annulling the sensing capacity of the system.

5.2. Low-to-Medium Probe Power Regime

When using a DSB modulation to generate the probe, as fully explained in Section 3.2, its higher frequency sideband (which scans the Brillouin loss process) provides power to the pump pulse, and at the same time, the pump pulse provides power to the lower frequency probe sideband (that scans the Brillouin gain). This situation can be analyzed in the analogous way in which the higher and lower frequency sidebands of the probe generate, respectively, a gain (red curves in Figure 5.1) and loss (blue curves in Figure 5.1) around the pump frequency.

Depending on the pump-probe frequency offset, the relative position of the gain and loss signatures and the pump pulse can be different, as shown in Figure 5.1.

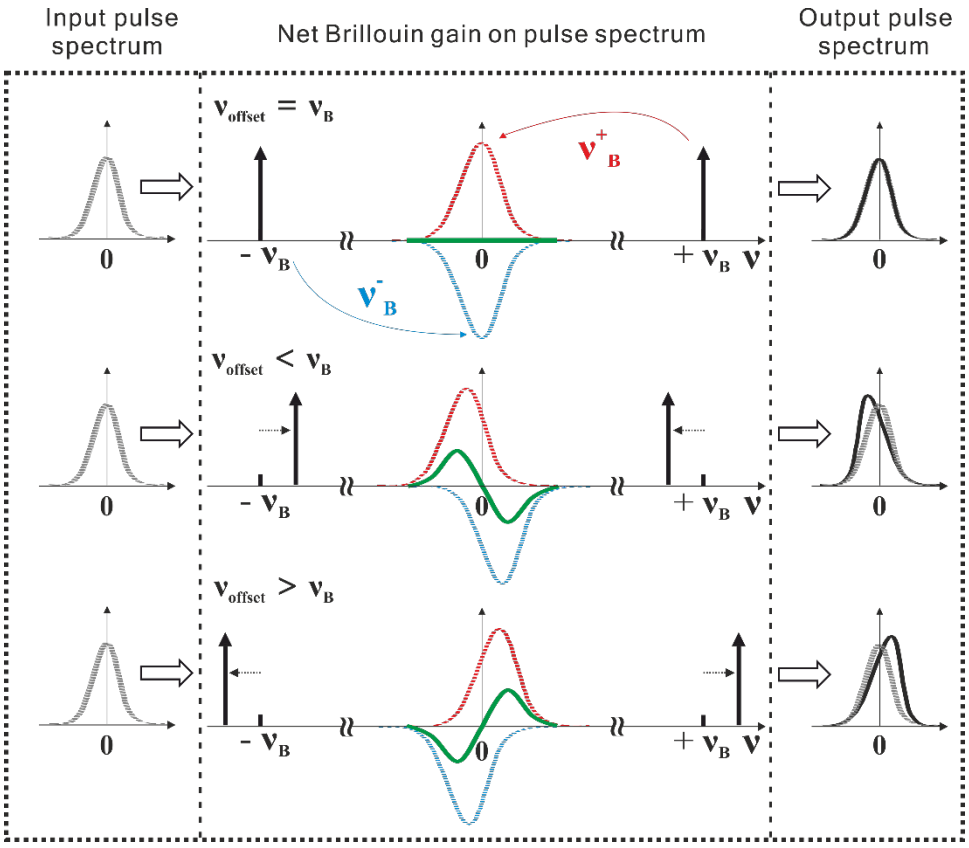

Figure 5.1: Net Brillouin gain affecting the pump pulse while scanning the pump-probe frequency offset (ν_{offset}) symmetrically around the pulse spectrum in a conventional BOTDA scheme. Grey dotted lines: input pulse spectrum; red dotted lines: Brillouin gain spectrum generated by the upper-frequency probe sideband; blue dotted lines: Brillouin loss spectrum generated by the lower-frequency probe sideband; green solid lines: net Brillouin gain spectrum experienced by the pulse; black solid line: output pulse spectrum after SBS interaction.

When the pump-probe frequency offset is chosen to match the dominant BFS of the last fiber section (equal to the non-linear effective length L_{eff}), i.e. $\nu_{offset} = \nu_B$, the amplification and attenuation processes generated, respectively, by the upper and lower frequency sidebands, will occur at the pump frequency simultaneously, as shown in Figure 5.1(a), generating a zero net gain over the pump (green line in Figure 5.1). This leads to an essentially undistorted pulse spectrum along the distance. However, setting the pump-probe offset at a frequency below the BFS [Figure 5.1(b)] ($\nu_{offset} < \nu_B$) implies an amplification curve occurring at a frequency lower

than the pump frequency, and simultaneously, an attenuation process happening at a frequency above the pump frequency (note that the amplification and attenuation processes always manifest at a frequency shifted $\pm\nu_B$ from the corresponding probe frequency). The overall result is that the pump pulse is affected by a non-zero net gain (green line in Figure 5.1) which spectrally down-shifts and distorts the pulse spectrum, in a similar way as the Raman frequency shift of solitons [87]. On the other hand, when the frequency offset is detuned above the BFS [Figure 5.1(c)] ($\nu_{offset} > \nu_B$), the amplification process generated by the upper frequency sideband occurs at a higher frequency than the pump frequency, and equivalently, the attenuation generated by the lower frequency band occurs at a lower frequency than the pump frequency. This will again lead to a distortion of the pulse spectrum and an up-shifting of its central frequency. Thus, sweeping the pump-probe frequency offset around the BFS will modify the pump pulse spectrum, turning it asymmetrical and spectrally shifted upwards or downwards depending on whether the pump-probe frequency offset is higher or lower than the BFS. This has a strong impact on how the gain and loss curves are retrieved, as we will see next.

When performing BOTDA measurements, a frequency sweep around the BFS is needed on the pump-probe frequency offset, in order to recover a complete BFS profile of the fiber. Therefore, changing the pump-probe offset, the Brillouin gain and loss curves interact with a pump pulse spectrum that is spectrally different for each probe frequency, as illustrated in Figure 5.2. In particular, when the offset (ν_{offset}) is detuned below the BFS, the pulse central frequency is down-shifted [see Figure 5.2(a)(top)]. This implies that the new frequency difference among the pump and the upper probe sideband is closer to the BFS (thus, the attenuation is overestimated) and conversely, the frequency difference among the pump and the lower frequency sideband is lower, which implies an underestimation of the gain curve. A similar situation can be observed in the case in which the pump-probe frequency offset is above the BFS [Figure 5.2(a)(bottom)]. In this case the pulse central frequency is up-shifted, which implies that the new frequency difference among the pump and the upper sideband is closer to the BFS. Once again, in this situation, the attenuation is overestimated meanwhile the gain is underestimated.

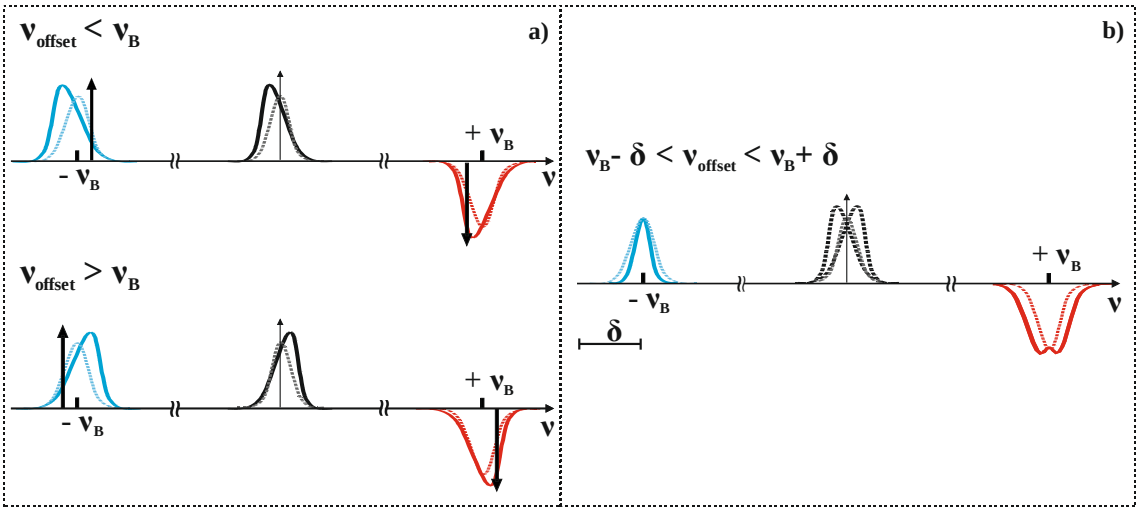

Figure 5.2: a) Illustration of the SBS interaction between a non-uniform pulse spectrum and the Brillouin Gain and Loss curves while sweeping the pump-probe frequency offset (ν_{offset}) for a low-to-medium probe power; b) Resulting spectra after a complete sweep of the pump-probe frequency offset, varying such frequency over a certain amount (± δ) around the BFS of the FUT. The gain process shows an apparent narrowing while the attenuation process appears to be broader.

This particular phenomenon leads to one remarkable result: as the pump pulse advances towards the end of the fiber, the "observed" BGS progressively narrows while the BLS broadens, as observed in Figure 5.2(b). Such outcome will imply, for this low-to-medium probe power regime, a better determination of the BFS in the Brillouin gain case and a worse determination in the Brillouin loss one. Moreover, it can be shown that the energy content of the pulse grows when the modulation frequency is slightly detuned from the BFS. This behavior is responsible for the appearance of two side lobes in the Brillouin loss curve. As we will see, the appearance of undesired lobes is proportional to the probe wave power provided at the fiber end. Such analysis will be complemented with the high-probe power regime study of the forthcoming sections, where massive pump pulse distortions are observed.

Another point of concern for BOTDA developers is that the Brillouin gain and loss processes on the pump induced by, respectively, the upper and lower frequency sidebands of the probe are not exactly located at the same frequency offset from their corresponding sideband. Indeed, the difference in Brillouin shift between the processes generated by the upper and lower sidebands is given by [88]:

$$\nu_B^+ - \nu_B^- = \frac{2nV_A}{\lambda_{US}} - \frac{2nV_A}{\lambda_{LS}} \tag{5.1}$$

Where λ_{US} and λ_{LS} are respectively, the upper and lower frequency sidebands, n is the refractive index of the fiber and V_A is the acoustic velocity in the fiber. A rapid evaluation of this quantity yields a frequency offset between both processes of circa 1.2 MHz in typical conditions. As it will be seeing in the detailed modeling, this induces some asymmetry in the spectral deformation of the pulse described above. In particular, we will see that the BFS estimation tends to be increasingly overestimated as a function of the distance. This effect, although small, is non-negligible.

To model this effect mathematically we will assume that the probe waves experience simple linear attenuation along the fiber. In addition, for now on, we will consider pump pulses with a duration longer than the phonon lifetime (pulse width >> 10 ns). The evolution of pump power with the distance z is then given by [88]:

$$dP_P(\nu,z) = -\alpha P_P(\nu)dz + \left[g_B\left(\nu,\nu_{offset} - \nu_B^+\right) - g_B\left(\nu,\nu_B^- - \nu_{offset}\right)\right] P_s(z) P_P(\nu,z)dz \tag{5.2}$$

where ν is the modulation frequency, α is the attenuation, P_P is the peak pump power and P_S is the probe wave power (where $P_S \equiv P_{US} \equiv P_{LS}$, P_{US} and P_{LS} being the probe power in the upper and lower sideband, respectively). $g_B(\nu,\nu_B)$ is the Lorentzian Brillouin gain profile as a function of the offset frequency ν, given by the following expression:

$$g_B(\nu,\nu_B) = g_0 \frac{(\Delta\nu_B/2)^2}{(\nu-\nu_B)^2 + (\Delta\nu_B/2)^2} \tag{5.3}$$

The pump spectrum as a function of the distance can be solved now [88]:

$$\begin{aligned} P_P(\nu,z)\big|_{\nu_{offset}} &= P_P(\nu,0)\exp(-\alpha z) \\ \times \exp&\left[\left(g_B\left(\nu,\nu_{offset} - \nu_B^+\right) - g_B\left(\nu,\nu_B^- - \nu_{offset}\right)\right) P_s(L)\exp(-\alpha L)\frac{\exp(\alpha z)-1}{\alpha}\right] \end{aligned} \tag{5.4}$$

At each position, the actual gain spectrum observed will be the natural (Lorentzian) gain spectrum convolved with the pump spectrum:

$$g(\nu,z)\Big|_{\nu_{offset}} = g_B(\nu,\nu_B) \otimes P_P(\nu,z)\Big|_{\nu_{offset}} \tag{5.5}$$

For each probe frequency, this spectrum is read at the corresponding pump-probe frequency offset ($\nu = \nu_{offset}$), and thus, evaluating the gain spectrum obtained in Eq. (5.5) for $\nu = \nu_{offset}$. Correspondingly, the same process is followed to compute the loss spectrum and the recovered BLS value at $\nu = -\nu_{offset}$. Note that each frequency offset detuning yields a different pump deformation, and therefore the read gain/loss value has to be recalculated for each case.

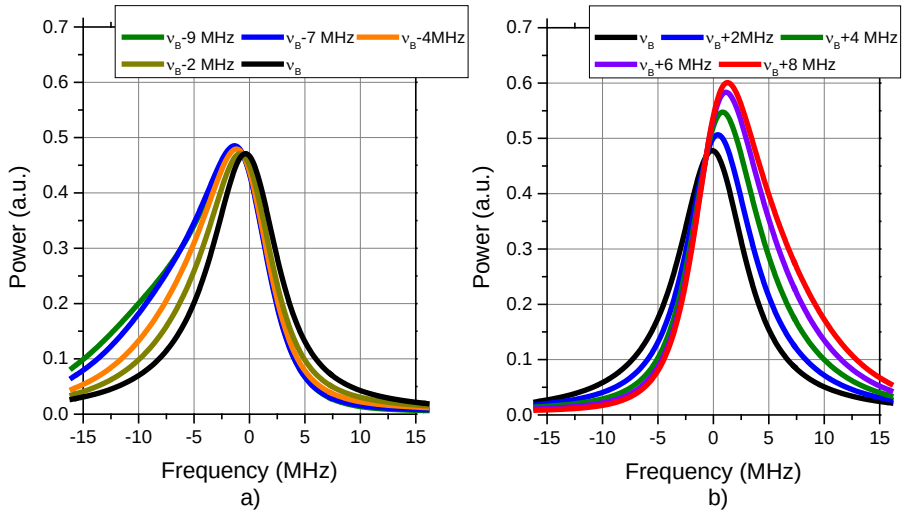

Figure 5.3: Pump pulse theoretical spectra after going through the fiber and interacting with a probe wave whose frequency is detuned around the BFS of the FUT. a) Sweeping frequency below the BFS; b) Sweeping frequency above the BFS [88].

To further clarify such phenomenon, an illustration of the pulse shifting and asymmetrization process is shown in Figure 5.3 for different values of $\nu = \nu_{offset}$. The frequency displacement and the spectral disproportion turns out to be non-negligible when sweeping the frequency offset around the BFS of the fiber.

Furthermore, a simulation of the interaction between a spectrally non-uniform pump pulse and a pump-probe frequency offset varying around the BFS has been carried out. Figure 5.4 illustrates the calculated BGS and BLS at the end of the fiber, where the BLS starts to show two undesired side lobes around the center frequency of the curve meanwhile the BGS remains well-proportioned and similar to the expected value. Besides such disproportion, the BGS presents a narrower profile than the BLS, which could lead to a better determination of the

BFS extracted from the BGS compared to the BLS case. Moreover, both gain and loss curves are slightly up-shifted in comparison with the expected curve for the BFS at that position. This shift is usually in the order of 1 MHz or below 1 MHz, so comparable to the usual values of uncertainty. These consequences, among others, will be studied in further detail in the forthcoming sections.

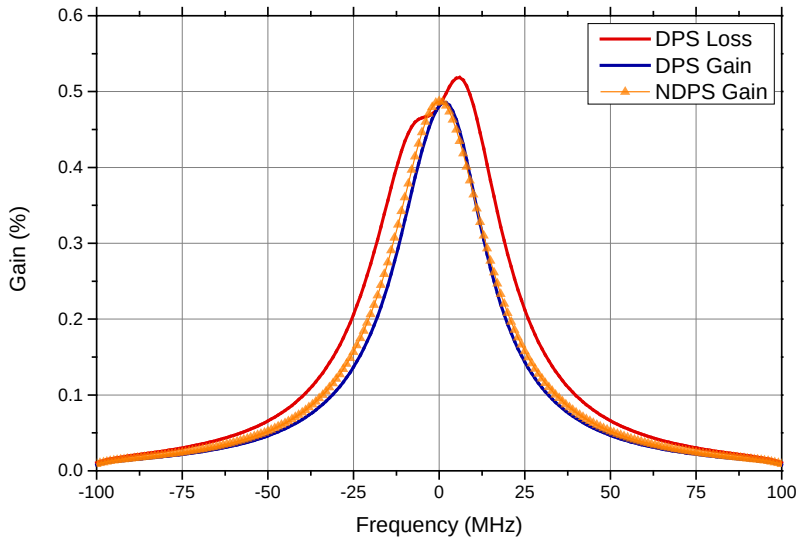

Figure 5.4: Simulated BGS and BLS retrieved for a distorted pulse spectrum (DPS) overlapped with the simulated BGS for a non-distorted pulse spectrum (NDPS) at the end of the FUT for a pump pulse peak power of ~57 mW and a probe wave power of ~275 μW (on each sideband). Simulations obtained for a Gaussian pump pulse of 10 MHz of width [88].

5.2.1 Experimental Results

To prove the above model of non-local effects in DSB-BOTDA systems for low-to-medium probe powers, the BOTDA scheme represented in Figure 5.5 has been developed. It is a variation of the already implemented DSB-BOTDA system (see Figure 4.2) where the pump pulse is shaped using an Electro-Optical Modulator (EOM) and where the detection is done by means of a conventional single-sideband detection scheme.

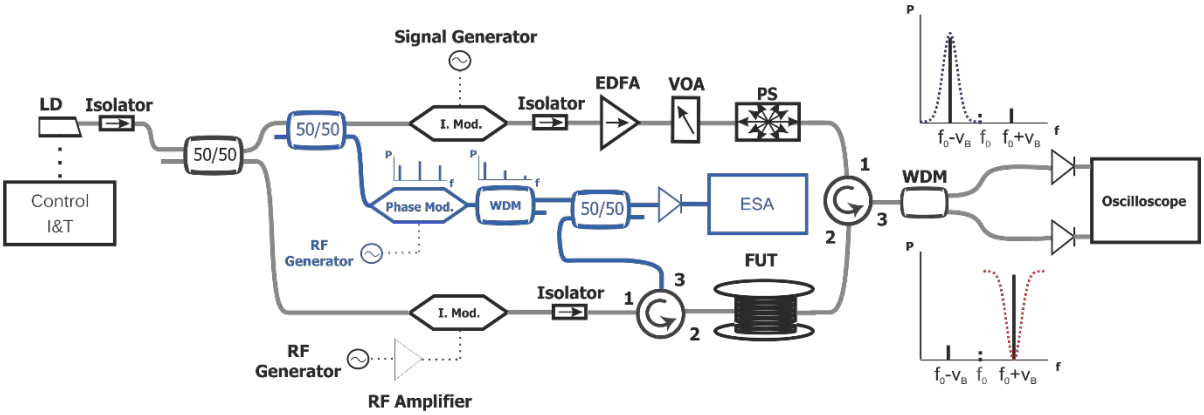

Figure 5.5: BOTDA experimental setup. LD: Laser Diode; I. Mod.: Intensity Modulator; EDFA: Erbium Doped Fiber Amplifier; RF: Radio-frequency generator; VOA: Variable Optical Attenuator; PS: Polarization Scrambler; FUT: Fiber Under Test; WDM: Wavelength Division Multiplexer; ESA: Electrical Spectrum Analyzer [88].

Analogously to what it has been presented in the previous chapter, and as in most BOTDA setups, pump and probe waves are developed from a single distributed feed-back (DFB) laser diode [24]. A Mach-Zehnder EOM is used to make a dual sideband with suppressed carrier (DSB-SC) modulation in the probe. The extinction ratio of the EOM is >40 dB, thus it is possible to nearly eliminate the carrier signal. The probe power fed into the fiber is ~500 μW (-3 dBm) on each sideband. The modulation frequency of the EOM is controlled through an RF Generator. The RF frequency is chosen to sweep around the BFS of the FUT.

At the pump side, the signal is pulsed using another EOM. The EOM allows to shape high extinction ratio (~30 dB) optical pulses. The pulse widths used in the experiment are 50 ns, which implies a 5 meter spatial resolution. The pulses are then amplified through an EDFA, and their power is controlled through a Variable Optical Attenuator (VOA). After the VOA, their polarization is scrambled by a fast polarization scrambler. The peak power of the pulses fed into the fiber is ~50 mW.

After going through the fiber and experiencing Brillouin scattering, the probe sidebands are separated using a conventional 100 GHz DWDM filter. The edge of the filter used is sharp enough to separate both sidebands correctly, attenuating the rejected band in >13 dB. The Brillouin gain and loss bands are then fed into two equal photodetectors, so as to acquire both signals simultaneously.

In addition, in order to check the spectral evolution of the pump pulse along the fiber, an extra setup has been incorporated in order to measure the pulse spectrum through heterodyne detection. First of all, the master laser is split using a 50/50 coupler. While one of the arms is used to shape the pump, the other is phase-modulated by means of an electro-optical phase modulator at a certain RF frequency, which is set by means of an external RF generator. The lower sideband of the resulting modulated wave is selected by means of a DWDM filter. An optical circulator is placed at the end of the FUT, on the probe side, so the pulse can be properly recovered after interacting with the probe sidebands through SBS. This pulse is then recombined with the selected sideband of the phase modulation, and the resulting combination is fed into a high bandwidth photodetector. This allows us to observe the pulse spectral shifting/deformation with high spectral resolution and capability to discriminate the sense of the frequency shifts.

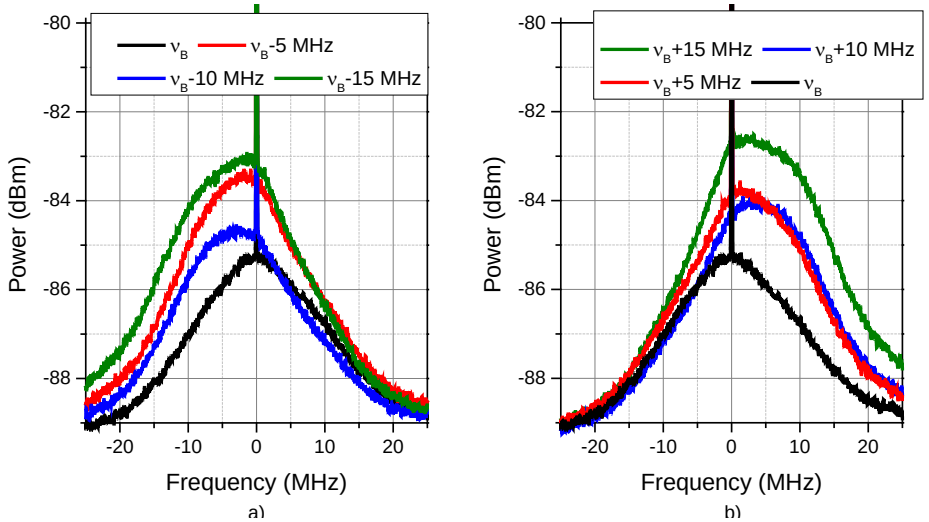

Figure 5.6: Electrical spectra (75 kHz of resolution bandwidth) of the detected pump pulse recorded after going through the FUT and experiencing SBS for a fixed probe wave power of ~500 μW (-3 dBm) per sideband, sweeping the pump-probe frequency offset around the BFS of the FUT; a) Sweeping frequency below the BFS; b) Sweeping frequency above the BFS. The vertical lines located at 0 MHz in the spectra correspond to the DC leakage of the pump pulse [88].

Making use of the above explained scheme, full BOTDA measurements have been performed over ~50 km of single-mode fiber (SMF) with an essentially homogeneous BFS located at 10.865 GHz at the pump wavelength (~1550 nm). The acquired traces have always

been averaged 1024 times. The first remarkable result is the observation of an asymmetric spectral shift of the pump pulse dependent on the pump-probe frequency detuning. Figure 5.6 shows the evolution of the electrical spectrum of the pump pulse after experiencing SBS through the fiber. A 32 GHz bandwidth Electrical Spectrum Analyzer (ESA) has been used to acquire the pulse spectrum for a fixed probe power and different pump-probe frequency offsets. As it can be seen (and as previously modelled), the interaction of both the attenuation and amplification processes with the pulse modifies its spectral shape, leading to an upshifting of the pulse when the pump-probe frequency is detuned above ν_B and a down shifting when it is detuned below the BFS. Moreover, the separation from the BFS frequency also leads to an increase in the pulse energy content, which is larger when the frequency detuning is above the BFS. As previously discussed, the slight offset among BFSs generated by the upper and lower modulation bands unbalances the power provided for a fixed pump-probe frequency detuning.

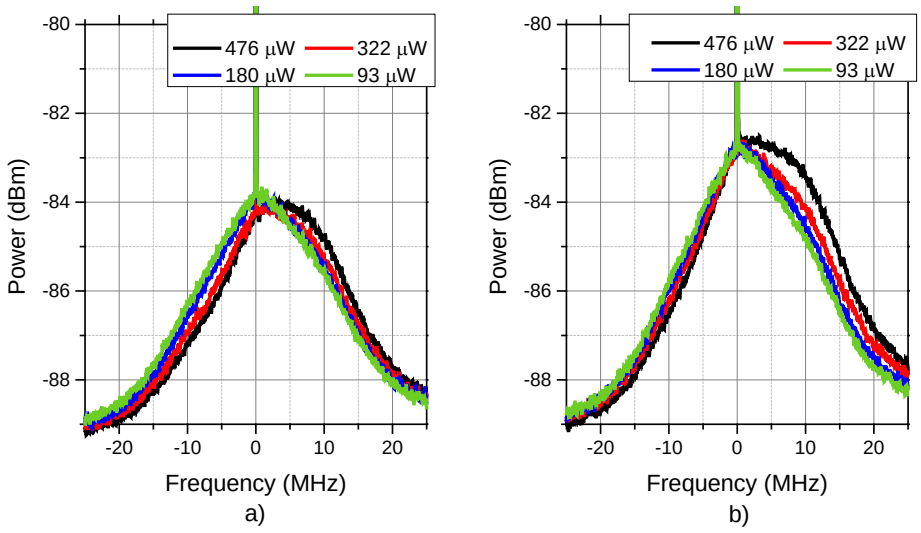

Figure 5.7: Electrical spectra (75 kHz of resolution bandwidth) of the detected pump pulse recorded after going through the FUT and experiencing. a) Probe power variation for a fixed probe wave modulation frequency of 10.873 GHz (ν_B + 5 MHz). b) Probe power variation for a fixed probe wave modulation frequency of 10.873 GHz (ν_B + 10 MHz). Again, the vertical lines located at 0 MHz in the spectra correspond to the DC leakage of the pump pulse [88].

In Figure 5.7, the same analysis has been carried out varying the probe power delivered into the fiber for a fixed pump-probe detuning. Such analysis illustrates that the more powerful

the probe wave is, the more asymmetrical the pulse shape becomes. It can be observed that even for the less powerful case, the pulse spectrum remains slightly asymmetrical.

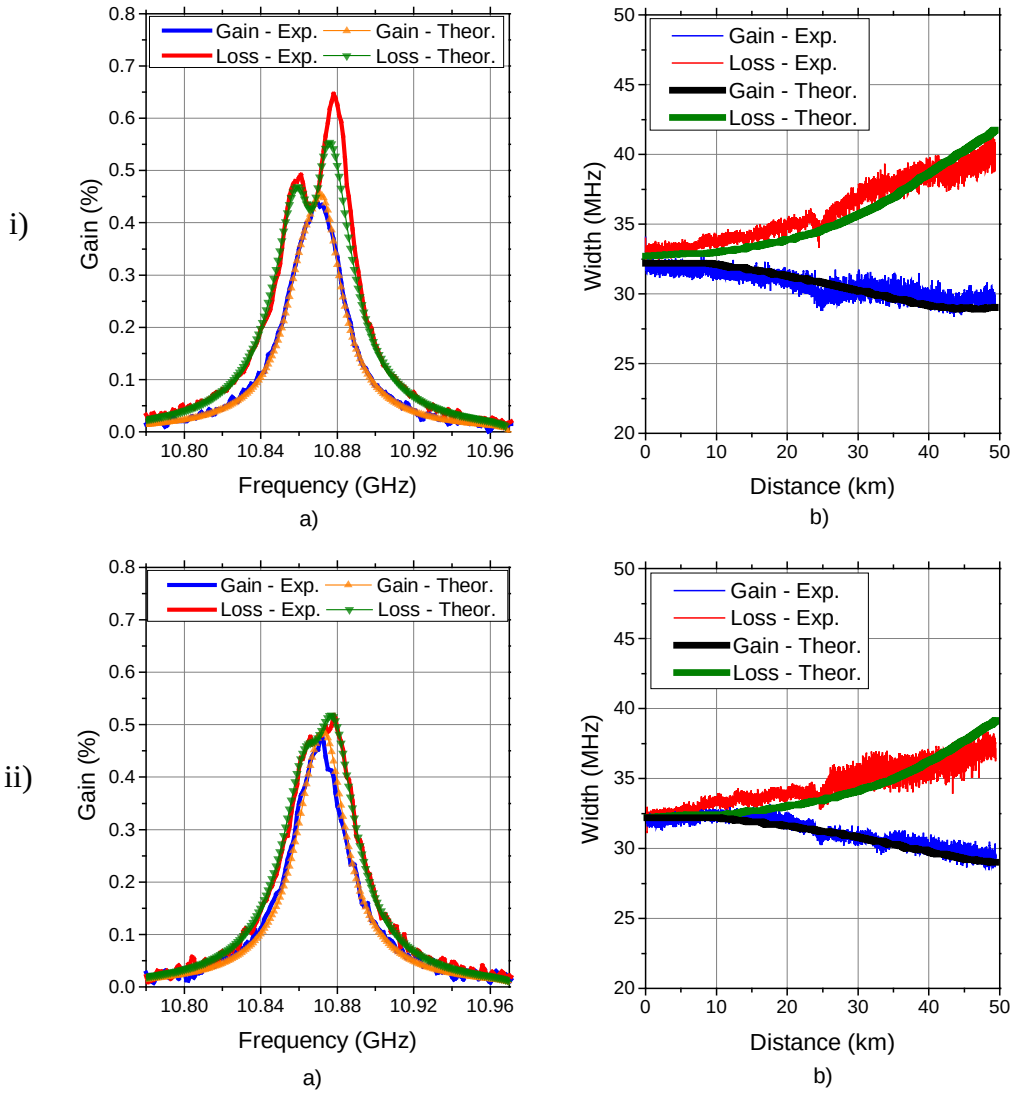

Figure 5.8: BOTDA outcomes for a probe wave power of: i) ~500 μW (- 3 dBm) per sideband, and ii) ~275 μW (- 5 dBm) per sideband. a) Experimental and theoretical representation of the BGS and BLS at 49.768 km for a frequency sweep between 10.78 GHz and 10.98 GHz. b) Experimental and theoretical evolution of the FWHM for the Brillouin gain and loss spectra [88].

As previously pointed out, such remarkable phenomenon leads to a major outcome: it broadens and distorts the BLS profile meanwhile narrows the BGS. Figure 5.8 shows the theoretical and experimental BLS and BGS analysis for two different probe wave powers:

~500 μW (- 3dBm) and ~275 μW (- 5dBm) per sideband [Figure 5.8(i) and Figure 5.8(ii) respectively]. Figure 5.8(a) graphs represent both the BGS and BLS at a distance of 49.768 km; Figure 5.8(b) graphs, though, illustrate the evolution of the FWHM of the BGS and BLS profiles along the distance. As it can be seen in Figure 5.8(i)(b), the FWHM of the experimental BLS broadens ~7.5 MHz, meanwhile the simulated results show a broadening of ~8.5 MHz. Conversely, the FWHM of the BGS narrows ~3 MHz, confirming the decrease of ~3 MHz observed at the simulated results. In Figure 5.8(i)(a), it can be observed the gain and loss spectra for a probe power of ~500 μW (-3 dBm) per sideband at the very end of the FUT (point 49.768 km). The measured distorted BLS and BGS curves are well recovered by the model, as we can see. The spurious new lobes retrieved on the BLS are, in fact, as predicted, slightly unbalanced among each other due to the small BFS offset generated by the Brillouin gain and loss bands. In this case, the theoretical model adjusts correctly to the experimental result, following reliably the profile shape.

The same analysis has been carried out reducing the probe wave power down to ~275 μW (-5.6 dBm) per sideband. As Figure 5.8(ii)(a) illustrates, the disproportion and the spurious side lobes in the BGS and BLS have decreased when reducing the probe power. Such outcome confirms the theoretical analysis previously studied (the experimental data profiles follow precisely the theoretical curves). The FWHM of the BGS continues to be narrower than the BLS one. Analyzing the evolution of the FWHM of both the BGS and BLS along the fiber Figure 5.8(ii)(b), the FWHM of the BLS tends to be wider at the end of the fiber meanwhile the width of the BGS narrows towards the end of it. In particular, the FWHM of the experimental BLS broadens ~5 MHz, meanwhile the simulated results show a broadening of ~7 MHz. On the other hand, the FWHM of the BGS narrows ~3 MHz, once again, verifying the ~3 MHz decrease observed at the simulated results.

On top of the above results, the consequences of these non-local effects in terms of the BFS determination have been investigated. As it has already been shown, the BLS at the very end of the fiber presents two asymmetric side lobes [see Figure 5.8(i)(a)]. Indeed, due to the small mismatch of the BFS generated by the Brillouin gain and loss bands, such spurious peaks are unequal, and the higher frequency lobe always prevails over the lower frequency one. The

appearance of these lobes can lead to a distorted determination of the maximum of the retrieved curves, which should be consistently overestimated.

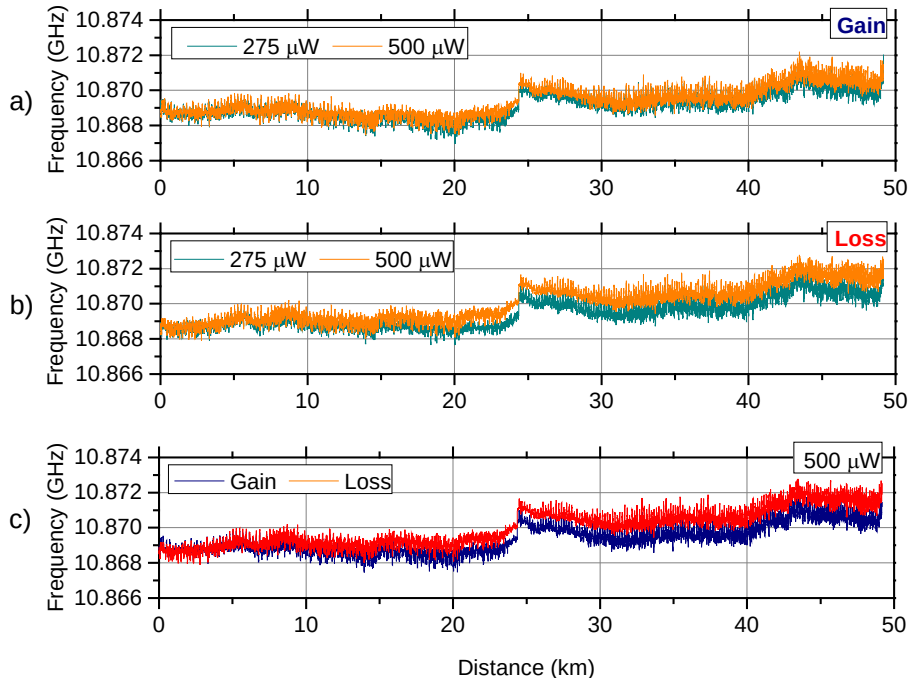

Figure 5.9: Brillouin frequency shift profiles obtained for different probe wave powers on a ~50 km SMF. a) BFS profiles obtained from the measured Brillouin gain band for two values of probe power; b) BFS profiles obtained from the measured Brillouin loss band for two values of probe power; c) BFS profiles of the Brilluoin gain and loss bands for a fixed probe wave power of ~500 μW (-3 dBm) per sideband [88].

The analysis of the mismatch in the determination of the BFS along the fiber when increasing the probe power (i.e. increasing the asymmetry in the side lobes) is shown in Figure 5.9. The BFS profile of the Brillouin gain spectrum along the fiber for two different probe wave powers is illustrated in [Figure 5.9(a)]. Increasing the probe wave power leads to a BFS displaced an average of ~0.6 MHz to higher frequencies at the very end of the fiber. On the contrary, the BFS obtained from the Brillouin loss spectrum [Figure 5.9(b)] shifts ~1 MHz to higher frequencies when strengthening the asymmetry of the pump pulse spectrum. Furthermore, the behavior of the BFS obtained for both the BGS and BLS for a fixed probe wave power [Figure 5.9(c)] has also been studied. The displacement of the BFS extracted from the measured loss curve at the very end of the fiber is again ~1 MHz above the BFS obtained

in the gain case, whereas the BFS measured for both cases at the beginning of the FUT remains equal. These results clearly confirm the slight up-shifting phenomenon of the BFS predicted by the qualitative models, which is stronger in the attenuation case.

5.3. High Probe Power Regime

The previous section studies, both theoretical and experimentally, the consequences of the conventional scanning of the pump-probe frequency offset in DSB-BOTDA schemes for probe powers up to -3 dBm/sideband. The distortions induced on the pump pulse lead to major deformations on the retrieved BGS and BLS, which ultimately affect the BFS determination. For this probe power regime, the detrimental effects prevail in the Brillouin loss configuration case over the gain one. All of these effects, both in gain and loss configurations, are already of great importance for BOTDA manufacturers.

As already known, the major limitation in mid-to-long range BOTDA sensors is the low SNR at the far end of the fiber. To overcome such limitation, several advanced approaches have been put forward in the literature [54]–[56], [65], [73], [89], [90], allowing a significant boost in SNR and sensor performance; however, their capability to enable implementations with very high figure-of-merit [32] has been compromised by the use of low probe power levels, thus preventing those advanced techniques from performing at their maximum potential.

The present section aims to understand the effect of applying strong probe powers (i.e. above -3 dBm/sideband) to DSB schemes, where massive pump pulse distortions are reported. In this case, not only the spectral distortions but also the temporal perturbations are thoroughly studied, where the spatial resolution becomes dramatically affected, and where any BFS change is completely concealed towards the far end of the fiber.

5.3.1 Spectral and Temporal Pump Distortion

As previously mentioned, it has been shown that the pulse spectrum experiences distortion and a spectral up or down-shifting when sweeping the pump-probe frequency offset in the conventional scanning process of BOTDA sensors. Such pulse distortion entails a non-negligible deformation over the Brillouin gain and loss curves retrieved at the far end of the fiber, consequently affecting the BFS determination. In this section, those previous findings are complemented and more deeply investigated in a much larger probe power range, including also an investigation on the temporal distortion of the pulse shape for different pulse lengths and different frequency detuning. For this analysis, a conventional BOTDA scheme based on a two-sideband probe has been used (see Figure 5.5) [26], [86], [91]. Scanning the pump-probe frequency offset around the BFS of a 50 km-long single-mode fiber, and using a 20 ns pulse for 2 m spatial resolution, the BGS and BLS have been measured for different probe power levels (a peak pump power of 80 mW has been used in all measurements). Figure 5.10 shows the measured BGS (blue curves) and BLS (red curves) obtained at the end of the sensing fiber (at 50 km distance), for a probe power per sideband of (a) –5 dBm, (b) –2 dBm, (c) +1 dBm and (d) +4 dBm. Experimental results point out that, for –5 dBm probe power, although there appear minimum distortions in the measured spectra, such distortions are negligible, while with the use of moderate probe powers the spectral distortion becomes evident. Actually, the narrowing effect observed in the gain spectrum and the broadening measured in the loss spectrum for –5 dBm and –2 dBm [see Figure 5.10(a)-(b)] match the behavior reported in Section 5.2. However, a novel and unexpected behavior could be found with powers reaching and exceeding the mW range: for such a high probe power (e.g. more than about 0 dBm), both the BGS and BLS show a peak splitting around the BFS.

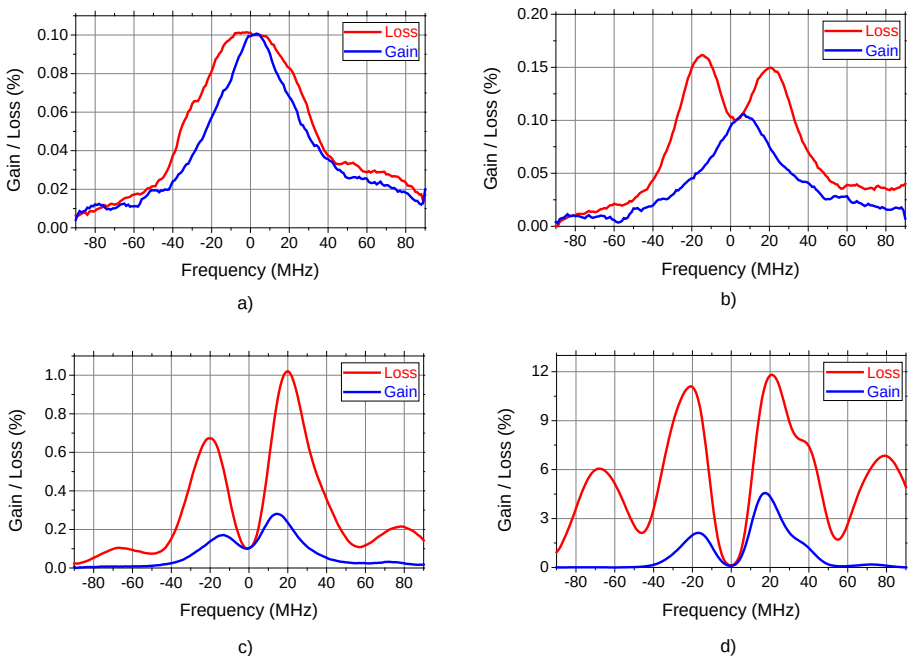

Figure 5.10: Measured BGS/BLS at the end of a 50 km SMF using a conventional BOTDA sensor with 2 m spatial resolution, for different probe power levels: (a) –5 dBm/sideband; (b) –2 dBm/sideband; (c) 1 dBm/sideband; and (d) 4 dBm/sideband. Red curve: BLS; blue curve: BGS. Spectral distortions originate from the asymmetric Brillouin gain and loss process affecting the pump pulse while scanning the pump-probe frequency offset around the BFS [92].

In order to have a better insight into the process and to provide an explanation of the spectral distortions shown in Figure 5.10, Figure 5.11 show a schematic description of the pump-probe Brillouin interaction occurring in a standard DSB-based scanning method for the present probe power regime. By sweeping the frequency of the two sidebands in the traditional way [18], [26], [88], [91], [93], as shown in Figure 5.1, the pump pulse spectrum is subject to an uneven spectral compensation of the gain-loss probe spectra when detuning them. The pulse spectrum turns out to be then asymmetrically distorted and downshifted or upshifted as the pulse propagates along the sensing fiber, depending on whether the scanned pump-probe frequency offset (ν_{offset}) is higher or lower than the dominant BFS of the fiber [88]. This detrimental effect comes from the non-zero net gain (indicated by green lines in Figure 5.1) over the pump that combines Brillouin gain and loss spectra generated by the upper and lower probe sidebands, respectively.

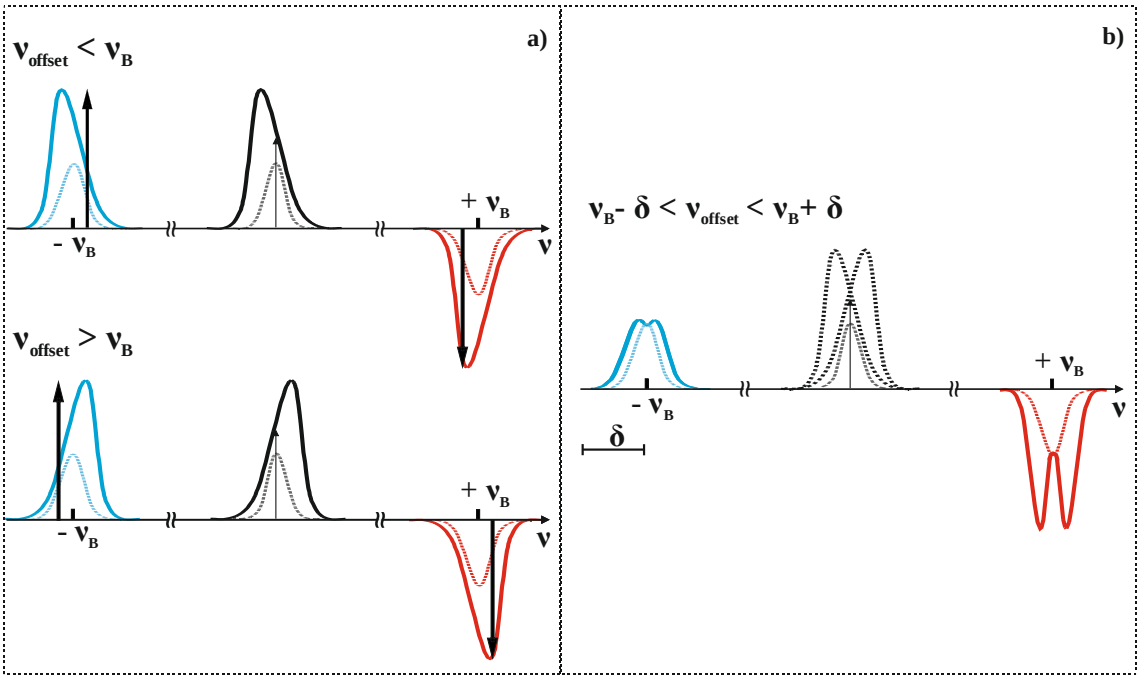

Figure 5.11: a) Illustration of the SBS interaction between a non-uniform pulse spectrum and the Brillouin Gain and Loss curves while sweeping the pump-probe frequency offset (ν_{offset}) for a high probe power; b) Resulting spectra after a complete sweep of the pump-probe frequency offset, varying such frequency over a certain amount ($\pm \delta$) around the BFS of the FUT. In this case, both the gain and loss processes present a double peak around the maximum of the curve, as well as a notorious broadening.

The higher power regime occurs at probe powers ranging from about 0 dBm up to the threshold of ASpBS (about +7 dBm). In this case, the pump-probe interaction is similar to the previous case presented in Section 5.2 for lower powers (see Figure 5.2); however, the net asymmetric Brillouin gain (see green line in Figure 5.1) amplifying and distorting the pump pulses highly cumulates along the fiber, increasing with a strong nonlinear dependency on the probe power. This leads to BGS and BLS having two strong peaks around the central BFS (see Figure 5.11), as demonstrated in the measurements previously shown in Figure 5.10(c)-(d). An interesting feature is that for such high-power regime, the induced detrimental effects grow exponentially with the probe power, which can dramatically worsen the system performance. This is a completely different behavior when compared to results reported in Section 5.2, and it has a more detrimental impact on the measurements since the obtained spectrum splits into side-lobes independently of the measured processes (i.e. it occurs for both the BGS and BLS).

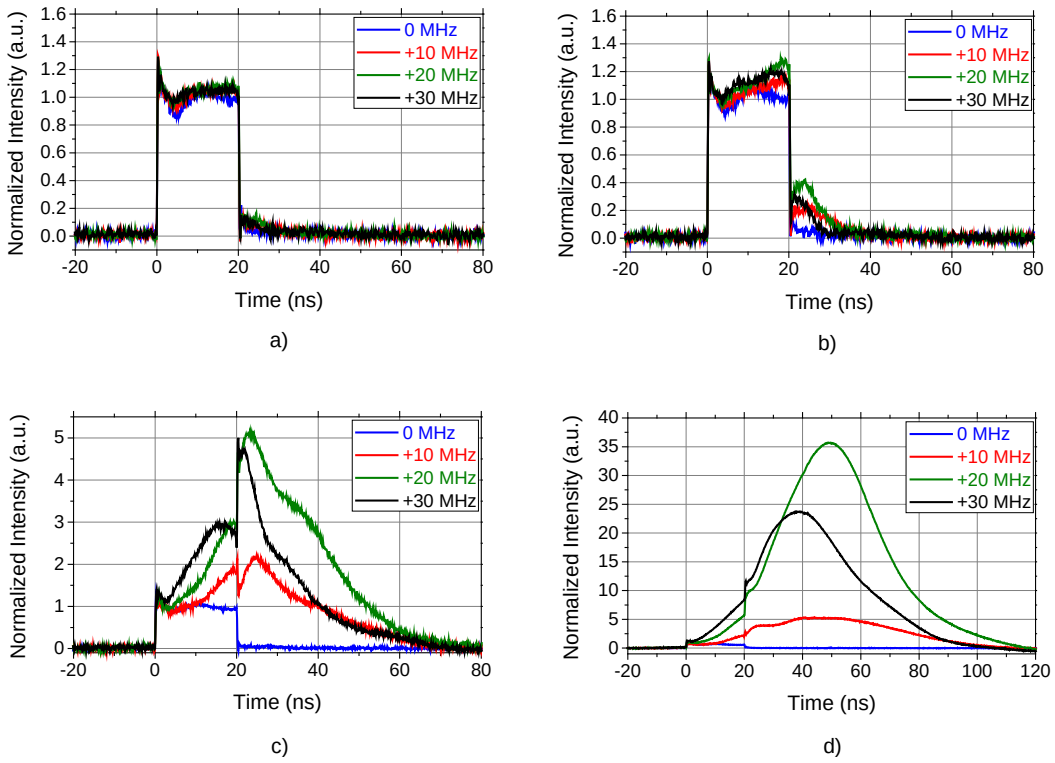

Figure 5.12: Temporal distortion of a 20 ns pump pulse, for different pump-probe positive frequency detuning and using probe powers of (a) –5 dBm/sideband; (b) –2 dBm/sideband; (c) 1 dBm/sideband; and (d) 4 dBm/sideband [92].

In addition to the above-reported spectral distortions, the pump pulses also experience significant temporal deformation after interacting with the two-sideband probe through long sensing fibers. Figure 5.12 shows a set of measurements analyzing the deformation of the pulse temporal shape at the output of the 50 km sensing fiber for different probe powers, when detuning the pump-probe frequency offset around the BFS. Actually, when the pump-probe frequency offset matches the BFS of the fiber, gain and loss induced by the sidebands on the pump pulse compensate, and there is no distortion, broadening or amplification on the pump pulse shape. However, as shown in Figure 5.12, when the pump-probe frequency offset is detuned from the BFS of the fiber (positive detuning), the asymmetric non-zero net gain affecting the pump pulses induces huge temporal distortions, which manifest as large temporal broadening and amplification. Although a negligible tail could be observed in the pulse for low probe powers [Figure 5.12(a)-(b)], the final pulse shape results completely distorted when using high probe powers [Figure 5.12(c)-(d)]. The largest distortion in this case has been found

to be for a frequency detuning of about 20 MHz; however, this worst-case condition depends on the pulse spectral width, which is directly linked to its temporal duration. It is noteworthy the huge amplification and temporal broadening induced when using a probe power of +4 dBm/sideband, resulting in a pulse shape with 30 times higher power and about 4 times longer (i.e. a net energy growth up to 120 times higher than the undistorted pulse energy). Considering that the local Brillouin gain/loss measured by a BOTDA sensor depends on the local energy of the pump pulse (see Section 3.2), temporal and amplitude distortions have both a relevant impact on the measured BGS/BLS. The large distortions in the measured BGS and BLS shown in Figure 5.10(d) actually originate from the very high local energy transfer from the pulse to the probe occurring at such a high probe power (4 dBm).

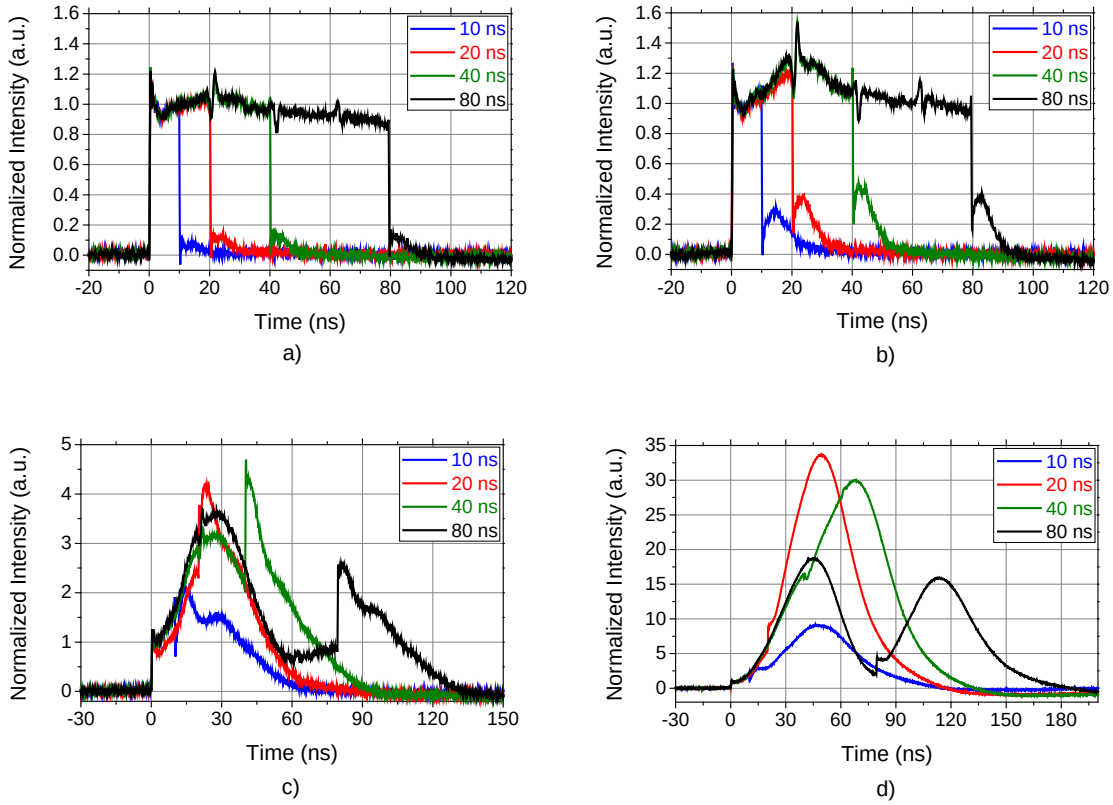

Figure 5.13: Temporal distortion of pump pulses having different widths, for a fixed pump-probe frequency detuning equal to ν_B + 20 MHz, when using a probe power of (a) –5 dBm/sideband; (b) –2 dBm/sideband; (c) 1 dBm/sideband; and (d) 4 dBm/sideband [92].

An important consequence of the non-local effects induced in this case is not only linked to the spectral distortions affecting the measurements, but also to the huge temporal distortion

of the pump pulse, which obviously has a deleterious effect on the spatial resolution of the system.

In addition to the impact of the frequency detuning, the pulse distortion has also been investigated for different pulse widths. Figure 5.13 shows the pulse temporal shape measured for four different pulse widths, using the same previous four probe powers (ranging from -5 dBm to +4 dBm). Similarly to the behavior reported in Figure 5.12, Figure 5.13 also points out that the pulse distortion is actually negligible when operating at a probe power of -5 dBm, or below; however, this rapidly grows when the probe power is increased. In addition, Figure 5.13 also indicates that the level of distortion highly depends on the pulse width, which is clearly explained by the differences in the spectral width of the pulse interacting with the two probe sidebands. A visual inspection of the figure actually indicates that the higher amplitude distortion occurs for a 20 ns pulse width; however the real impact on the sensor response depends not only on the amplitude distortion but on the total relative energy growth that pump pulses experience.

In order to fairly quantify the impact that the described distortions have on the sensor response, the total energy contained in the pump pulse has been calculated by simple integration of the temporal shapes above reported. Figure 5.14 illustrates the integrated energy of the pump pulses measured at the fiber end (50 km) for different pump-probe frequency detuning and several pulse widths. The energy shown in the figure has been normalized by the energy of the undistorted pulses obtained after propagation along the fiber and in absence of Brillouin interaction. As it can be seen, for low probe powers (< –5 dBm) the pulse distortion represents less than 10% of the energy carried by the pulse, regardless the frequency detuning and pulse width. As shown before in Figure 5.10, this relative energy variation can be considered low enough to prevent the measured BGS/BLS from being distorted. When the probe power is increased up to –2 dBm, a certain and repeatable distortion pattern appears, inducing a maximum distortion of about 25% at a frequency detuning of ~20 MHz. For higher probe powers, the distortion strongly increases, well above the reference pulse energy, reaching levels of up to 170 times larger than the undistorted pulse case. Comparing the results in Figure 5.14(c) and Figure 5.14(d), it is actually possible to observe the highly non-linear growth of the detrimental effects, where the pulse energy distortion grows about ~20 times for a probe

power increase of just 3 dB. It is worth noticing that the relative energy distortion here reported clearly highlights the fact that larger relative distortions occur when using shorter pump pulses. This can be explained by the broader spectrum characterizing shorter pulses, which turns out to be much more affected by the asymmetric gain-loss process generated by the two probe sidebands when scanning the BGS/BLS. Figure 5.14 also points out that the shorter the pulse width, the higher the detuning frequency at which these phenomena have a more harmful effect, e.g. being ~20 MHz for a 20 ns pulse width, but ~25 MHz for a 10 ns pulse. Thus, analyzing the entire set of measurements in Figure 5.14, it can be generally stated that the worst distortion scenario arises in BOTDA sensors having a spatial resolution of 1-2 m (i.e. using pulses of 10-20 ns), especially when scanning frequency offsets close to ~20-25 MHz.

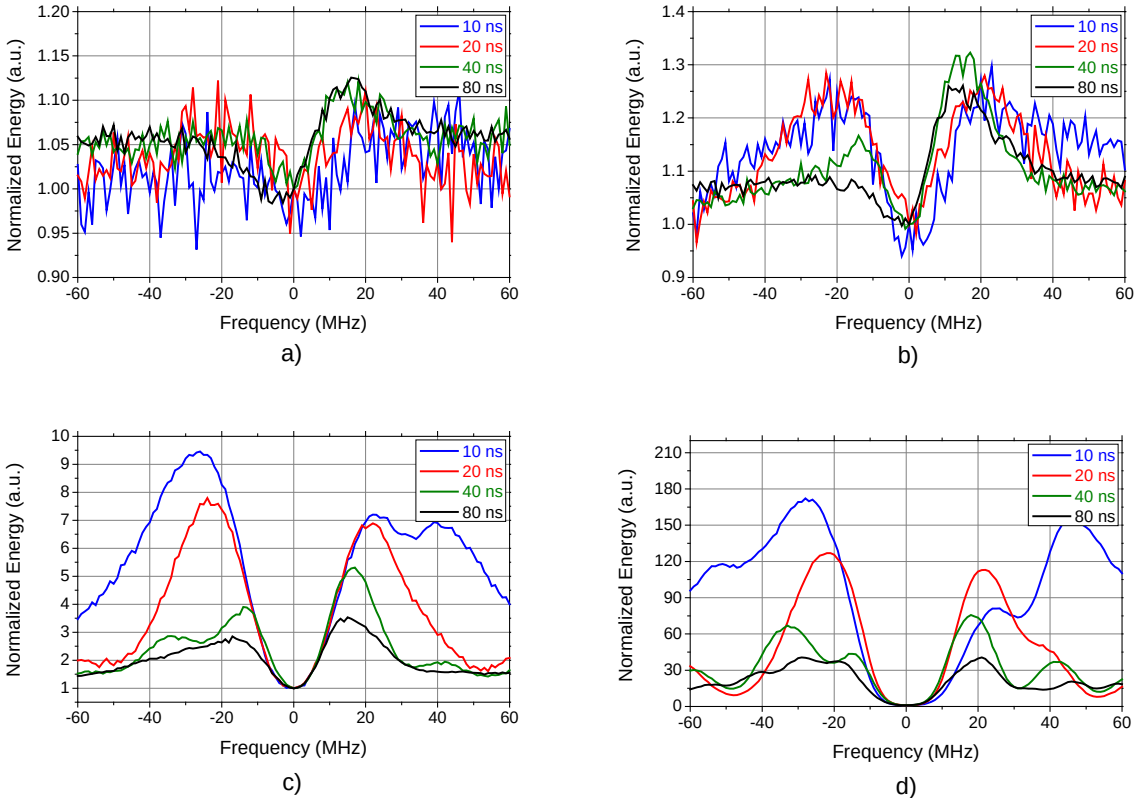

Figure 5.14: Total (integrated) pulse energy obtained from the optical pulses measured at the fiber output (after 50 km distance) and normalized by the undistorted pulse energy. Curves are plotted versus the detuning between the pump-probe frequency offset and the dominant BFS of the fiber, for different pulse widths and a using a probe power equal to (a) –5 dBm/sideband; (b) –2 dBm/sideband; (c) 1 dBm/sideband; and (d) 4 dBm/sideband [92].

It should be mentioned that the leading distortions induced on the pump pulse in both probe power regimes are certainly caused by the SBS interaction between the pump pulse and the probe sidebands (as depicted in Figure 5.2 and Figure 5.11). However, it is clear that other non-linearities (such as modulation instability or ASpBS) may arise in the higher probe power regime as a result of the huge variation of the pump pulse energy. It has been checked that these non-linearities have no major effect on the pulse shape, but may eventually lead to additional deformations of the measured BOTDA trace.

5.4. Conclusions

In this chapter, a thorough analysis of non-local effects impacting on the response of conventional BOTDA sensors based on high-power DSB probe has been presented. Experimental results have verified that, contrary to the common acceptation up to now, non-local effects do appear in conventional dual-sideband BOTDA schemes well below the ASpBS threshold, especially when using long fiber sections showing uniform BFS. The DSB scheme actually works perfectly when the modulation frequency matches the BFS of the fiber, but suffers from non-local effects when the sideband modulation frequency is detuned from the dominant BFS of the fiber. The analysis presented here highlights that the origin of these non-local effects is the uneven spectral compensation of the gain and loss spectra caused by the probe sidebands on the pump pulse spectrum. The pump pulse changes severely its spectral shape when it propagates through a long sensing fiber and interacts with a high-power probe wave. These spectral changes manifest as a shift and an asymmetric energy growth of the pump spectrum depending on the exact detuning from the BFS. Such an asymmetry is directly related to the probe power employed, being larger for higher probe powers. They are also related to the pulse width, so they become more severe when the pulse is shorter (in higher-resolution systems). In addition, measurements have also demonstrated that these spectral distortions turn out to induce strong temporal distortions in the pump pulses at the fiber end, affecting the accuracy and spatial resolution of the measurements. Additionally, in the forthcoming Chapter, where a solution to avoid these effects is presented, it has been actually verified that the combination of these detrimental effects conceals the determination of temperature or strain

events in the fiber (see Figure 6.5), especially at the end of long sensing fibers, as the measured gain and loss spectra turn out to be completely distorted, typically showing two side-lobes detuned from the BFS frequency.

Chapter 6:
Novel Scanning Method for Distortion-free BOTDA Measurements

6.1. Introduction

The DSB-BOTDA scheme works perfectly when gain/loss spectra generated by the probe-sidebands are fully overlapping. However, as it has been shown in the previous Chapter, such a scheme still suffers from non-local effects when probe and gain spectra are detuned, even for probe powers far below the ASpBS threshold. Since the asymmetric gain/loss process affecting the pump pulse cumulates along the sensing fiber, severe distortions in the gain/loss BOTDA traces are obtained, particularly towards the end of the fiber, where the probe power is the highest. This gives rise to errors in the BFS estimation, and imposes serious limitations to the performance of conventional BOTDA sensors in long-range scenarios. Hence, it turns necessary to devise a clever procedure to resolve such limitations in BOTDA sensors. This chapter presents a novel scanning technique that smartly overcomes the restrictions imposed by the appearance of detrimental non-local effects induced by the probe, allowing a significant

increase of the used probe power, and consequently, considerably augmenting the system SNR. Such interesting feature has led to two major state-of-the-art records: first, a BOTDA sensor that reaches 100 km with a 2 m spatial resolution has been achieved, without using any kind of amplification, coding or post-processing technique, and in a conventional acquisition time; furthermore, a sensor that resolves, for the first time to our knowledge, 1,000,000 sensing points in a time-domain Brillouin sensor, featuring 1 cm of spatial resolution over 10 km of SMF. The acquisition time in this case is kept under a few minutes, which means a one order of magnitude reduction when compared to other methods for an equivalent performance.

6.2. Novel BOTDA Scanning Method

In order to overcome all the previously mentioned limitations and avoid the distortions affecting the system, a new scanning method is here proposed. In this case, instead of sweeping the two probe sidebands symmetrically away and towards the pulse spectrum as in the conventional case [18], [26], [88], [91], [93], the proposed scheme keeps a fixed frequency separation between the two probe sidebands (equal to twice the dominant BFS of the fiber) while sweeping pump or probe wave frequency to scan the Brillouin gain or loss spectrum, as shown in Figure 6.1. Compared to the conventional scanning method explained in previous chapters, (see Figure 5.1), in the technique here proposed (Figure 6.1), the optical pump frequency remains fixed, while the probe sidebands scan towards higher or lower frequencies in unison, keeping a constant separation between them ($2\nu_B$). This way, the gain and loss spectra generated by the two probe sidebands exactly cover the same spectral region and mutually cancel out, regardless of the scanned pump-probe frequency offset (ν_{offset}). Consequently, the pump pulse experiences no spectral distortions during propagation and Brillouin interaction. As demonstrated in the next section, this proposed technique allows the probe power to reach the ultimate limit given by the ASpBS threshold, representing about 12 dB enhancement on probe power when compared to the traditional dual-sideband probe configuration. It must be mentioned that the compensation is fully effective only in the small

gain regime – which is confidently the case of BOTDA systems at <5 m spatial resolutions – and with probe sidebands of equal amplitude.

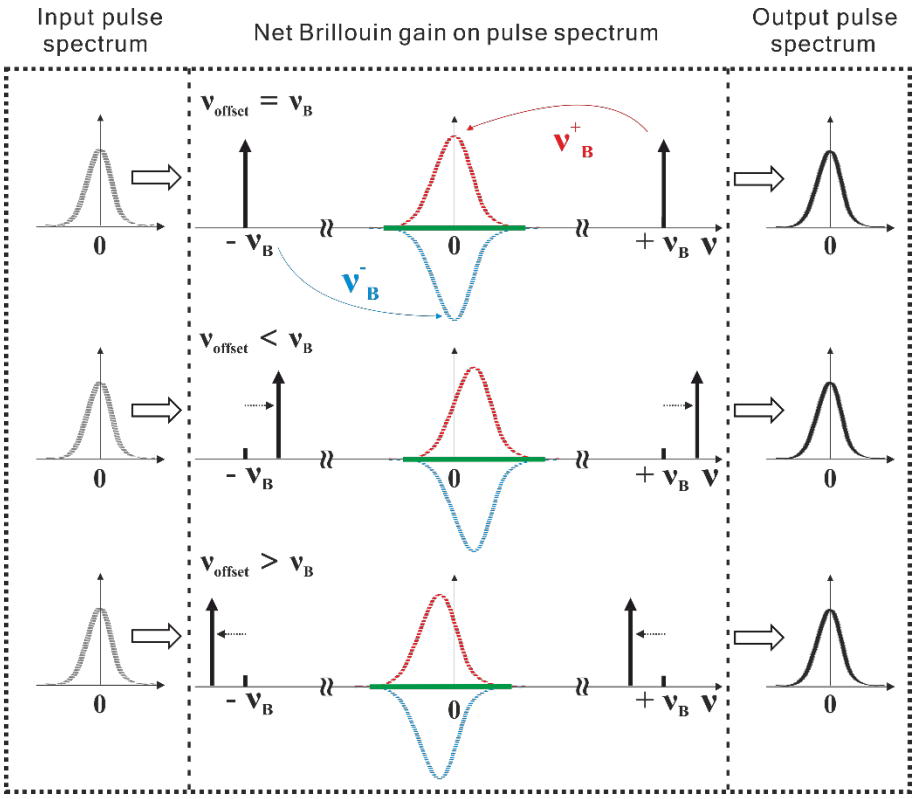

Figure 6.1: Net Brillouin gain affecting the pump pulse while scanning the pump-probe frequency offset (ν_{offset}) symmetrically around the pulse spectrum using the proposed scanning method, which keeps a fixed frequency separation between sidebands. Here ν_{offset} refers to the offset between the pump frequency (ν_{pump}) and the probe low sideband frequency ($\nu_{probe\text{-}LSB}$), (i.e. $\nu_{offset} = \nu_{pump} - \nu_{probe\text{-}LSB}$). Grey dotted lines: input pulse spectrum; red dotted lines: Brillouin gain spectrum generated by the upper-frequency probe sideband; blue dotted lines: Brillouin loss spectrum generated by the lower-frequency probe sideband; green solid lines: net Brillouin gain spectrum experienced by the pulse; black solid line: output pulse spectrum after SBS interaction [92].

At the moment of presenting this thesis another technique to smartly overcome non-local effects induced by strong probe powers has been presented by Ruiz-Lombera *et al.* [94]. Its working principle is based on dithering the probe frequency in order to create a large and flat gain/loss over the pump pulse, allowing them to inject a probe power of 8 dBm per sideband.

6.2.1 Experimental Validation of the Proposed Method

In order to experimentally validate the proposed scanning method, and its ability to measure correctly when using high probe powers, the scheme in Figure 6.2 has been implemented. This corresponds to a modified standard BOTDA scheme [18], [26], [88], [91], [93], where, in this case, the probe wave frequency is fixed while the pump pulse frequency is swept to properly scan the Brillouin gain or loss spectrum [92]. Note that such sweeping implementation is equivalent to the one illustrated in Figure 6.1.

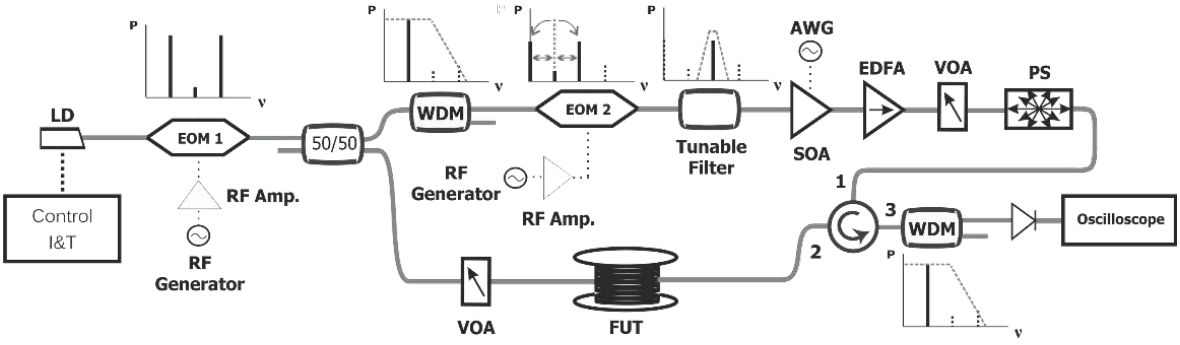

Figure 6.2: Experimental setup implemented to validate the proposed scanning technique. LD: laser diode; EOM: electro-optical modulator; WDM: wavelength division multiplexer; AWG: arbitrary waveform generator; SOA: semiconductor optical amplifier; EDFA: erbium doped-fiber amplifier; RF: radio-frequency generator; VOA: variable optical attenuator; PS: polarization scrambler; FUT: fiber under test [92].

First, the laser light is modulated using an intensity electro-optic modulator (EOM1), whose modulating frequency is set to match the dominant BFS (ν_B) of the fiber. The generated DSB continuous wave is split into two branches. One of them already constitutes the DSB probe and is directly launched into the sensing fiber, passing through a variable optical attenuator (VOA) that is used to precisely adjust the probe power launched into the fiber. The other branch is used to generate the pump pulse. For this, only one of the two sidebands is selected by a suitable narrowband filter. In this case a dense wavelength-division multiplexer (DWDM) is used to select the low-frequency sideband, which is then amplitude modulated by a second modulator (EOM2) at a frequency difference sweeping around the BFS ($\nu_B \pm \Delta\nu$). This new frequency component, which provides the pump wave, is selected through a narrow

tunable filter (~148 pm of bandwidth), wide enough to allow a frequency tuning along the selected spectral span, but narrow enough to filter out all unwanted spectral components. Subsequently, the signal is pulsed through a semiconductor optical amplifier (SOA), then amplified by an erbium doped-fiber amplifier (EDFA) and de-polarized by a polarization scrambler (PS) in order to avoid polarization fading in the measured temporal traces. At the receiver stage, a WDM is used as a narrowband filter to select only one of the probe sidebands, which is then detected by a 125 MHz high-transimpedance photoreceiver (50000 V/A). Note that this high transimpedance gain makes the system thermal noise limited (as demonstrated hereafter) and leads to measurements with optimized electrical SNR [49], [95].

6.2.1.1 Spectral Measurements of the BGS and BLS

In this section, the ability of the proposed scanning method to measure correctly even at high probe powers is experimentally verified. It should be noted that all the measurements have been performed for a spatial resolution of 2 m (20 ns pulse width), which actually corresponds to one of the worst conditions as reported in Chapter 5 and comfortably places the system in the small gain regime. To perform the scan as proposed in the novel method, only the frequency driving EOM2 is swept while the frequency of EOM1 is kept fixed at the dominant BFS of the last kilometers of the fiber. Actually, since the non-local effects under question result from a non-linear SBS interaction, most of the pump pulse distortion cumulates along the last fiber section (equivalent to the non-linear effective length L_{eff}), where the probe power propagating along the fiber is the highest. As a result, in the case of a very long sensing range (longer than $\alpha^{-1} \approx 20$ km), the frequency separation between the two probe sidebands has to be tuned to match the dominant BFS over the last $L_{eff} = \alpha^{-1} \approx 20$ km of fiber. However, as any other non-linear interaction, for shorter sensing fibers (shorter than $\alpha^{-1} \approx 20$ km), the critical interaction length will be reduced accordingly with L_{eff}.

Figure 6.3 shows the BGS (blue curve) and BLS (red curve) measured at the very end of a 50 km uniform SMF spool when a probe wave of 5 dBm/sideband is swept with the proposed method. Interestingly, no distortion is observed in this case. Note that a probe power of 4 dBm in the conventional DBS BOTDA scheme induces huge distortions in both BGS and BLS [see

Chapter 5, Figure 5.10(d)]; however with the proposed scheme these distortions have been reduced to a negligible level even with the use of a slightly higher probe power (5 dBm as employed in Figure 6.3). It should be also mentioned that similar spectral shapes have been verified experimentally for lower probe powers, all of them showing the usual well-behaved bell shape.

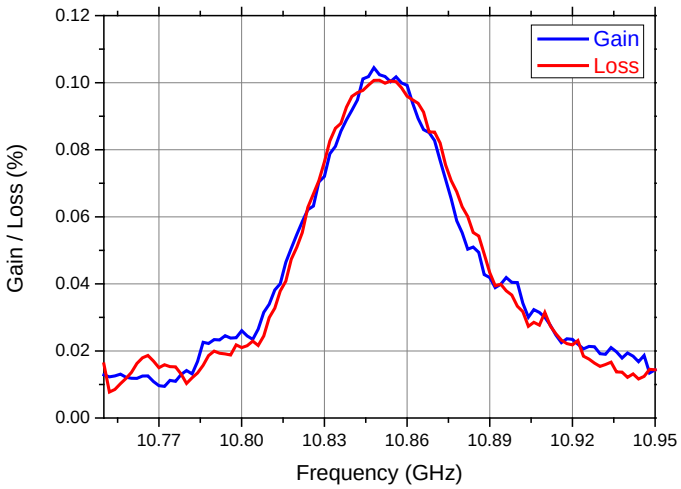

Figure 6.3: Measured BGS (blue curve) and BLS (red curve) at the end of a 50 km SMF spool using the proposed method with a probe wave of +5 dBm/sideband [92].

To better visualize the correct measurements provided by the method, 3D maps of the measured BGS and BLS are shown in Figure 6.4(a) - 5.4(b), respectively. They highlight that no distortions of the measured spectral shape along the entire sensing fiber are observed when using the proposed scheme with a probe power of 5 dBm/sideband. Compared to the conventional scanning method, a clear improvement is here demonstrated. This way the new sweeping method ensures correct measurement conditions and allows increasing the probe power in at least ~10 dB (from –5 dBm to +5 dBm), over the standard BOTDA scheme, being ultimately limited by the ASpBS threshold of the fiber (+7 dBm) [5], thus representing a 12 dB probe power increase.

It is worth mentioning that due to the increased probe power and the high-transimpedance photodetector used in the measurements shown in Figure 6.3, an optical attenuator has been placed in this particular measurement at the receiver front-end to avoid saturation of the

photodetector. Although no real SNR improvement can be claimed with the use of this attenuator in the system, this technical solution results helpful to demonstrate the significant reduction of the spectral distortions in the BGS/BLS measured when using high probe powers propagating along the sensing fiber. Results certainly validate the proposed scanning method, which best compensates the cumulated gain-loss SBS interaction occurring between the optical signals propagating along the sensing fiber. To complement this demonstration, results in Section 6.2.1.2 verify that the proposed method enables the correct detection of a short hot-spot (comparable to the spatial resolution), unlike measurements with the conventional scanning method which are highly affected by the pulse distortions previously described.

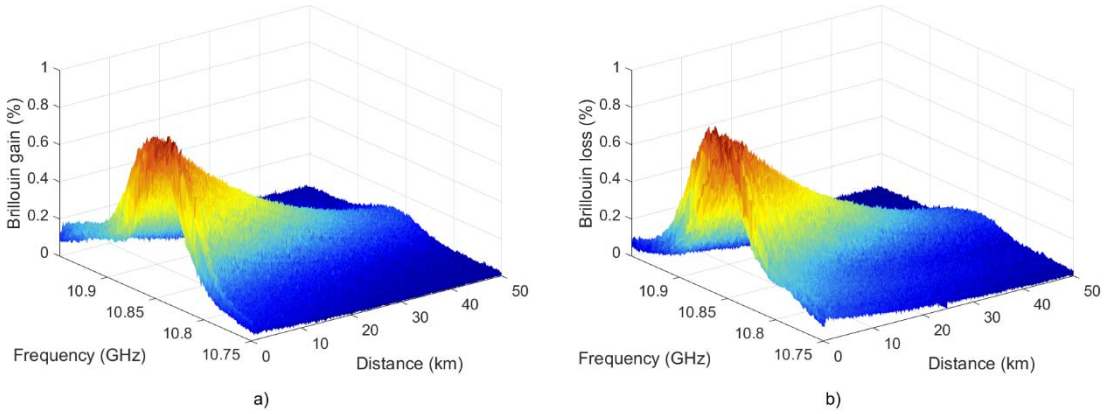

Figure 6.4: 3D maps of the measured (a) Brillouin gain and (b) Brillouin loss spectra along a 50 km-long sensing fiber, using the proposed scanning method. Compared to standard BOTDA measurements, here the spectra are not distorted at any location along the fiber [92].

Furthermore, it should be noted that the mentioned 12 dB increase in the probe power launched into the fiber provides a significant enhancement in the power budget of the system. This can be directly translated into a 12 dB SNR improvement in the measurements obtained by thermal-noise-limited BOTDA sensors. However, if an optical attenuator is needed to avoid saturation and/or other sources of noise dominate, such as shot noise or spontaneous-signal beat noise [49] (resulting when using an EDFA in the probe branch), the SNR improvement provided by the novel scanning method might be reduced. It remains that one of the main benefits of the proposed scanning method is the possibility of reaching longer sensing ranges due to the enhanced probe power that is launched into the sensing fiber, besides the undistorted

spectral measurements. The full advantages of the proposed scanning method will be shown in Sections 6.3 and 6.4, demonstrating undistorted BGS/BLS measurements along an extended sensing range of 100 km (Sections 6.3), and most importantly, resolving, for the first time to our knowledge, 1,000,000 sensing points in a time-domain Brillouin sensor Sections 6.4).

6.2.1.2 Hot-spot Detection

Until now, the analysis of distortion has been presented for the spectral and temporal shapes measured by the conventional and the proposed method. As reported in Chapter 5, non-local effects basically impact on the measured traces when long and uniform sensing fibers are used, along with high probe powers. The impact is therefore mostly observed over the last kilometers of fiber, where the probe wave is at its highest power level. If an event, such as a strain or temperature variation, occurs at the end of the sensing fiber, the distortions induced in the conventional BOTDA scheme will completely conceal the BGS/BLS spectral shift. For this reason, the measurement of a hot-spot placed near the far fiber end becomes essential to validate the proposed scanning method. In order to increase the signal contrast and provide better SNR to the measurements, this test has been carried out using a 25 km-long sensing fiber. It is important to notice that the fiber effective length, determining the ASpBS threshold [25] is only marginally reduced in this case (with respect to the effective length of 50 km, being $\alpha^{-1} \approx 20$ km), representing only a small variation in the conditions when compared to previous results. Nevertheless, to provide a reliable comparison, measurements with the standard BOTDA scheme have been repeated along the 25 km of fiber, and results are compared with the ones obtained with the new proposed method.

For this test, a 2 meter-long hot-spot has been placed at the end of a 25 km SMF spool, immersing the short fiber section into a hot-water bath at a temperature of ~53 ºC, while the room temperature has been measured to be 25 ºC. While Figure 6.5(a) shows the BGS and BLS measured just before the hot-spot location with the standard BOTDA scheme and a probe power of 4 dBm [same condition as in Figure 5.10(d)], Figure 6.5(b) shows the measured spectra at the exact position of the hot-spot. The huge distortions observed in this case make it

impossible to retrieve the correct temperature profile. As it can be seen, the 2 m hot-spot placed at the end of the fiber is confirmed to be completely concealed under the huge deformation of the gain and loss curves. Actually, with the level of distortion measured in this case, any fitting algorithm employed to obtain the peak of the BFS will fail to locate the real and proper frequency shift (either outside or at the very location of the hot-spot). For instance, the widely employed parabolic fitting [32] would in this case converge to a polynomial curve adjusted to any of the two strong spectral peaks, leading to a wrong BFS determination.

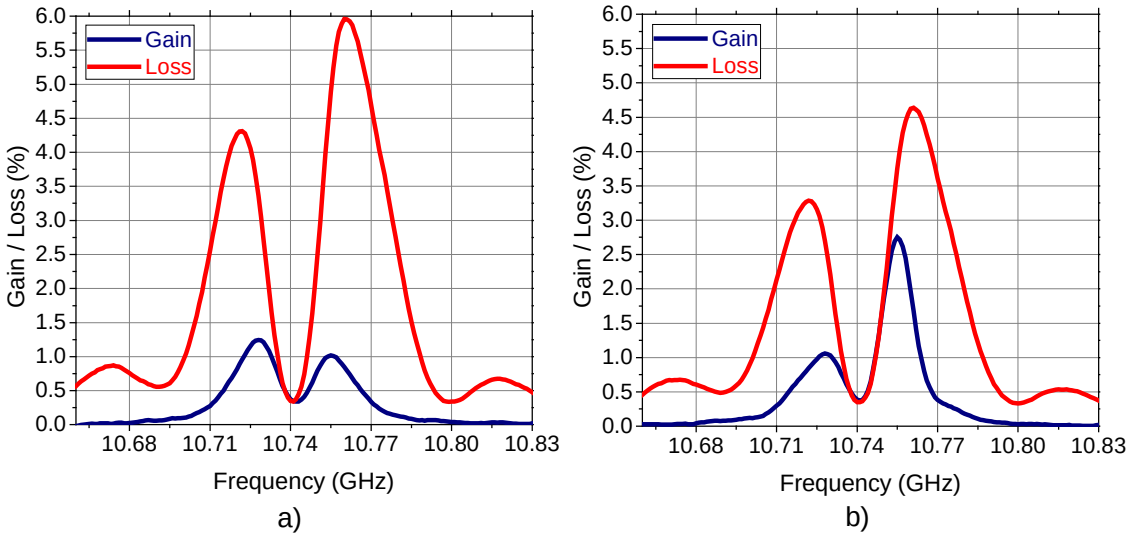

Figure 6.5: Brillouin gain and loss spectra measured at the end of a 25 km-long SMF spool where a 2-m hot-spot has been applied for a probe power of +4 dBm/sideband. (a) Profiles obtained a few meters before the location of the hot-spot. (b) Profiles obtained in the middle of the hot-spot when immersing the fiber in a hot-water bath [92].

On the other hand, when the proposed method is used, correct BGS and BLS shapes could be measured, as reported in Figure 6.6(a)-(b). In particular, Figure 6.6(a) shows the BGS/BLS measured a few meters before the hot-spot and at its precise location. It is important to mention that similar spectral shapes have been obtained, not only at 4 dBm, as in the case depicted in Figure 6.5(a)-(b) (used here as a reference for comparison), but also using higher probe powers. The particular broadening observed in the BGS/BLS inside the hot-spot shown in Figure 6.6(a) is probably due to some non-homogeneity in the heating process implemented to generate the hot-spot on the fiber. Actually, the pump pulses have been monitored at the output of the fiber for several probe frequency detuning to verify any potential impact of residual non-local

effects. As shown in the inset on Figure 6.6(a), the pulses remain essentially undistorted at the fiber output regardless of the probe frequency detuning, demonstrating negligible levels of non-local effects. It should be noted that the particular case shown in Figure 6.6 has been measured with a probe power of +8.4 dBm/sideband, which, to our knowledge, matches the highest probe power reported in a BOTDA sensor to date. This represents a considerable performance improvement in BOTDA sensing, while ensuring no visual impairment in the measurements. Figure 6.6(b) shows the retrieved temperature profile around the hot-spot location when using such a high probe power, confirming the correct determination of the applied temperature change.

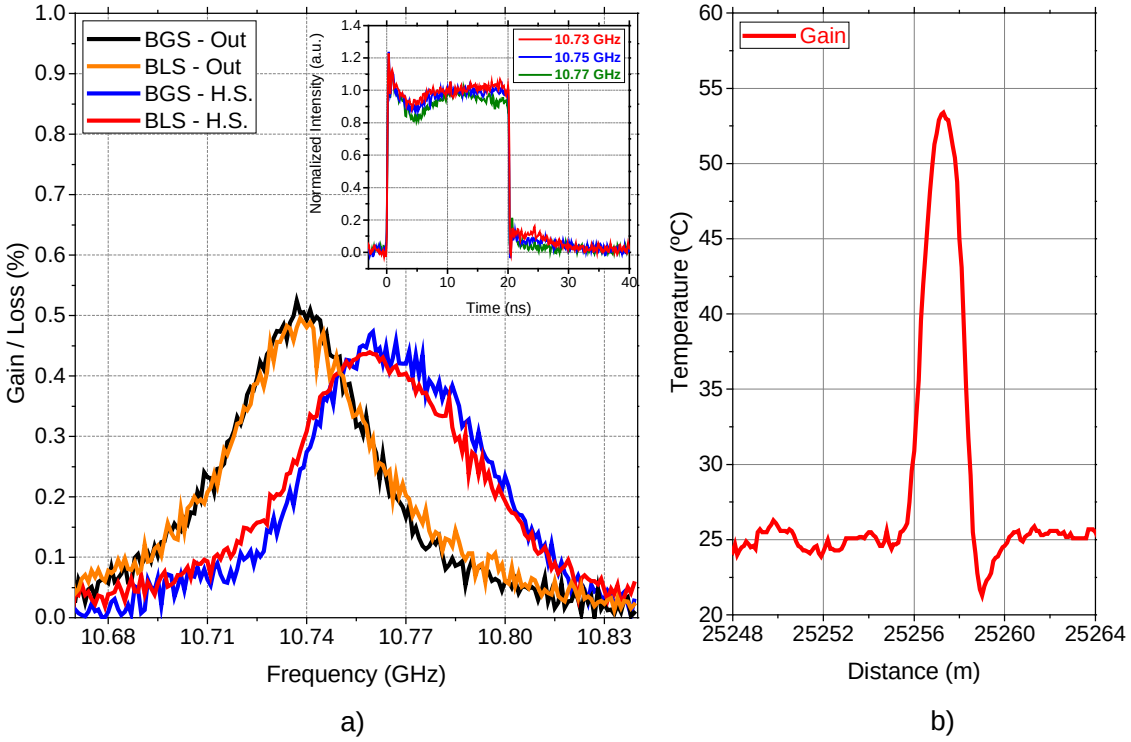

Figure 6.6: Detection of a 2 m-long hot-spot with the proposed BOTDA scanning method using a probe power of +8.4 dBm/sideband. (a) Brillouin gain and loss spectra measured at the end of a 25 km-long SMF spool where the hot-spot has been applied (black and orange lines: a few meters before the hot-spot; red and blue lines: at the precise location of the hot-spot). (a: Inset) Output pulses for several probe frequency detuning. (b) BFS profile translated to absolute temperature around the hot-spot position (profile obtained from the measured BGS). "BGS/BLS-Out": Gain/loss profiles obtained a few meters outside the hot-spot. "BGS/BLS-H.S.": Gain/loss profiles obtained in the middle of the hot-spot [92].

6.3. Very-long Range BOTDA Sensor

Making use of the improved operating conditions above demonstrated for the proposed scheme and owing to the increased probe power, measurements along 100 km with 2 m resolution turned possible without the need of additional advanced methods, such as coding techniques [68], [89], distributed amplification [54], [55], image processing [90] or some combinations of them [56], [96]. Figure 6.7 shows the BOTDA amplitude trace at the averaged peak gain frequency (pump-probe frequency shift of ~10.856 GHz) along the 100 km fiber span. As it can be observed, the fiber end is perfectly visible, showing a good contrast with the background noise (SNR of ~6 dB at 100 km distance). The decay in the decibel scale is perfectly linear, which also ensures that only the linear fiber attenuation is acting on the pump pulse, with negligible levels of pump depletion. The slight disturbance observed at 50 km is due to the fiber pigtails and connectors used to join the two ~50 km SMF spools together. The pump pulse peak power employed in this case is ~14 dBm and the probe wave is ~5 dBm/sideband, while each time trace has been averaged 16000 times.

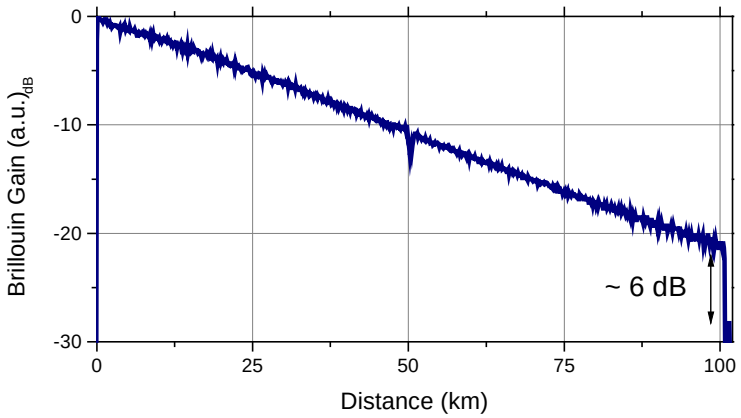

Figure 6.7: BOTDA trace represented in logarithmic scale along a 100 km-long sensing fiber, for a pump-probe frequency offset of 10.856 GHz [92].

To further verify the performance of the implemented sensor, a 5 meter hot-spot has been placed at the end of the fiber (around 100 km) in a hot-water bath at ~60 ºC (being the room temperature around 25 °C). A full frequency sweep is performed to retrieve the BFS change at the hot-spot position; the retrieved temperature profile around the hot-spot is shown in

Figure 6.8. A ~35 ºC change over room temperature is verified at the hot-spot location (considering a linear relation temperature-frequency ≈ 1ºC/MHz), which matches the real temperature difference. The sensing uncertainty (estimated as the standard deviation of the repeatability in consecutive measurements) around the hot-spot is 2.4 ºC. In addition, the spatial resolution of the system has been verified to be 2 m, which has been determined by analyzing the length of the temperature transient in the detected hot-spot. Moreover, the hot-spot is correctly identified as being ~5 m long.

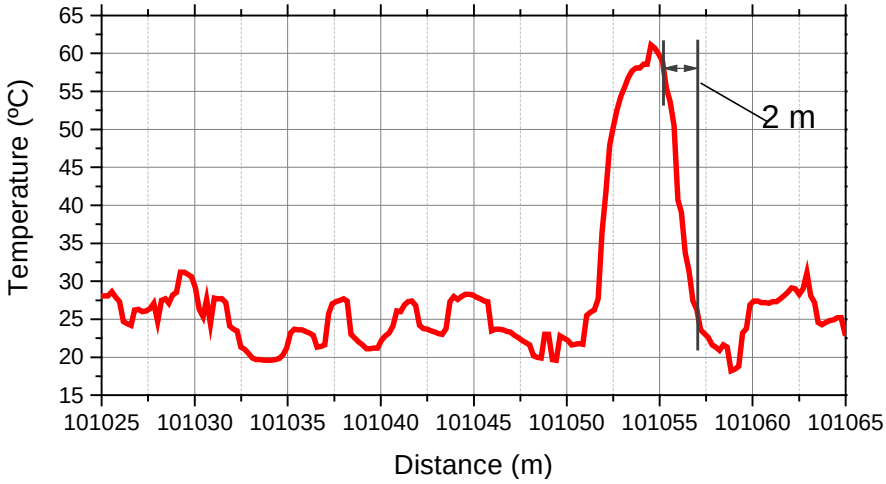

Figure 6.8: Retrieved BFS profile translated to the absolute temperature, measured for a ~5-meter hot-spot located around a 100 km distance [92].

It should be highlighted that this kind of measurements at 100 km with 2 m resolution are basically impossible to perform with conventional DSB setups. These performances can only be reached by using range enhancement techniques such as the ones previously mentioned [54]–[56], [68], [89], [90], [96]. This comes from the low SNR resulting from the reduced probe power (< -5 dBm/sideband) required to avoid spectral distortions in the measurements and the large cumulated fiber loss (20 dB for 100 km sensing range) experienced by the probe before reaching the detector. With no pre-amplification before detection, these conditions make the BOTDA system to be thermal-noise dominated, even when using the raised probe power enabled by the proposed scanning method. This has actually been verified in our setup by measuring the noise standard deviation of the electrical trace measurements (4.37 mV),

which is essentially identical to the one measured when no light enters into the photodetector (4.34 mV). Such noise behavior implies that the proposed scanning method provides a figure-of-merit (FoM) [32] enhancement of about one order of magnitude with respect to conventional scanning methods, which follows the ~12 dB SNR improvement accomplished in the implemented BOTDA system. The simplicity of the proposed setup makes these results even more impressive when compared with other studies reaching similar distances.

6.4. Resolving 1 Million Sensing Points in an Optimized DPP-BOTDA Sensor

As already known, augmenting the signal-to-noise ratio of the system improves the overall performance of BOTDA-based schemes [32], where, as previously seen, it can be used to significantly boost the sensing range of the sensors [56], [62], [92], [97]. Likewise, the SNR enhancement could serve to improve the system spatial resolution, and consequently, increase the number of resolved sensing points along the fiber. However, in conventional Brillouin sensing, the spatial resolution cannot be reduced below ~1 m, since the acoustic wave does not get fully built-up for interaction times < 10 ns (see Section 3.3.2 for further details).

To overcome such limitation and achieve sub-metric spatial resolution, different solutions have been proposed based on frequency, correlation [41]–[44] or time-domain [74], [75], [98] approaches. All of these techniques aim at increasing the number of resolved sensing points in the fiber. Frequency- and correlation-domain approaches allow very sharp spatial resolutions (in the order of mm or a few cm), in spite of a measurement range typically limited to a few km. Using correlation-based schemes, a significant increase in the number of resolved points has been demonstrated along fibers of several km-long [42]–[44]; however, the total measurement time still remain extremely long, e.g. a few hours for 1 million points [42]. Conversely, time-domain approaches, which typically make use of differential pump pulses, are the preferred option when a faster acquisition time is intended.

The differential pulse-width pair (DPP) technique [74], [98] is based on the subtraction of two temporal traces, each of them obtained using long pump pulse widths of slightly different

duration. The resulting spatial resolution is determined by the difference between the pulses width, and thus, it highly depends on the rising/falling time of the used optical pulses (see Section 3.4.4). Typically, the long pulses duration is chosen to be large enough to properly build up the acoustic wave (e.g. 50-60 ns). In such case, however, the polarization noise (which is a fraction of the measured traces) becomes dominant in the differential trace. To secure correct DPP measurements, the polarization noise amplitude must be kept below the one of the differential trace, which scales with the differential pulse width. Reducing the width of the long pulses implies less relative polarization noise in the differential trace, but also a shorter interaction length, and hence a weaker response. In summary, there is an optimum to be found in the width of the pair of long pulses when aiming to reach very high spatial resolution.

In this section, it is proven that the limitations to extend the sensing range or to improve the spatial resolution of differential pulse techniques are not decisively due to the reduced measurement SNR resulting from the larger attenuation in longer fibers, particularly critical considering the lower energy contained in shorter differential pulses, but are primarily due to spectral and temporal distortions affecting the pump pulses, and ultimately due to the limited polarization noise elimination.

Aiming to maintain the resolution all along the sensing fiber in a DPP scheme, it turns critical to ensure well-shaped and non-distorted pulses along the entire sensing range. However, as thoroughly reported in Chapter 5, the conventional DSB-based BOTDA sensing measurement technique does not secure this condition, due to the large temporal distortion that pump pulses experience when a large probe power is used.

By combining DPP-BOTDA with the above-described scanning technique [92], the pulse distortion can be significantly mitigated, making it possible to increase the probe power launched into the fiber (theoretically limited by the onset of ASpBS [92]), enhancing the SNR of the sensor, while securing very sharp spatial resolution. To demonstrate this, a DPP-BOTDA system has been implemented, as shown in Figure 6.9, using the novel scanning technique described in Section 6.2 (see Figure 6.1). In this scheme, compared to the previous implementation (Figure 6.2), the selected band is the Brillouin loss one, but the pump and probe branches are developed in the same way as it was explained before (see Section 6.2 for

further details). Additionally, in this case, right before launching the probe into the fiber-under-test (FUT), it goes through a polarization synthesizer (P. Synth.), which is used to reduce polarization noise in the measured temporal traces.

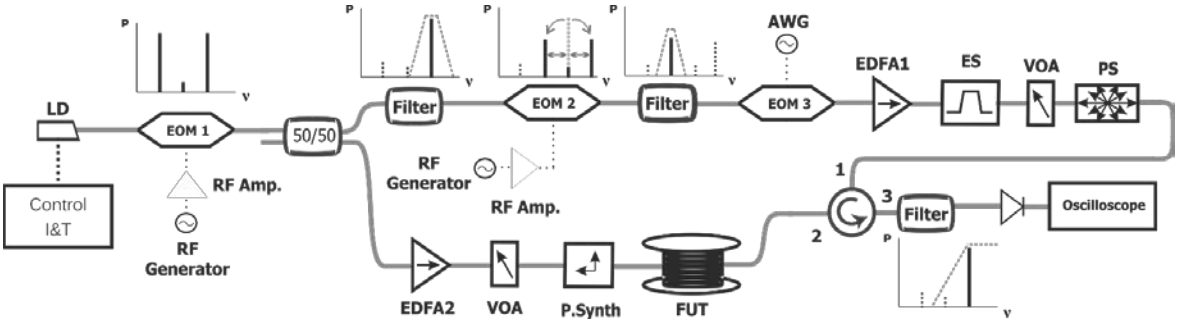

Figure 6.9: Experimental setup. LD: Laser Diode; EOM: Electro-Optical Modulator; AWG: Arbitrary Waveform Generator; EDFA: Erbium Doped Fiber Amplifier; VOA: Variable Optical Attenuator; P.Synth: Polarization Synthesizer; ES: Electrical Switch; PS: Polarization Switch; FUT: Fiber Under Test [99].

To increase the extinction ratio (ER) of the pulses (30-40 dB at the EOM output), an electro-optical MEMS switch (ES) is used to gate the pulses and ensure an overall ER higher than 80 dB. Before entering the circulator, the pulses go through a fast polarization scrambler, which helps reducing the polarization fading in the traces (in addition to the polarization synthesizer). After selecting the Brillouin loss component by means of a DWDM filter, the signal is fed into a high-bandwidth (9.5 GHz) photo-receiver.

In order to analyze the performance of the above explained technique, full DPP-BOTDA measurements have been carried out over a 10 km SMF, presenting a homogeneous BFS of ~10.855 GHz along the entire fiber. In the measurements, sharp squared pulses (100 ps fall time) of 26.4 ns and 26.3 ns have been used, thus, resulting in a spatial resolution of 1 cm (100 ps width difference). Such pulse widths are short enough as to mitigate polarization fluctuations in the BOTDA traces and wide enough to generate a sufficient Brillouin interaction to enable the DPP technique. The pump pulse peak power is ~100 mW while the probe wave is ~2 mW (3 dBm) per sideband. To evaluate the impact of the proposed scanning method on the reduction of the pulse distortion, pulses are measured at the output of the sensing fiber, i.e. after propagating along the 10 km-long fiber and interacting with the probe wave

through SBS. Figure 6.10(a) shows the acquired long pump pulses and the resulting differential pulse (subtraction among long pulses) using the conventional scanning method. Measured shapes illustrate the temporal distortion experienced by the two long pump pulses when the pump-probe frequency offset is detuned by +25 MHz from the average BFS. It can be observed that such a non-negligible temporal distortion leads to a complete jamming of the differential pulse resulting from the subtraction of the long and short pulses [red line in Figure 6.10(a)]; thus making the DPP technique not reliable for this sensing range and probe powers.

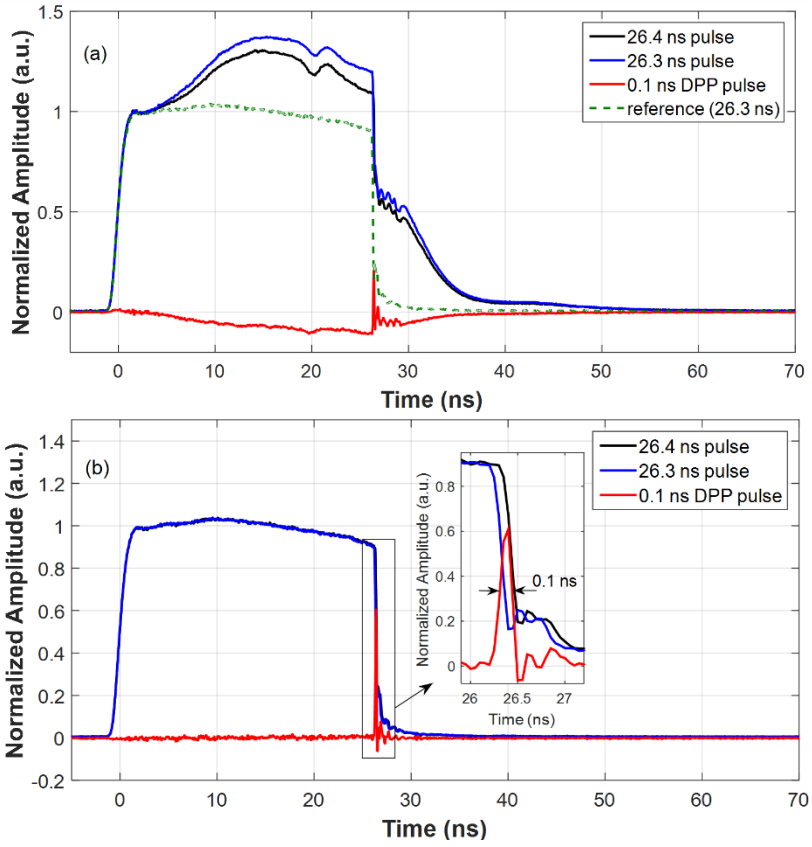

Figure 6.10: DPP working principle, presenting the long and short pulses (black and blue, respectively), and the resulting differential pulse (red). (a) DPP on the conventional BOTDA sweeping method, showing a distortion in the pulses for a +25 MHz frequency detuning (non-distorted 26.3 ns pulse is shown in green dashed-lines for reference), and a null differential pulse. (b) DPP-BOTDA using the proposed scanning procedure: both long pulses remain well-shaped, while the differential pulse shows a correct shape and the expected 100 ps width [99].

However, as it can be seen in Figure 6.10(b), by making use of the proposed scanning procedure, the long pump pulses maintain their original shape along the entire fiber, regardless the probe power and frequency detuning. This behavior secures the correct operation of the DPP-BOTDA technique, showing a well-shaped differential pulse of 100 ps along the entire sensing fiber. It should however be mentioned that a penalty (~2 dB) on the peak power of the differential pulse can be observed, which results from the limited bandwidth of the pulse generator used in the experiment (defining a pulse falling time of 100 ps, being similar to the expected differential pulse width).

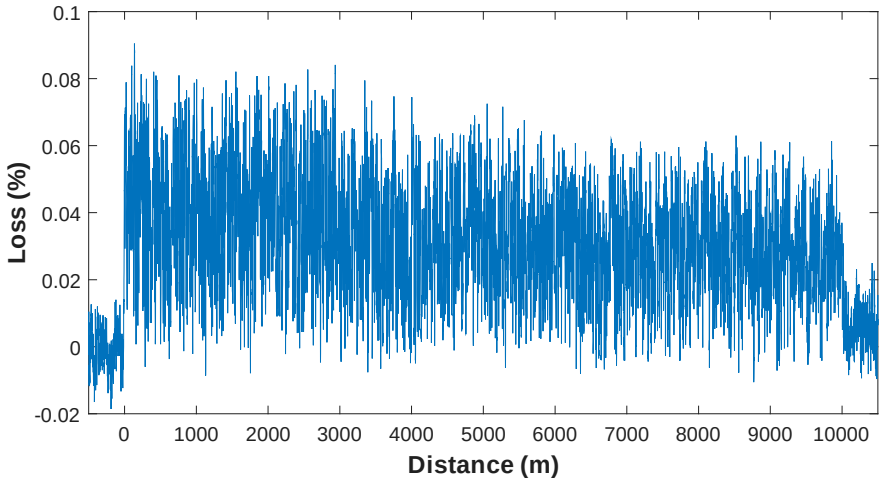

Figure 6.11: DPP-BOTDA trace along the 10 km SMF using a differential pulse of 100 ps (1 cm resolution) at a gain peak frequency of 10.855 GHz [99].

Note that in the implemented DPP-BOTDA sensing scheme, the intended spatial resolution (1 cm) is obtained by subtracting traces measured with pump pulses of 26.4 ns and 26.3 ns, which means that the 100 ps differential pulse corresponds to a ~0.3 % of the total pulse width. In such a scenario, minimizing polarization fading in the trace and noise resulting from time-varying polarization issues turns out to be essential. Thus, a redundant polarization scrambling scheme has been utilized in both the pump and probe waves. On one side, the pump is scrambled by means of a fast polarization scrambler. On the other side, the probe goes through a polarization synthesizer which sets its state to six different polarization states (three pairs of orthogonal polarization states). This way, the impact of polarization fading and time-varying polarization issues on the differential time-domain traces can be substantially reduced,

thus providing a reliable differential trace measurement, as shown in Figure 6.11. Although the differential trace shown in Figure 6.11 looks to have large amplitude fluctuations, the SNR calculated at the end of the sensing fiber (around 10 km distance) is ~4.2 dB, thus securing a large enough signal contrast for reliable BFS determination [32].

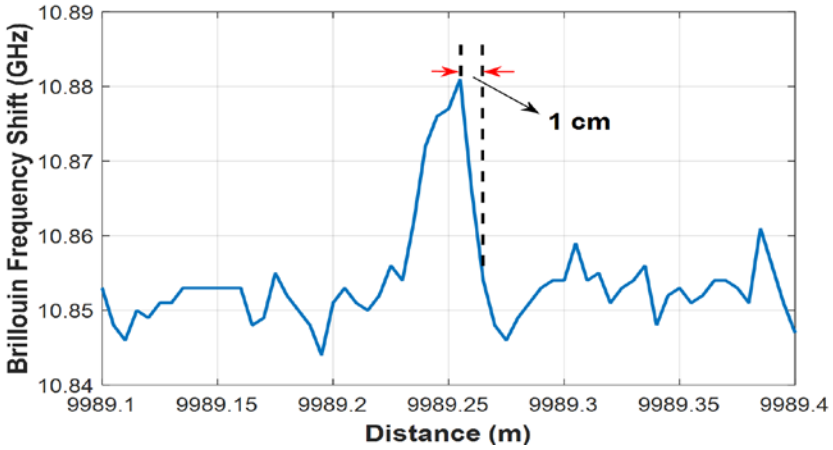

Figure 6.12: BFS evolution at the far end of the fiber showing a 3 cm hot-spot presenting a BFS offset by ~30 MHz with respect to the unheated fiber [99].

The system performance has been finally evaluated by creating a 3 cm hot-spot at the end of the FUT by attaching a resistor to the fiber section, and applying a current high enough to heat the fiber up to ~56 °C. A full frequency sweep has been carried out, where each temporal trace has been averaged 18000 times. The evolution of the BFS along the FUT has been obtained by fitting a parabolic curve to the measured Brillouin loss spectrum [32], and a zoom in the last few meters of fiber is presented in Figure 6.12. The measured BFS evolution demonstrates the presence of a hot-spot around 9989 m. The heated section shows a BFS at ~10.880 GHz, offset by ~30 MHz when compared to the rest of the fiber at room temperature (~25 °C), thus confirming the ~30 °C increase when using the estimated conversion factor of 1MHz/°C. The measured hot-spot width is 3 cm, with a transient distance of 1 cm, demonstrating the expected spatial resolution of the DPP-BOTDA sensor.

The frequency uncertainty measured in this case at the end of the fiber is ~3.1 MHz, being in agreement with the theoretical expected value based on the measured SNR [32]. It should be highlighted that the achieved spatial resolution of 1 cm over a sensing range of 10 km

represents an equivalent of 1’000’000 resolved points, which constitutes a state-of-the-art record number of points using a Brillouin time-domain sensor. Compared to correlation-domain methods reaching the same number of points, the DPP-BOTDA scheme here implemented leads to a significant reduction in the measurement time, from several hours down to only a few minutes. In particular, in our experiment, the measurement time has been reduced down to ~20 min.

6.4.1 High-resolution Sensor over an Extended Sensing Range

The previously presented result features a vast number of sensing points retrieved in a relatively short time over 10 km of fiber. However, some applications could require sensing short spatial resolutions over extended sensing ranges (tens of kilometers). The work presented in this subsection seeks extending the sensing range using the proposed method, and it successfully achieves a 5 cm spatial resolution DPP-BOTDA sensor over 25 km of fiber [100], and ultimately, a sensing range of 37.5 km featuring 20 cm of spatial resolution [101].

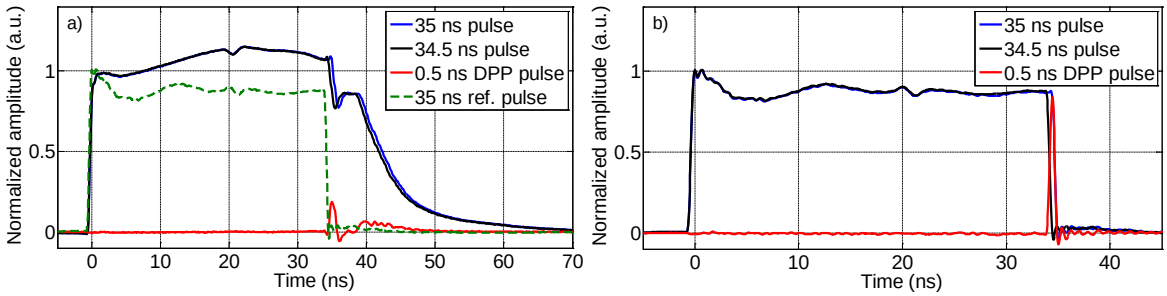

Figure 6.13: Output pulses of the DPP technique applied to both the (a) conventional (+15 MHz pump-probe frequency detuning) and (b) novel scanning methods, obtained at the end of a 25 km SMF [100].

In this case, the implemented scheme is analogous to the one presented in Figure 6.9, although now, the polarization diversity scheme has been simplified, where both the polarization synthesizer and the scrambler present in Figure 6.9 have been substituted by a fast polarization switch.

In the first implementation, the pair of long pulses is chosen to be 35 ns and 34.5 ns wide, being the differential pulse width 0.5 ns. Such differential pulse, in this case, is 1.4% of the total pulse width, and thus, the polarization-induced noise becomes less critical in the resulting measurements compared to the previously analyzed result. Figure 6.13 illustrates the effectiveness of the proposed method, which successfully enables the DPP technique, guaranteeing non-distorted $500\ ps$ –width pulses (5 cm of spatial resolution) along the entire fiber length (25 km).

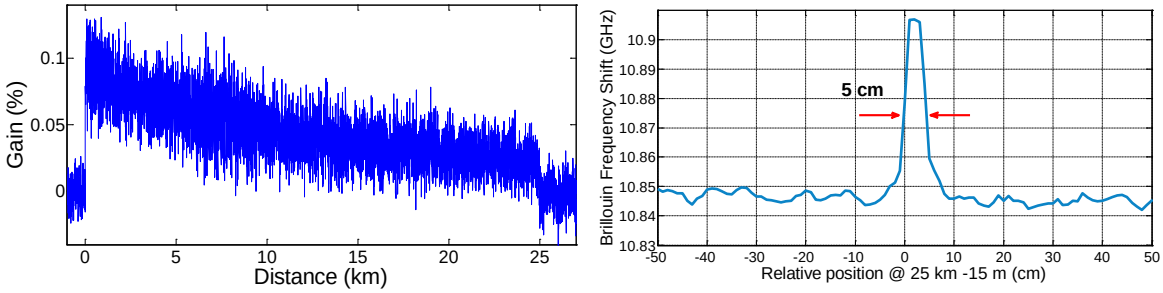

Figure 6.14: a) DPP-BOTDA trace of a 25 km SMF for a differential pulse of 500 ps width (5 cm spatial resolution). b) BFS evolution at the far end of the fiber, where a 5 cm piece of fiber has been strained 1200 $\mu\varepsilon$ [100].

The system performance has been evaluated by elongating a 5 cm section of the fiber located at the end of the FUT. The elongation has been precisely controlled gluing the fiber to a micro-metric translation stage, in order to induce a calibrated and known strain over the fiber. The differential temporal traces show a sufficient signal contrast along the entire 25 km fiber [Figure 6.14(a)] as well as a correct exponential decay. The signal-to-noise ratio (SNR) calculated at the end of the fiber is ~3 dB, where all the traces have been averaged 16000 times. In addition, the evolution of the BFS along the FUT has been obtained, and a zoom in the last few meters of fiber is presented in Figure 6.14(b). The measured BFS evolution demonstrates the presence of a short fiber section where positive strain is induced. The elongated piece of fiber presents a BFS of ~10.905 GHz, which implies a frequency difference of ~60 MHz when compared with a non-strained fiber section. If the conventional strain-to-frequency conversion parameter is used (~$0.05\ MHz/\mu\varepsilon$) (see Chapter 1, Subsection 1.5.1), the estimated induced

strain (~1200 με) matches the applied elongation of 60 μm. The frequency uncertainty measured at the end of the fiber is ~2.1 MHz, which matches the expected theoretical value for the calculated ~3 dB SNR. The strained section is proven to be 5 cm long, which actually validates the system spatial resolution. In this case, such effective spatial resolution and sensing range corresponds to 500,000 sensing points.

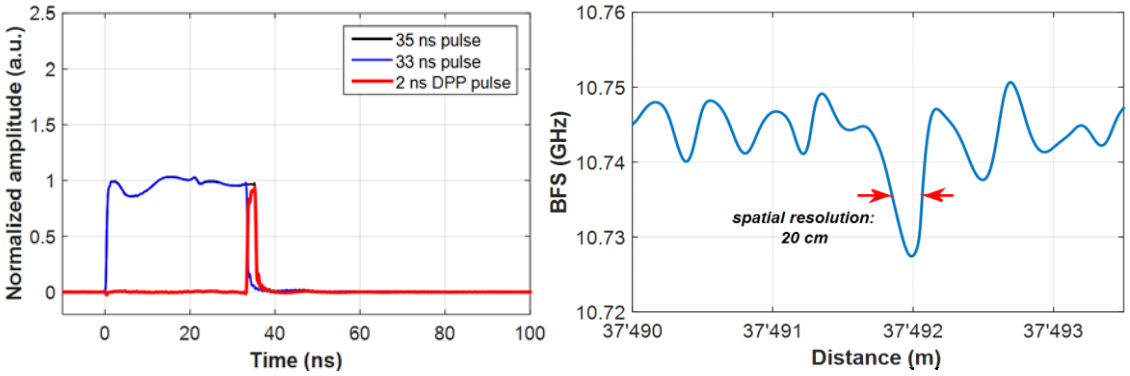

Figure 6.15: a) Output pulses of the DPP-BOTDA with the novel scanning method, verifying a differential pulse of 2 ns width (20 cm spatial resolution). b) BFS evolution at the far end of the fiber, where a 20 cm piece of different fiber (with a different BFS) has been strained spliced [101].

Finally, the last set of results is presented in Figure 6.15, where the proposed combination of methods has allowed reaching 37.5 km with a spatial resolution of 20 cm. Figure 6.15(a) illustrates the correct functioning of the DPP technique, having a well-shaped squared differential pulse of ~2 ns. On the other hand, in order to verify the high spatial resolution provided by the system, a 20 cm section of a different fiber (presenting a different BFS) has been spliced near the end of a 37.5 km SMF spool. A full and fast frequency sweep has been carried out, where all of the temporal traces have been averaged 2000 times. The evolution of the BFS along the FUT has been determined, and a zoom in the last few meters of fiber is presented in Figure 6.15(b). The estimated BFS at each position demonstrates the presence of a slightly different piece of fiber, whose BFS is determined to be ~10.728 GHz. In this case, the frequency uncertainty measured at the end of the fiber is ~1.9 MHz.

This latter result, i.e. 37.5 km of sensing range resolved every 20 cm, corresponds to ~190,000 independent sensing points, which are acquired in a relatively fast manner (only 2000 averages).

6.5. Conclusions

In previous Chapter 5, a thorough investigation on the non-local effects impacting on the response of conventional BOTDA sensors based on high-power DSB probe was presented. In the present chapter, a novel scanning technique for Brillouin optical time-domain analysis, which aims to solve the previously introduced detrimental non-local effects, has been proposed and validated. The measuring methodology is based on varying the pump-probe modulation structure by just fixing the probe sidebands frequency separation to match twice the dominant Brillouin frequency shift of the last fiber section (coinciding with L_{eff}), and then sweeping the pump pulse frequency. Note that the non-local effects under question would be reduced if the sensing fiber presents several sections with different BFS, since the cumulative effect over the pump pulse is averaged among the different BFS distributions. However, it is usually expected that single fiber spools would show a relatively uniform BFS, making the proposed system helpful for most real-case applications. If the BFS uniformity changes along the fiber, for instance as a result of fiber properties or environmental conditions, the proposed method with a fixed frequency separation between probe sidebands would turn less critical, but would not impair the sensor performance. Only if the BFS distribution along the last kilometers of the fiber presents a considerable and long enough frequency step, the proposed technique could become less effective near the fiber end and even non operative in extremely unlikely situations, but fortunately it will never result in a higher pump pulse distortion when compared to the conventional BOTDA scanning procedure, and can be considered as the best case situation in terms of cumulated distortion.

This method ensures cancelation of the probe-induced gain and loss spectra over the pump for the complete frequency span analyzed. Experimental results prove that this method enables the probe power to be increased until the onset of ASpBS, with no visible distortion on the

gain/loss curves, thus providing high robustness against pump depletion and non-local effects. The possibility of raising the probe power is translated into a sensor performance improvement, as the SNR of the measurements can be strongly increased. Of course, matching the proper pump-probe frequency shift of the fiber is critical to ensure correct measurements, but this can be realized by a coarse measurement at large spatial resolution and low probe power. Under these conditions, experimental results have demonstrated that, in a thermal-noise-limited BOTDA system, the proposed scheme results in a FoM [32] improvement of about one order of magnitude over the traditional sweeping scheme, directly mapping the 12 dB increase in probe power. Such a significant SNR improvement has granted achieving successful measurements over a sensing range of 100 km with 2 m of spatial resolution (16000 averages) and 2.4 ºC uncertainty, without any extra assistance.

Ultimately, fundamental limitations imposed by temporal distortions of pump pulses in a DPP-BOTDA sensor, and up to now preventing mid to long-range high spatial resolution sensing, have been here identified and mitigated using the novel scanning method. The proposed technique ensures non-distorted pump pulses (time and frequency wise) while enabling to raise the probe wave power launched into the sensing fiber. Such a power increase enhances the overall system performance, enabling in this case to improve the spatial resolution down to 1 cm over an extended sensing range of 10 km. This result is, to the best of our knowledge, the first demonstration of a time-domain Brillouin sensor capable of resolving 1’000’000 sensing points along a single optical fiber. Given the time-domain nature of the implemented scheme, the measurement time can be substantially reduced from the hour-scale (typically required by correlation-domain Brillouin sensing to scan 1 million points) down to a few minutes.

Additionally, the sensing range has been significantly increased, while keeping a high spatial resolution. Doing so, a spatial resolution of 5 cm has been demonstrated along 25 km of sensing range, as well as 20 cm over 37.5 km. This implies 500,000 and 190,000 independent sensing points resolved along the fiber (for 25 and 37.5 km respectively).

All of these results represent a considerable upgrade in the current state-of-the-art of BOTDA sensors. The impact and applicability of the proposed method is furthermore

highlighted since it allows combining it with other additional techniques, such as Raman assistance, image processing or pulse coding, to keep further enhancing the overall system performance.

Chapter 7:
Conclusions and Open Lines

7.1. Conclusions

In conclusion, several works and studies on the analysis and optimization of Brillouin Optical Time Domain Analysis (BOTDA) schemes have been reported in this thesis. In the first part of it, the theoretical fundamentals of the physical processes in which BOTDA schemes are based were presented, focusing on the Brillouin scattering, particularly in its stimulated regime (SBS). The main limitations of the technique are studied, in terms of power, resolution and noise. Safe-operating pump and probe powers are given, in order to avoid detrimental effects on the interacting signals such as MI or non-local effects induced by the probe wave. Additionally, several of the approaches used to overcome such limitations have been reported, according to the current state-of-the-art of BOTDA sensors.

The first result here presented is the successful application of balanced detection to BOTDA sensors. It has been shown that a balanced detection among Brillouin gain and loss bands in a conventional dual-sideband probe scheme leads to a doubling in the amplitude of the BOTDA trace and a SNR improvement of a factor of $\sqrt{2}$ in conventional conditions. In

addition, the technique has proven to be extremely effective in cancelling common-mode noise (i.e. any source of noise present in both probe sidebands), as well as demonstrating a strong robustness to the deterioration of the pump pulse extinction ratio. This feature is extremely useful when used in combination with Raman assistance schemes in BOTDA. In this case, making use of balanced detection effectively eliminates the RIN transfer arising from the Raman pumps to the Brillouin probe signals. Moreover, it can still be combined with other enhancing techniques, such as pulse coding or image processing. The successful application of balanced detection to Brillouin sensors has been awarded a patent, which is detailed in Appendix A, which also includes a comprehensive list of the published contributions derived from the work here presented.

In addition, in this thesis, a thorough analysis of non-local effects impacting on the response of conventional BOTDA sensors using mid- to high-power DSB probe has been presented. Experimental results have verified that, contrary to the common acceptation up to now, non-local effects do appear in conventional dual-sideband BOTDA schemes well below the ASpBS threshold, especially when using long fiber sections showing uniform BFS. It has been proven that these non-local effects originate from the symmetrical scanning of the pump-probe frequency offset in conventional DSB-BOTDA schemes. Such detrimental effects entail massive spectral and temporal distortions of the pump pulse, consequently altering the shape of the Brillouin gain and loss profiles, particularly at the end of the fiber, where the probe power is the highest. This leads to errors in the BFS estimation, and imposes serious limitations to the performance of conventional BOTDA sensors. It has been demonstrated that in long-range BOTDA schemes (i.e. where $L_{eff} \approx 20\,km$), for probe powers as low as -5 dBm ($\sim 300\ \mu W$) per sideband, there appear noticeable distortions on the Brillouin gain and loss spectra, which implies a safe-scenario limit ~10 dBm lower than what was considered up to now.

Aiming to validate a procedure to solve such limitations in BOTDA sensors, a novel scanning technique has been presented. The technique effectively overcomes the restrictions imposed by the appearance of detrimental non-local effects induced by the probe, allowing a significant increase of the used probe power, and consequently, considerably augmenting the

system SNR. Such interesting feature has led to two major state-of-the-art records: first, a BOTDA sensor that reaches 100 km with a 2 m spatial resolution has been achieved without using any kind of amplification and in a conventional acquisition time; furthermore, a sensor that resolves, for the first time to our knowledge, 1,000,000 sensing points in a time-domain Brillouin sensor, featuring 1 cm of spatial resolution over 10 km of SMF. The acquisition time in this case is kept under a few minutes, which means a one order of magnitude reduction when compared to other methods for an equivalent performance.

7.2. Field-Test Applications

In addition to the on-lab work presented in this thesis, we had the opportunity to further test the developed sensors in several field applications:

- First, the Interreg-Sudoe ECOAL project aimed at surveilling extremely high temperatures of a self-burning charcoal-waste pile in the Portuguese region of Porto. The leftovers of a mining field, inoperative since the 1970s, ignited after a thunderstorm hit the area in 2005. Ever since, the pile has been continuously burning, where the ground shows temperatures as high as 300 ºC while emitting hazardous gases. Our task was to build a BOTDA sensor able to register temperature changes in a heat-resistant fiber deployed. The system incorporated some of the advancements here presented, such as the balanced detection in combination with the DPP technique to allow sub-meter spatial resolutions. It was able to successfully provide enough information as to produce a detailed 3D temperature map of the monitored area, which ultimately has been used by geological experts to properly address the problematic. Moreover, this has resulted in several conference and journal publications [102]–[105].

- Secondly, at the moment of preparing this thesis, another project is undergoing. This one, known as REPARA 2.0 project, pursues monitoring the integrity of roads and transportation infrastructures. The task, in this case, was to study and prevent structural-failure in a road affected by an imminent landslide by obtaining strain

information on a fiber installed parallel to the track. The installation features a strain-sensitive fiber cable, which provides the information of interest, along with a telecom cable used to compensate the BFS temperature variations. The deployed BOTDA sensor will provide strain information of the fiber displacement suffered by the structure along one year.

7.3. Open Lines

The work presented in this thesis represents a remarkable improvement in the performance of both long-range and high-resolution BOTDA sensors. However, the advancements here reported have not yet been combined with other promising and well-proven techniques present in the literature.

The first and most straightforward combination would be the application of the post-processing techniques proposed by Soto *et al.* [90], particularly to the sensing schemes presented in Sections 6.3 and 6.4, whose measurements require a vast number of averages. Its application could ease the technical requirements and/or increase the system performance by taking advantage of the foreseeable significant SNR improvement.

Further investigations on the applicability of the novel BOTDA scanning method are to be done, where a reduction in the technical requirements would be very desirable. The need of narrow yet stable filters as well as the use of an extra intensity modulator increases the system complexity compared to standard BOTDA schemes. Additionally, the proposed scanning method has proven to solve the issues arising when relatively long fibers presenting a relatively uniform BFS are used. However this method lacks effectiveness when, for example, two long-enough fiber sections (of lengths circa $L_{eff}/2$) presenting well differentiated BFS profiles are present at the far end of the fiber. Therefore, other effective approaches to avoid non-local effects without increasing complexity are to be sought.

The application of a balanced detection scheme in combination with distortion-free (i.e. avoiding non-local effects) BOTDA schemes is yet to be thoroughly studied, since at a glance,

it does not appear to be straightforward. Successfully putting together these two techniques could help better exploiting the advancements presented in this thesis, particularly in high-probe power implementations.

The successful realization of a centimetric spatial resolution strain and temperature sensor over an extended measurement range opens new potential fields of applications, such as crack detection in large civil structures or bio-sensing. In the latter, the possibility of integrating optical fibers in textiles and sense over them (with the possibility of resolving ~1 million measurement points in a single garment) is yet to be explored, where being able to register changes in temperature over such a short resolution could be used by medical specialists in early disease detection.

Bibliography

[1] W. Zou, X. Long, and J. Chen, “Brillouin Scattering in Optical Fibers and Its Application to Distributed Sensors,” *Adv. Opt. Fiber Technol. Fundam. Opt. Phenom. Appl.*, pp. 3–54, 2015.

[2] H. Martins, “Distributed and Remote Fiber Sensing Assisted by Raman Effect,” 2014.

[3] R. Ramaswani, K. Sivarajan, and G. Sasaki, *Optical Networks: A Practical Perspective, 3rd Edition*, 3rd Editio., vol. 1. San Francisco, CA: Morgan Kaufmann, 2009.

[4] S. P. Singh and N. Singh, “Nonlinear Effects in Optical Fibers: Origin, Management and Applications,” *Prog. Electromagn. Res.*, vol. 73, pp. 249–275, 2007.

[5] C. V. Raman, “A new radiation,” *Indian J. Phys.*, vol. 37, no. 2, pp. 387–398, 1928.

[6] X. Angulo-Vinuesa, “Ultra-Long Range Brillouin Optical Time Domain Analysis,” Universidad de Alcalá, 2014.

[7] M. N. Islam, *Raman Amplifiers for Telecommunications 1*, vol. 90/1. New York, NY: Springer New York, 2004.

[8] J. P. Dakin, D. J. Pratt, G. W. Bibby, and J. N. Ross, “Distributed optical fibre Raman temperature sensor using a semiconductor light source and detector,” *Electron. Lett.*, vol. 21, no. 13, p. 569, 1985.

[9] E. J. Woodbury and W. K. Ng, “Ruby laser operation in the near IR,” *Proc. IRE*, vol. 50, no. 11, p. 2367, 1962.

[10] G. Eckhardt, R. W. Hellwarth, F. J. McClung, S. E. Schwarz, D. Weiner, and E. J. Woodbury, “Stimulated Raman Scattering From Organic Liquids,” *Phys. Rev. Lett.*, vol. 9, no. 11, pp. 455–457, Dec. 1962.

[11] R. W. Boyd, *Nonlinear optics*. Academic Press, 2008.

[12] G. P. Agrawal, *Nonlinear fiber optics*, 3rd Editio. Academic Press, 2001.

[13] R. G. Smith, “Optical Power Handling Capacity of Low Loss Optical Fibers as Determined by Stimulated Raman and Brillouin Scattering,” *Appl. Opt.*, vol. 11, no. 11, p. 2489, Nov. 1972.

[14] L. Brillouin, “Diffusion de la lumière et des rayons X par un corps transparent homogène. Influence de l’agitation thermique.,” *Ann. Phys.*, vol. 17, no. 21, pp. 88–122, 1922.

[15] M. Facchini, “Distributed Optical Fiber Sensors Based on Brillouin Scattering,” EPFL, 2001.

[16] A. Denisov, “Brillouin dynamic gratings in optical fibres for distributed sensing and advanced optical signal processing,” EPFL, 2015.

[17] D. Heiman, D. S. Hamilton, and R. W. Hellwarth, “Brillouin scattering measurements on optical glasses,” *Phys. Rev. B*, vol. 19, no. 12, pp. 6583–6592, Jun. 1979.

[18] M. Niklès, L. Thévenaz, and P. A. Robert, “Brillouin Gain Spectrum Characterization in Single-Mode Optical Fibers,” *J. Light. Technol.*, vol. 15, no. 10, pp. 1842–1851, 1997.

[19] L. Thévenaz, *Advanced Fiber Optics*. EPFL Press, 2011.

[20] R. Y. Chiao, C. H. Townes, and B. P. Stoicheff, “Stimulated Brillouin Scattering and Coherent Generation of Intense Hypersonic Waves,” *Phys. Rev. Lett.*, vol. 12, no. 21, pp. 592–595, May 1964.

[21] M. O. van Deventer and A. J. Boot, “Polarization properties of stimulated Brillouin scattering in single-mode fibers,” *J. Light. Technol.*, vol. 12, no. 4, pp. 585–590, Apr. 1994.

[22] Y. Aoki, K. Tajima, and I. Mito, “Input power limits of single-mode optical fibers due to stimulated Brillouin scattering in optical communication systems,” *J. Light. Technol.*, vol. 6, no. 5, pp. 710–719, May 1988.

[23] T. Horiguchi and M. Tateda, “BOTDA - Nondestructive measurement of single-mode optical fiber attenuation characteristics using Brillouin interaction: Theory,” *J. Light. Technol.*, vol. 7, no. 8, pp. 1170–1176, 1989.

[24] M. Niklès, L. Thévenaz, and P. A. Robert, “Simple distributed fiber sensor based on Brillouin gain spectrum analysis,” *Opt. Lett.*, vol. 21, no. 10, p. 758, May 1996.

[25] L. Thévenaz, S. F. Mafang, and J. Lin, “Effect of pulse depletion in a Brillouin optical time-domain analysis system,” *Opt. Express*, vol. 21, no. 12, p. 14017, Jun. 2013.

[26] A. Minardo, R. Bernini, and L. Zeni, “A simple technique for reducing pump depletion in long-range distributed brillouin fiber sensors,” *IEEE Sens. J.*, vol. 9, no. 6, pp. 633–634, 2009.

[27] X. Bao, J. Dhliwayo, N. Heron, D. J. Webb, and D. a. Jackson, “Experimental and theoretical studies on a distributed temperature sensor based on Brillouin scattering,” *J. Light. Technol.*, vol. 13, no. 7, pp. 1340–1348, 1995.

[28] A. Minardo, R. Bernini, L. Zeni, L. Thevenaz, and F. Briffod, “A reconstruction technique for long-range stimulated Brillouin scattering distributed fibre-optic sensors: experimental results,” *Meas. Sci. Technol.*, vol. 16, no. 4, pp. 900–908, Apr. 2005.

[29] X. Bao, J. Dhliwayo, N. Heron, D. J. Webb, and D. A. Jackson, “Experimental and theoretical studies on a distributed temperature sensor based on Brillouin scattering,” *J. Light. Technol.*, vol. 13, no. 7, pp. 1340–1348, Jul. 1995.

[30] L. Thévenaz and S. Foaleng Mafang, “Distributed fiber sensing using Brillouin echoes,” *19th Int. Conf. Opt. Fibre Sensors*, vol. 7004, p. 70043N–70043N, 2008.

[31] M. A. Soto, “Advanced techniques for distributed optical fiber sensors based on Raman and Brillouin scattering,” 2011.

[32] M. A. Soto and L. Thévenaz, “Modeling and evaluating the performance of Brillouin distributed optical fiber sensors.,” *Opt. Express*, vol. 21, no. 25, pp. 31347–66, 2013.

[33] T. Kurashima, T. Horiguchi, and M. Tateda, “Distributed-temperature sensing using stimulated Brillouin scattering in optical silica fibers,” *Opt. Lett.*, vol. 15, no. 18, p. 1038, Sep. 1990.

[34] K. Tai, A. Hasegawa, and A. Tomita, “Observation of modulational instability in optical fibers,” *Phys. Rev. Lett.*, vol. 56, no. 2, pp. 135–138, 1986.

[35] S. Foaleng Mafang, “Brillouin Echoes for Advanced Distributed Sensing in Optical Fibres,” EPFL, 2011.

[36] D. Alasia, “Advanced trends in nonlinear optics applied to distributed optical-fibre sensors,” EPFL, 2006.

[37] G. Van Simaeys, P. Emplit, and M. Haelterman, “Experimental Demonstration of the Fermi-Pasta-Ulam Recurrence in a Modulationally Unstable Optical Wave,” *Phys. Rev. Lett.*, vol. 87, no. 3, p. 33902, Jun. 2001.

[38] M. Alem, M. A. Soto, and L. Thévenaz, “Analytical model and experimental verification of the critical power for modulation instability in optical fibers,” vol. 23, no. 23, pp. 29514–29532, Nov. 2015.

[39] E. Geinitz, S. Jetschke, U. Röpke, S. Schröter, R. Willsch, and H. Bartelt, “The influence of pulse amplification on distributed fibre-optic Brillouin sensing and a method to compensate for systematic errors,” *Meas. Sci. Technol.*, vol. 10, no. 2, pp. 112–116, Feb. 1999.

[40] Q. Cui, S. Pamukcu, A. Lin, W. Xiao, and J. Toulouse, “Performance of double sideband modulated probe wave in BOTDA distributed fiber sensor,” *Microw. Opt. Technol. Lett.*, vol. 52, no. 12, pp. 2713–2717, Dec. 2010.

[41] K. Hotate and T. Hasegawa, “Measurement of Brillouin Gain Spectrum Distribution along an Optical Fiber Using a Correlation-Based Technique—Proposal, Experiment and Simulation—,” *IEICE TRANS. ELECTRON.*, vol. E83–C, no. 3, pp. 405–412, 2000.

[42] A. Denisov, M. A. Soto, and L. Thévenaz, “1’000’000 resolved points along a Brillouin distributed fibre sensor,” 2014, p. 9157D2.

[43] Y. London, Y. Antman, E. Preter, N. Levanon, and A. Zadok, “Brillouin Optical Correlation Domain Analysis Addressing 440 000 Resolution Points,” *J. Light. Technol.*, vol. 34, no. 19, pp. 4421–4429, Oct. 2016.

[44] A. Denisov, M. A. Soto, and L. Thévenaz, “Going beyond 1 000 000 resolved points in a Brillouin distributed fiber sensor: theoretical analysis and experimental demonstration,” *Nat. Publ. Gr.*, vol. 5, 2016.

[45] W. Li, X. Bao, Y. Li, and L. Chen, “Differential pulse-width pair BOTDA for high spatial resolution sensing,” *Opt. Express*, vol. 16, no. 26, p. 21616, Dec. 2008.

[46] A. W. Brown, B. G. Colpitts, and K. Brown, “Dark-Pulse Brillouin Optical Time-Domain Sensor With 20-mm Spatial Resolution,” *J. Light. Technol.*, vol. 25, no. 1, pp. 381–386, Jan. 2007.

[47] K. Y. Song, S. Chin, N. Primerov, and L. Thévenaz, “Time-Domain Distributed Fiber Sensor With 1 cm Spatial Resolution Based on Brillouin Dynamic Grating,” *J. Light. Technol. Vol. 28, Issue 14, pp. 2062-2067*, vol. 28, no. 14, pp. 2062–2067, 2010.

[48] C. A. Galindez Jamioy and J. M. Lopez-Higuera, “Decimeter Spatial Resolution by Using Differential Preexcitation BOTDA Pulse Technique,” *IEEE Sens. J.*, vol. 11, no. 10, pp. 2344–2348, Oct. 2011.

[49] X. Angulo-Vinuesa, A. Dominguez-Lopez, A. Lopez-Gil, J. D. Ania-Castañón, S. Martin-Lopez, and M. Gonzalez-Herraez, “Limits of BOTDA Range Extension Techniques,” *IEEE Sens. J.*, vol. 16, no. 10, 2016.

[50] K. De Souza and T. P. Newson, "Signal to noise and range enhancement of the Brillouin intensity based temperature sensor," *Opt. Express*, vol. 12, no. 12, pp. 2656–2661, 2004.

[51] A. Motil, A. Bergman, and M. Tur, "[INVITED] State of the art of Brillouin fiber-optic distributed sensing," *Opt. Laser Technol.*, vol. 78, pp. 81–103, 2016.

[52] A. Lopez-Gil, A. Dominguez-Lopez, S. Martin-Lopez, and M. Gonzalez-Herraez, "Simple Method for the Elimination of Polarization Noise in BOTDA Using Balanced Detection and Orthogonal Probe Sidebands," *J. Light. Technol.*, vol. 33, no. 12, pp. 2605–2610, Jun. 2015.

[53] E. Desurvire, *Erbium-doped fiber amplifiers : principles and applications*. Wiley, 1994.

[54] F. Rodríguez-Barrios, S. Martín-López, A. Carrasco-Sanz, P. Corredera, J. D. Ania-Castañón, L. Thévenaz, and M. González-Herráez, "Distributed brillouin fiber sensor assisted by first-order raman amplification," vol. 28, no. 15, pp. 2162–2172, 2010.

[55] S. Martin-Lopez, M. Alcon-Camas, F. Rodriguez, P. Corredera, J. D. Ania-Castañon, L. Thévenaz, and M. Gonzalez-Herraez, "Brillouin optical time-domain analysis assisted by second-order Raman amplification," vol. 18, no. 18, pp. 18769–18778, Aug. 2010.

[56] M. A. Soto, X. Angulo-Vinuesa, S. Martin-Lopez, S. H. Chin, J. D. Ania-Castañon, P. Corredera, E. Rochat, M. Gonzalez-Herraez, and L. Thévenaz, "Extending the real remoteness of long-range brillouin optical time-domain fiber analyzers," *J. Light. Technol.*, vol. 32, no. 1, pp. 152–162, 2014.

[57] J. Nuño del Campo, "Novel photonic systems and devices exploiting the Raman effect in optical fiber," Universidad de Alcala, 2013.

[58] D. E. McCumber, "Intensity Fluctuations in the Output of cw Laser Oscillators. I," *Phys. Rev.*, vol. 141, no. 1, pp. 306–322, Jan. 1966.

[59] P. N. Kean, B. D. Sinclair, K. Smith, W. Sibbett, C. J. Rowe, and D. C. J. Reid, "Experimental Evaluation of a Fibre Raman Oscillator Having Fibre Grating Reflectors," *J. Mod. Opt.*, vol. 35, no. 3, pp. 397–406, Mar. 1988.

[60] C. R. S. Fludger, V. Handerek, and R. J. Mears, "Pump to signal RIN transfer in Raman fiber amplifiers," *J. Light. Technol.*, vol. 19, no. 8, pp. 1140–1148, 2001.

[61] J. Bromage, "Raman Amplification for Fiber Communication Systems," *J. Light. Technol.*, vol. 22, no. 1, pp. 79–93, 2004.

[62] X. Angulo-Vinuesa, S. Martin-Lopez, J. Nuño, P. Corredera, J. D. Ania-Castañon, L. Thévenaz, and M. González-Herráez, "Raman-Assisted Brillouin Distributed Temperature Sensor Over 100 km Featuring 2 m Resolution and 1.2 °C Uncertainty," *J. Light. Technol. Vol. 30, Issue 8, pp. 1060-1065*, vol. 30, no. 8, pp. 1060–1065, 2012.

[63] M. A. Soto, G. Bolognini, and F. Di Pasquale, "Optimization of long-range BOTDA sensors with high resolution using first-order bi-directional Raman amplification," *Opt. Express*, vol. 19, no. 5, p. 4444, Feb. 2011.

[64] X. Angulo-Vinuesa, D. Bacquet, S. Martin-Lopez, P. Corredera, P. Szriftgiser, and M. Gonzalez-Herraez, "Relative intensity noise transfer reduction in raman-assisted BOTDA systems," vol. 26, no. 3, pp. 271–274, Feb. 2014.

[65] M. Dossou, D. Bacquet, and P. Szriftgiser, "Vector Brillouin optical time-domain analyzer for high-order acoustic modes," *Opt. Lett.*, vol. 35, no. 22, p. 3850, Nov. 2010.

[66] P. S. Moharir and A. Selvarajan, “Optical Barker codes,” *Electron. Lett.*, vol. 10, no. 9, p. 154, 1974.

[67] M. D. Jones, “Using simplex codes to improve OTDR sensitivity,” *IEEE Photonics Technol. Lett.*, vol. 5, no. 7, pp. 822–824, Jul. 1993.

[68] M. A. Soto, G. Bolognini, F. Di Pasquale, and L. Thévenaz, “Simplex-coded BOTDA fiber sensor with 1 m spatial resolution over a 50 km range,” *Opt. Lett.*, vol. 35, no. 2, p. 259, 2010.

[69] H. Iribas, A. Loayssa, F. Sauser, M. Llera, and S. Le Floch, “Cyclic coding for Brillouin optical time-domain analyzers using probe dithering,” *Opt. Express*, vol. 25, no. 8, p. 8787, Apr. 2017.

[70] J. Urricelqui, M. Sagues, and A. Loayssa, “BOTDA measurements tolerant to non-local effects by using a phase-modulated probe wave and RF demodulation.,” *Opt. Express*, vol. 21, no. 14, pp. 17186–94, 2013.

[71] M. A. Soto, M. Taki, G. Bolognini, and F. Di Pasquale, “Optimization of a DPP-BOTDA sensor with 25 cm spatial resolution over 60 km standard single-mode fiber using Simplex codes and optical pre-amplification,” *Opt. Express*, vol. 20, no. 7, p. 6860, 2012.

[72] X.-H. Jia, Y.-J. Rao, K. Deng, Z.-X. Yang, L. Chang, C. Zhang, and Z.-L. Ran, “Experimental Demonstration on 2.5-m Spatial Resolution and 1^{o}C Temperature Uncertainty Over Long-Distance BOTDA With Combined Raman Amplification and Optical Pulse Coding,” *IEEE Photonics Technol. Lett.*, vol. 23, no. 7, pp. 435–437, Apr. 2011.

[73] M. A. Soto, G. Bolognini, and F. Di Pasquale, “Long-range simplex-coded BOTDA sensor over 120 km distance employing optical preamplification.,” *Opt. Lett.*, vol. 36, no. 2, pp. 232–4, 2011.

[74] Y. Dong, H. Zhang, L. Chen, and X. Bao, “2 cm spatial-resolution and 2 km range Brillouin optical fiber sensor using a transient differential pulse pair,” *Appl. Opt.*, vol. 51, no. 9, p. 1229, 2012.

[75] S. M. Foaleng, M. Tur, J. C. Beugnot, and L. Thévenaz, “High spatial and spectral resolution long-range sensing using Brillouin echoes,” *J. Light. Technol.*, vol. 28, no. 20, pp. 2993–3003, 2010.

[76] P. C. Hobbs, “Ultrasensitive laser measurements without tears.,” *Appl. Opt.*, vol. 36, no. 4, pp. 903–20, 1997.

[77] H. R. Carleton and W. T. Maloney, “A Balanced Optical Heterodyne Detector,” *Appl. Opt.*, vol. 7, no. 6, p. 1241, Jun. 1968.

[78] I. Andonovic, L. Tancevski, M. Shabeer, and L. Bazgaloski, “Incoherent all-optical code recognition with balanced detection,” *J. Light. Technol.*, vol. 12, no. 6, pp. 1073–1080, Jun. 1994.

[79] Xu Wang, Naoya Wada, T. Miyazaki, and K. Kitayama, “Coherent OCDMA system using DPSK data format with balanced detection,” *IEEE Photonics Technol. Lett.*, vol. 18, no. 7, pp. 826–828, Apr. 2006.

[80] T. Dennis, S. D. Dyer, and A. Dienstfrey, “Phase-dispersion light scattering for quantitative size-imaging of spherical scatterers,” in *Biomedical Applications of Light Scattering,”*, 2007, vol. 6446, pp. 644609-644609–8.

[81] A. Dominguez-Lopez, A. Lopez-Gil, S. Martin-Lopez, and M. Gonzalez-Herraez, "Signal-to-noise ratio improvement in BOTDA using balanced detection," *IEEE Photonics Technol. Lett.*, vol. 26, no. 4, pp. 338–341, 2014.

[82] A. Dominguez-Lopez, A. Lopez-Gil, S. Martin-Lopez, and M. Gonzalez-Herraez, "Strong Cancellation of RIN Transfer in a Raman-Assisted BOTDA Using Balanced Detection," *IEEE Photonics Technol. Lett.*, vol. 26, no. 18, pp. 1817–1820, Sep. 2014.

[83] X. Angulo-Vinuesa, S. Martin-Lopez, P. Corredera, and M. Gonzalez-Herraez, "Raman-assisted Brillouin optical time-domain analysis with sub-meter resolution over 100 km," *Opt. Express*, vol. 20, no. 11, p. 12147, May 2012.

[84] T. Horiguchi and M. Tateda, "Optical-fiber-attenuation investigation using stimulated Brillouin scattering between a pulse and a continuous wave," *Opt. Lett.*, vol. 14, no. 8, p. 408, Apr. 1989.

[85] J. Urricelqui, M. Sagues, and A. Loayssa, "Phasorial differential pulse-width pair technique for long-range Brillouin optical time-domain analysis sensors," *Opt. Express*, vol. 22, no. 14, p. 17403, Jul. 2014.

[86] Z. Yang, X. Hong, J. Wu, H. Guo, and J. lin, "Theoretical and experimental investigation of an 82-km-long distributed Brillouin fiber sensor based on double sideband modulated probe wave," *Opt. Eng.*, vol. 51, no. 12, p. 124402, Dec. 2012.

[87] J. P. Gordon, "Theory of the soliton self-frequency shift," *Opt. Lett.*, vol. 11, no. 10, p. 662, Oct. 1986.

[88] A. Dominguez-Lopez, X. Angulo-Vinuesa, A. Lopez-Gil, S. Martin-Lopez, and M. Gonzalez-Herraez, "Non-local effects in dual-probe-sideband Brillouin optical time domain analysis," *Opt. Express*, vol. 23, no. 8, p. 10341, 2015.

[89] M. A. Soto, G. Bolognini, F. Di Pasquale, and L. Thévenaz, "Long-range Brillouin optical time-domain analysis sensor employing pulse coding techniques," *Meas. Sci. Technol. Meas. Sci. Technol*, vol. 21, no. 21, pp. 94024–7, 2010.

[90] M. A. Soto, J. A. Ramírez, and L. Thévenaz, "Intensifying the response of distributed optical fibre sensors using 2D and 3D image restoration.," *Nat. Commun.*, vol. 7, p. 10870, 2016.

[91] S. Diaz, S. Foaleng Mafang, M. Lopez-Amo, and L. Thevenaz, "A High-Performance Optical Time-Domain Brillouin Distributed Fiber Sensor," *IEEE Sens. J.*, vol. 8, no. 7, pp. 1268–1272, Jul. 2008.

[92] A. Dominguez-Lopez, Z. Yang, M. A. Soto, X. Angulo-Vinuesa, S. Martin-Lopez, L. Thevenaz, and M. Gonzalez-Herraez, "Novel scanning method for distortion-free BOTDA measurements," *Opt. Express*, vol. 24, no. 10, p. 10188, May 2016.

[93] Z. Yang, X. Hong, J. Wu, H. Guo, and J. lin, "Theoretical and experimental investigation of an 82-km-long distributed Brillouin fiber sensor based on double sideband modulated probe wave," *Opt. Eng.*, vol. 51, no. 12, p. 124402, Dec. 2012.

[94] R. Ruiz-Lombera, J. Urricelqui, M. Sagues, J. Mirapeix, J. M. Lopez-Higuera, and A. Loayssa, "Overcoming Nonlocal Effects and Brillouin Threshold Limitations in Brillouin Optical Time-Domain Sensors," *IEEE Photonics J.*, vol. 7, no. 6, pp. 1–9, Dec. 2015.

[95] J. Urricelqui, M. A. Soto, and L. Thévenaz, "Sources of noise in Brillouin optical time-domain analyzers," 2015, p. 963434.

[96] M. A. Soto, M. Taki, G. Bolognini, and F. Di Pasquale, "Simplex-Coded BOTDA Sensor Over 120-km SMF With 1-m Spatial Resolution Assisted by Optimized Bidirectional Raman Amplification," *IEEE Photonics Technol. Lett.*, vol. 24, no. 20, pp. 1823–1826, Oct. 2012.

[97] X.-H. Jia, Y.-J. Rao, Z.-N. Wang, W.-L. Zhang, C.-X. Yuan, X.-D. Yan, J. Li, H. Wu, Y.-Y. Zhu, and F. Peng, "Distributed Raman amplification using ultra-long fiber laser with a ring cavity: characteristics and sensing application," *Opt. Express*, vol. 21, no. 18, p. 21208, Sep. 2013.

[98] W. Li, X. Bao, Y. Li, and L. Chen, "Differential pulse-width pair BOTDA for high spatial resolution sensing.," *Opt. Express*, vol. 16, no. 26, pp. 21616–21625, 2008.

[99] A. Dominguez-Lopez, M. A. Soto, S. Martin-Lopez, L. Thevenaz, and M. Gonzalez-Herraez, "Resolving 1 million sensing points in an optimized differential time-domain Brillouin sensor," *Opt. Lett.*, vol. 42, no. 10, p. 1903, May 2017.

[100] A. Dominguez-Lopez, M. A. Soto, S. Martin-Lopez, L. Thevenaz, and M. Gonzalez-Herraez, "Overcoming High-resolution Limitations in Optimized Long-range BOTDA Sensors," in *Asia Pacific Optical Sensors Conference*, 2016, p. Th3A.6.

[101] A. Dominguez-Lopez, M. A. Soto, S. Martin-Lopez, M. Gonzalez-Herraez, and L. Thevenaz, "Sub-metric spatial resolution over an extended range using differential time-domain Brillouin sensing," in *Proceedings of SPIE - The International Society for Optical Engineering*, 2016, p. 991635.

[102] D. Viveiros, J. Ribeiro, J. P. Carvalho, J. Ferreira, A. M. R. Pinto, R. A. Perez-Herrera, S. Diaz, A. Lopez-Gil, A. Dominguez-Lopez, O. Esteban, H. F. Martins, S. Martin-Lopez, H. Baierl, J.-L. Auguste, R. Jamier, S. Rougier, J. L. Santos, D. Flores, P. Roy, M. González-Herráez, M. López-Amo, and J. M. Baptista, "Fiber optic sensing system for monitoring of coal waste piles in combustion," in *Proceedings of SPIE - The International Society for Optical Engineering*, 2014, vol. 9157.

[103] D. Viveiros, J. Ribeiro, J. Ferreira, A. Lopez-Aldaba, A. M. R. Pinto, R. A. Perez-Herrera, S. Diaz, A. Lopez-Gil, A. Dominguez-Lopez, O. Esteban, S. Martin-Lopez, J.-L. Auguste, R. Jamier, S. Rougier, S. O. Silva, O. Frazão, J. L. Santos, D. Flores, P. Roy, M. Gonzalez-Herraez, M. Lopez-Amo, and J. M. Baptista, "Fiber optic sensing system for temperature and gas monitoring in coal waste pile combustion environments," in *Proceedings of SPIE - The International Society for Optical Engineering*, 2015, vol. 9634.

[104] D. Viveiros, J. Ribeiro, J. Ferreira, A. M. R. Pinto, R. A. Perez-Herrera, S. Diaz, A. Lopez-Gil, A. Dominguez-Lopez, O. Esteban, H. F. Martins, S. Martin-Lopez, H. Baierl, J.-L. Auguste, R. Jamier, S. Rougier, J. L. Santos, D. Flores, P. Roy, M. Gonzalez-Herraez, M. Lopez-Amo, and J. M. Baptista, "Monitoring of coal waste piles with fiber optic sensing technology," in *exp.at 2015 - 3rd Experiment International Conference: Online Experimentation*, 2016.

[105] L. Duarte, A. Teodoro, J. Gonçalves, J. Ribeiro, D. Flores, A. Lopez-Gil, A. Dominguez-Lopez, X. Angulo-Vinuesa, S. Martin-Lopez, and M. Gonzalez-Herraez, "Distributed Temperature Measurement in a Self-Burning Coal Waste Pile through a GIS Open Source Desktop Application," *ISPRS Int. J. Geo-Information*, vol. 6, no. 3, p. 87, Mar. 2017.

Appendix A - Patents & Publications

Patents

"Sistema de detección diferencial para sensores distribuidos sobre fibra óptica basados en scattering Brillouin estimulado" PCT: 14820065.2. & US: 14/902,819.

Journal papers

- A. Dominguez-Lopez, A. Lopez-Gil, S. Martin-Lopez, and M. Gonzalez-Herraez, "Signal-to-noise ratio improvement in BOTDA using balanced detection," *IEEE Photonics Technol. Lett.*, vol. 26, no. 4, pp. 338–341, 2014.
- A. Dominguez-Lopez, A. Lopez-Gil, S. Martin-Lopez, and M. Gonzalez-Herraez, "Strong Cancellation of RIN Transfer in a Raman-Assisted BOTDA Using Balanced Detection," *IEEE Photonics Technol. Lett.*, vol. 26, no. 18, pp. 1817–1820, Sep. 2014.
- A. Dominguez-Lopez, X. Angulo-Vinuesa, A. Lopez-Gil, S. Martin-Lopez, and M. Gonzalez-Herraez, "Non-local effects in dual-probe-sideband Brillouin optical time domain analysis," *Opt. Express*, vol. 23, no. 8, p. 10341, 2015.
- A. Dominguez-Lopez, Z. Yang, M. A. Soto, X. Angulo-Vinuesa, S. Martin-Lopez, L. Thévenaz, and M. Gonzalez-Herraez, "Novel scanning method for distortion-free BOTDA measurements," *Opt. Express*, vol. 24, no. 10, p. 10188, May 2016.
- A. Dominguez-Lopez, M. A. Soto, S. Martin-Lopez, L. Thévenaz, and M. Gonzalez-Herraez, "Resolving 1 million sensing points in an optimized differential time-domain Brillouin sensor," *Opt. Lett.*, vol. 42, no. 10, p. 1903, May 2017.
- A. Lopez-Gil, A. Dominguez-Lopez, S. Martin-Lopez, and M. Gonzalez-Herraez, "Simple method for the elimination of polarization noise in BOTDA using balanced detection and orthogonal probe sidebands," *J. Light. Technol.*, vol. 33, no. 12, 2015.
- A. Lopez-Gil, X. Angulo-Vinuesa, A. Dominguez-Lopez, S. Martin-Lopez, and M. Gonzalez-Herraez, "Exploiting nonreciprocity in BOTDA systems," *Opt. Lett.*, vol. 40, no. 10, 2015.
- A. Lopez-Gil, M. A. Soto, X. Angulo-Vinuesa, A. Dominguez-Lopez, S. Martin-Lopez, L. Thévenaz, and M. Gonzalez-Herraez, "Evaluation of the accuracy of BOTDA systems based on the phase spectral response," *Opt. Express*, vol. 24, no. 15, 2016.

- X. Angulo-Vinuesa, A. Dominguez-Lopez, A. Lopez-Gil, J. D. Ania-Castañón, S. Martin-Lopez, and M. Gonzalez-Herraez, "Limits of BOTDA Range Extension Techniques," *IEEE Sens. J.*, vol. 16, no. 10, 2016.
- A. Lopez-Gil, X. Angulo-Vinuesa, A. Dominguez-Lopez, S. Martin-Lopez, and M. Gonzalez-Herraez, "Simple Baseband Method for the Distributed Analysis of Brillouin Phase-Shift Spectra," *IEEE Photonics Technol. Lett.*, vol. 28, no. 13, 2016.
- L. Duarte, A. Teodoro, J. Gonçalves, J. Ribeiro, D. Flores, A. Lopez-Gil, A. Dominguez-Lopez, X. Angulo-Vinuesa, S. Martin-Lopez, and M. Gonzalez-Herraez, "Distributed Temperature Measurement in a Self-Burning Coal Waste Pile through a GIS Open Source Desktop Application," *ISPRS Int. J. Geo-Information*, vol. 6, no. 3, p. 87, Mar. 2017.

Main Conferences

- A. Dominguez-Lopez, Z. Yang, M. A. Soto, X. Angulo-Vinuesa, S. Martin-Lopez, L. Thévenaz, and M. Gonzalez-Herraez, "Reaching the ultimate performance limit given by non-local effects in BOTDA sensors," in Proceedings of SPIE - The International Society for Optical Engineering, 2015, vol. 9634.
- A. Dominguez-Lopez, A. Lopez-Gil, S. Martin-Lopez, and M. Gonzalez-Herraez, "Balanced detection in Brillouin optical time domain analysis," in Proceedings of SPIE - The International Society for Optical Engineering, 2014, vol. 9157.
- A. López-Gil, A. Domínguez-López, S. Martín-López, and M. González-Herráez, "Simple method for the elimination of polarization noise in BOTDA using balanced detection of orthogonally polarized Stokes and anti-Stokes probe sidebands," in Proceedings of SPIE - The International Society for Optical Engineering, 2014, vol. 9157.
- D. Viveiros, J. Ribeiro, J. P. Carvalho, J. Ferreira, A. M. R. Pinto, R. A. Perez-Herrera, S. Diaz, A. Lopez-Gil, A. Dominguez-Lopez, O. Esteban, H. F. Martins, S. Martin-Lopez, H. Baierl, J.-L. Auguste, R. Jamier, S. Rougier, J. L. Santos, D. Flores, P. Roy, M. González-Herráez, M. López-Amo, and J. M. Baptista, "Fiber optic sensing system for monitoring of coal waste piles in combustion," in Proceedings of SPIE - The International Society for Optical Engineering, 2014, vol. 9157.
- M. Gonzalez-Herraez, A. Dominguez-Lopez, A. Lopez-Gil, H. F. Martins, S. Martin-Lopez, X. Angulo-Vinuesa, and P. Corredera, "Long-range static and dynamic distributed sensing," in Proceedings of IEEE Sensors, 2014, vol. 2014–Decem, no. December.
- A. Dominguez-Lopez, X. Angulo-Vinuesa, A. Lopez-Gil, S. Martin-Lopez, and M. Gonzalez-Herraez, "Unexpected non-local effects in dual-probe-sideband BOTDA," in Proceedings of SPIE - The International Society for Optical Engineering, 2015, vol. 9634.
- X. Angulo-Vinuesa, A. Lopez-Gil, A. Dominguez-Lopez, J. L. Cruz, M. V. Andres, S. Martin-Lopez, and M. Gonzalez-Herraez, "Simultaneous gain and phase profile determination on an interferometric BOTDA," in Proceedings of SPIE - The International Society for Optical Engineering, 2015, vol. 9634.
- A. Lopez-Gil, X. Angulo-Vinuesa, A. Dominguez-Lopez, S. Martin-Lopez, and M. Gonzalez-Herraez, "Simple BOTDA temperature sensor based on distributed Brillouin Phase-Shift measurements within a Sagnac interferometer," in Proceedings of SPIE - The International Society for Optical Engineering, 2015, vol. 9634.

- X. Angulo-Vinuesa, A. Dominguez-Lopez, A. Lopez-Gil, J. D. Ania-Castañon, S. Martin-Lopez, and M. Gonzalez-Herraez, “Rating the limitations and effectiveness of BOTDA range extension techniques,” in Proceedings of SPIE - The International Society for Optical Engineering, 2015, vol. 9634.
- A. Dominguez-Lopez, M. A. Soto, S. Martin-Lopez, L. Thévenaz, and M. Gonzalez-Herraez, “Overcoming High-resolution Limitations in Optimized Long-range BOTDA Sensors,” in Asia Pacific Optical Sensors Conference, 2016, p. Th3A.6.
- A. Dominguez-Lopez, M. A. Soto, S. Martin-Lopez, M. Gonzalez-Herraez, and L. Thévenaz, “Sub-metric spatial resolution over an extended range using differential time-domain Brillouin sensing,” in Proceedings of SPIE - The International Society for Optical Engineering, 2016, p. 991635.
- A. Lopez-Gil, X. Angulo-Vinuesa, M. A. Soto, A. Dominguez-Lopez, S. Martin-Lopez, L. Thévenaz, and M. Gonzalez-Herraez, “Gain vs phase in BOTDA setups,” in Proceedings of SPIE - The International Society for Optical Engineering, 2016, vol. 9916.

Appendix B - List of Acronyms

Acronym	Meaning
ASE	Amplified Spontaneous Emission
ASpBS	Amplified Spontaneous Brillouin Scattering
AWG	Arbitrary Waveform Generator
BD	Balanced Detector
BFS	Brillouin Frequency Shift
BGS	Brillouin Gain Spectrum
BOCDA	Brillouin Optical Correlation Domain Analysis
BOTDA	Brillouin Optical Time Domain Analysis
BLS	Brillouin Loss Spectrum
BW	Bandwidth
CSIC	Spanish National Research Council
CW	Continuous Wave
DC	Direct Current
DPP	Differential Pulse-width Pair
DWDM	Dense Wavelength-Division Multiplexer
DSB	Double Side-Band
EDFA	Erbium-Doped Fiber Amplifier
EOM	Electro-Optical Modulator
EPFL	Swiss Federal Institute of Technology
ER	Extinction Ratio
ESA	Electrical Spectrum Analyzer
FUT	Fiber Under Test
FWHM	Full Width at Half Maximum
GFO	Group of Fibre Optics
I&T	Current and Temperature

LD	Laser Diode
MEMS	Micro Electro-Mechanical Switch
MI	Modulation Instability
OTDR	Optical Time Domain Reflectometry
PS	Polarization Scrambler/Switch
RF	Radio Frequency
RFL	Raman Fiber Laser
RFS	Raman Frequency Shift
RIN	Relative Intensity Noise
RMS	Root Mean Square
SBS	Stimulated Brillouin Scattering
SMF	Single Mode Fiber
SNR	Signal to Noise Ratio
SOA	Semiconductor Optical Amplifier
SpBS	Spontaneous Brillouin Scattering
SpRS	Spontaneous Raman Scattering
SRS	Stimulated Raman Scattering
SSB	Single Side-Band
UAH	University of Alcala
VOA	Variable Optical Attenuator